POLITECNICO DI MILANO

Dipartimento di Chimica, Materiali e Ingegneria Chimica

Master of Science in Materials Engineering

Out of Phase Multiaxial Fatigue Strength of a Cast Iron

Advisor   :   Prof. Stefano FOLETTI

Co-advisor :   PhD Mihaela CRISTEA

Master thesis by :   Cagdas CENGIZ

ID Number   :   749555

Academic Year 2011 – 2012

POLITECNICO DI MILANO

Dipartimento di Chimica, Materiali e Ingegneria Chimica

Master of Science in Materials Engineering

Out of Phase Multiaxial Fatigue Strength of a Cast Iron

Thesis by   :   _____
                           (Cagdas CENGIZ)

Advisor   :   _____
                           (Prof. Stefano FOLETTI)

Co-advisor :   _____
                           (PhD Mihaela CRISTEA)

Academic Year 2011 – 2012

Contents

List of Figures

List of Tables

Abstract

The purpose of this study is to understand the behavior of a ductile iron under combined compressive axial and torsional nonproportional loading conditions. Moreover, the final aim is to propose a model to predict the multiaxial fatigue limit for defective materials.

Chapter 1 is the introduction part explains briefly importance of multiaxial fatigue on structural mechanical components and methodology performed in this study. Chapter 2 covers the general review of the literature about fatigue, multiaxial fatigue and prediction models for multiaxial fatigue limit. In the Chapter 3, experimental methodology of axial, torsional and multiaxial tests, and mechanical information of the material are mentioned. Chapter 4 is the results and discussion part, all the experimental results of axial, torsional and multiaxial fatigue tests, and fracture surfaces of specimens with microstructural characterizations were published. Moreover, Papadopoulos model was applied and error percentages with respect to experimental results were calculated. Finally, Nadot's methodology was applied in order to define the effect of defect size on multiaxial fatigue limit.

Keywords: *high cycle fatigue; multiaxial fatigue; nonproportional loading; out of phase loading; ductile cast iron; integral approach; casting defect*

1. Introduction

Most of structural mechanical components as crank shafts, pressure vessels, blade/rotor junctions, and aeronautical components are usually subjected to multiaxial loading conditions in service and the sources of multiaxiality mostly arise from geometry, defects, residual stresses, and external loadings. Multiaxial fatigue can be defined as the fatigue process consisted of combined complex states of stresses [1] [2] [3].

The purpose of this study is to understand the behavior of a ductile iron roll for tube production under combined compressive axial and torsional nonproportional loading conditions. Due to the casting process, these materials have casting defects as shrinkage porosities. According to the FEM data, these rolls are working under nonproportional multiaxial stresses at 90° phase difference and the ratio of $R = \frac{\sigma_{min}}{\tau_{amp}} = -4$ and -3. In order to understand the behavior; pure axial, pure torsional, and multiaxial fatigue tests were run; moreover microstructural and fracture surfaces were observed. Furthermore, Papadopoulos Criterion [4] was proposed to predict the multiaxial fatigue limit with the inputs of pure axial and pure torsional fatigue limits. Furthermore, among different approaches in the literature for containing defects, Nadot's methodology [5] was chosen to define effect of defect size on fatigue limit which consists of Murakami's empirical approach [6] and a multiaxial fatigue limit prediction criterion (Papadopoulos Criterion).

2. Fatigue and Multiaxial Fatigue on Cast Iron

Ductile irons' have a defective structure due to the casting process. Defects in this study are shrinkage porosities which behave as stress risers and decrease the stress bearing cross section area of the component. One approach about the effect of defect size on fatigue limit in the literature is proposed by Murakami [6] where the crack is considered as a pre-existing crack and the crack threshold is estimated from the fatigue limit. In this approach, defect size is considered in the square root of the surface area ($\sqrt{area}$) of the defect in the plane perpendicular to the maximum principal stress direction. Then, effect of these changes in defect size is considered in the manner of multiaxial fatigue condition by considering Papadopoulos criterion [4]. In the next sections of Chapter 2, general information of fatigue and multiaxial fatigue was mentioned.

2.1   Fatigue Mechanism

Fatigue life has two discrete periods namely crack nucleation and early growth, and crack growth of stage I-II-III. Conditions like environment, surface quality, residual stress, microstructure, etc. affect these two periods differently; some of them have an influence on nucleation, some of them have on growth [7].

2.1.1   Crack Nucleation and Early Growth

Nucleation of fatigue cracks occurs at very early stages of component life generally on the surface of the material, almost just after the stress level above fatigue limit. It starts preferably from the surface at lower stresses because surface grains are surrounded by the environment (e.g. air, sea water) and have lower constraints on slip systems than subsurface grains which are constrained by other grains of the material. As a consequence, it can be said that fatigue crack nucleation is a surface phenomenon [7] [8, pp. 77-98].

Cracks rarely nucleate at subsurface. If it happens, it is generally at a porosity, grain boundary, second phase particle or inclusion as shown in Figure 2.1.1. [8, pp. 77-98].
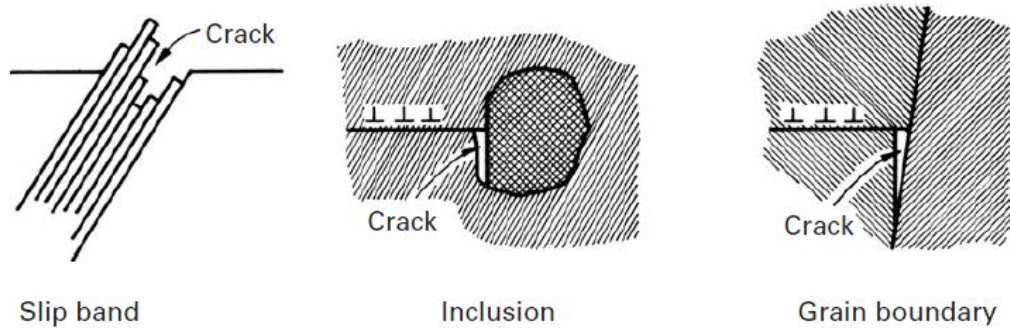
Figure 2.1.1 Some mechanisms of fatigue crack nucleation [9]

The slip bands take place due to the cyclic shear stresses. They initiate from the grains whose crystallographic slip planes are favorably oriented with respect to the applied cyclic shear stress. Therefore, each grain has a different resolved shear stress on its planes according to its orientation and applied cyclic shear stress. When the applied stress is increased, the number of grains who are under a higher stress than critical resolved shear stress will increase [8, pp. 77-98].

A model of nucleation mechanism of a fatigue crack is shown in Figure 2.1.2. During the loading part a new surface will be appeared and it will be oxidized immediately; and also, due to the loading, a strain hardening will take place on the slip band. Therefore, upon unloading part a larger shear stress in reversed direction will be present on the slip band. These two causes (oxide layer formation and strain hardening) explain why fatigue phenomenon is not fully reversible. Finally, reversed slip occurs on the adjacent parallel slip planes on the same slip band and this position of the reversed slip determines that it forms intrusion or extrusion. If it takes place upper side of the slip band, it forms intrusion; otherwise, it forms extrusion [7] [9].
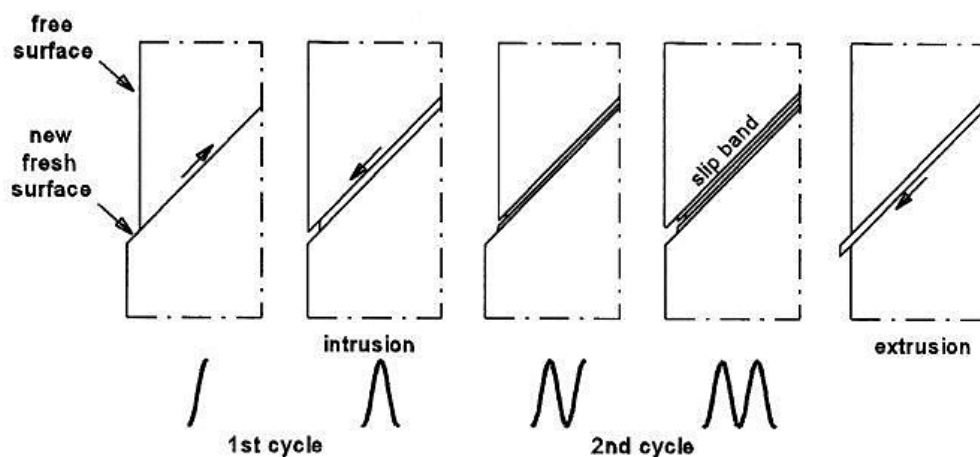
Figure 2.1.2 Formation of intrusion and extrusion [7]

2.1.2   Crack Growth

Surface properties are not relevant for growth mechanism. Crack has already propagated to the interior of the materials may be a couple of grains but low surface restraints or surface properties like roughness are not related to the crack anymore. Therefore, the resistance against the crack growth is a bulk property [7].

Once the cracks have nucleated on the surface under continuous cyclic stresses, they tend to merge and propagate along the planes of maximum shear stress for each grain. This is the growth of stage I. After a couple of grains, crack starts to grow along the axis perpendicular to tensile stress as in Figure 2.1.3 until reaching the critical length which gives rise to failure of the material [8, pp. 77-98] [10].
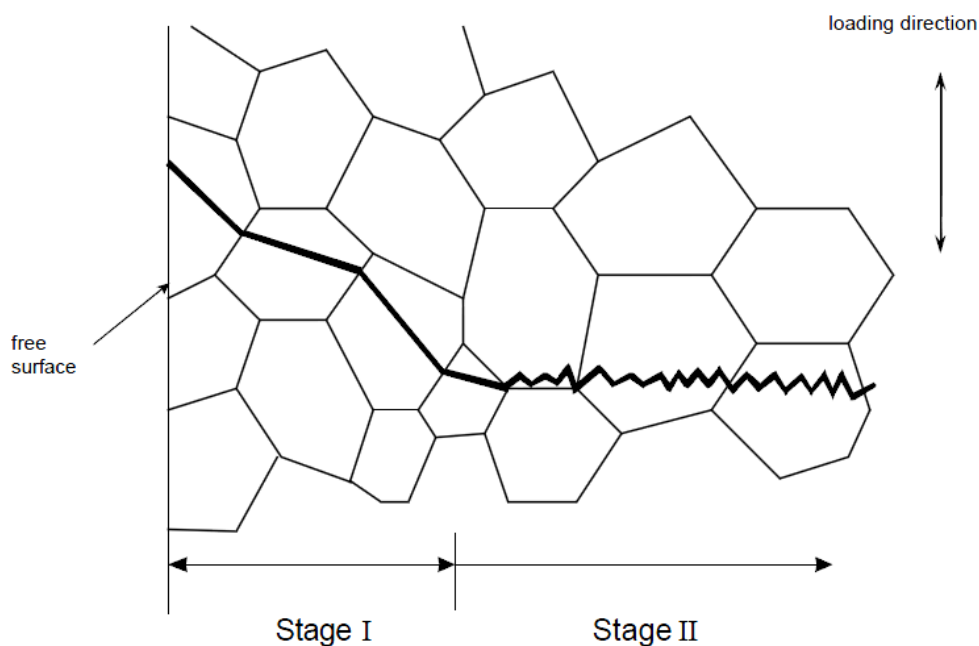
Figure 2.1.3 Stage I and Stage II growths [8, pp. 77-98]

If the proportions of spent time in various stages of the whole lifetime are considered, it will be seen that under low stresses: nucleation and stage I will take the large proportion but under high stresses, stage II will take the large proportion as seen in Figure 2.1.4 [11].
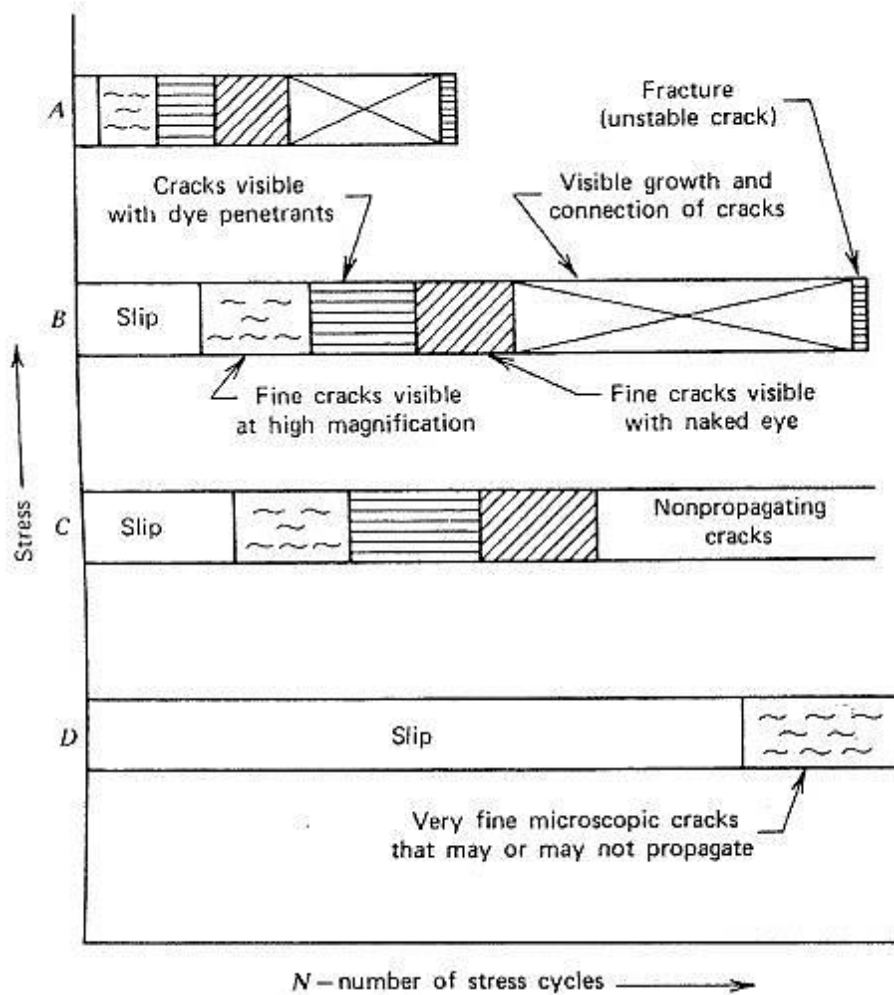
Figure 2.1.4 Schematic representation of fatigue process [10]

2.1.2.1 Growth Mechanism under Tensile Stress (Mode I)

After crack has grown away from the surface under tensile cyclic stresses, it propagates in the duplex shear band form (zig-zag form, Figure 2.1.5). This mechanism forms striation mark on the crack surface and each cycle results in the formation of one striation mark (Figure 2.1.6) [8, pp. 77-98].
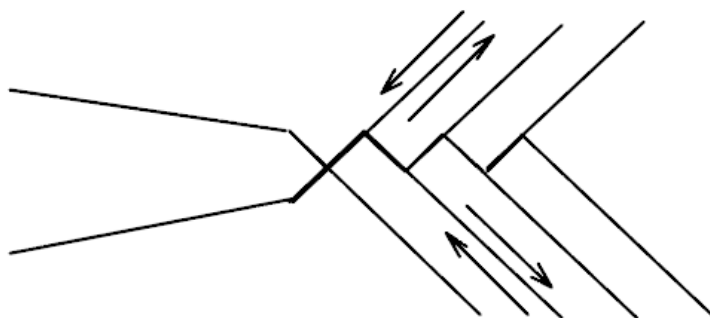
Figure 2.1.5 Crack growth in duplex shear band form [8, pp. 77-98]
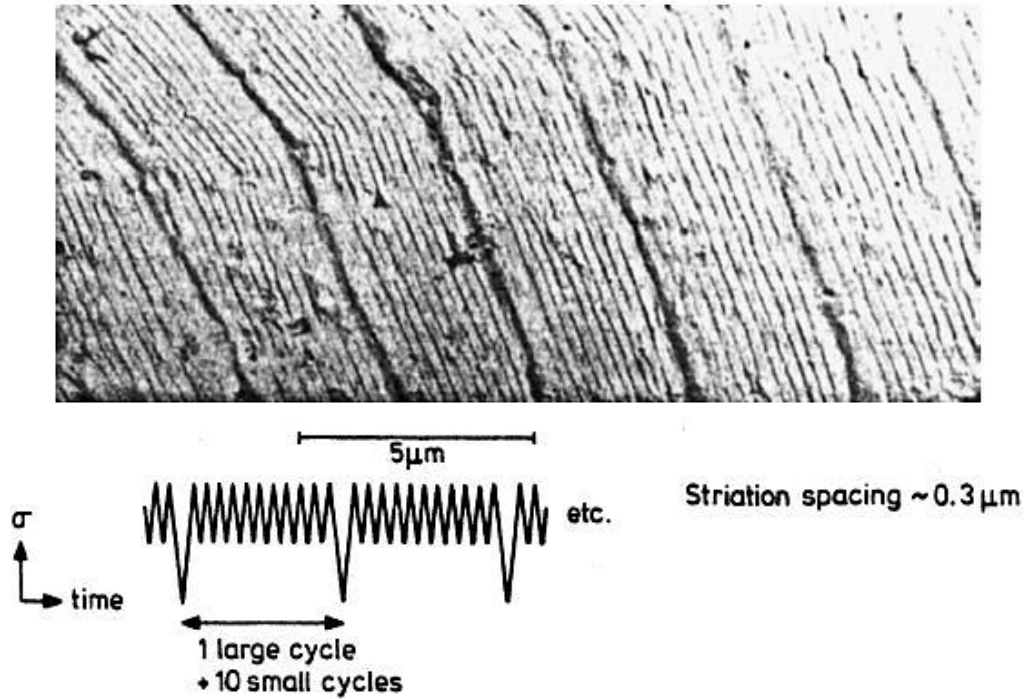
Figure 2.1.6 Striation marks on Al-alloy sheet [7]

Mechanism takes place macroscopically under tensile stresses but microscopically governed by local shear stresses on the crack tip [8, pp. 77-98]. At the start of the loading cycle the crack tip is sharp (Figure 2.1.7-a). As the tensile load is applied at the crack tip, slips takes place along planes of maximum shear stress (Figure 2.1.7-b). As the crack widens to its maximum extension (Figure 2.1.7-c) it grows longer by plastic shearing and at the same time its tip becomes blunter. If the stress is reversed, the crack tip re-sharpens by buckling and folding of the newly created surface into a double notch resulting in a striation formation (Figure 2.1.7-d) and (Figure 2.1.7-e). The re-sharpened crack is then ready to advance and be blunted in the next stress cycle [11] [12].
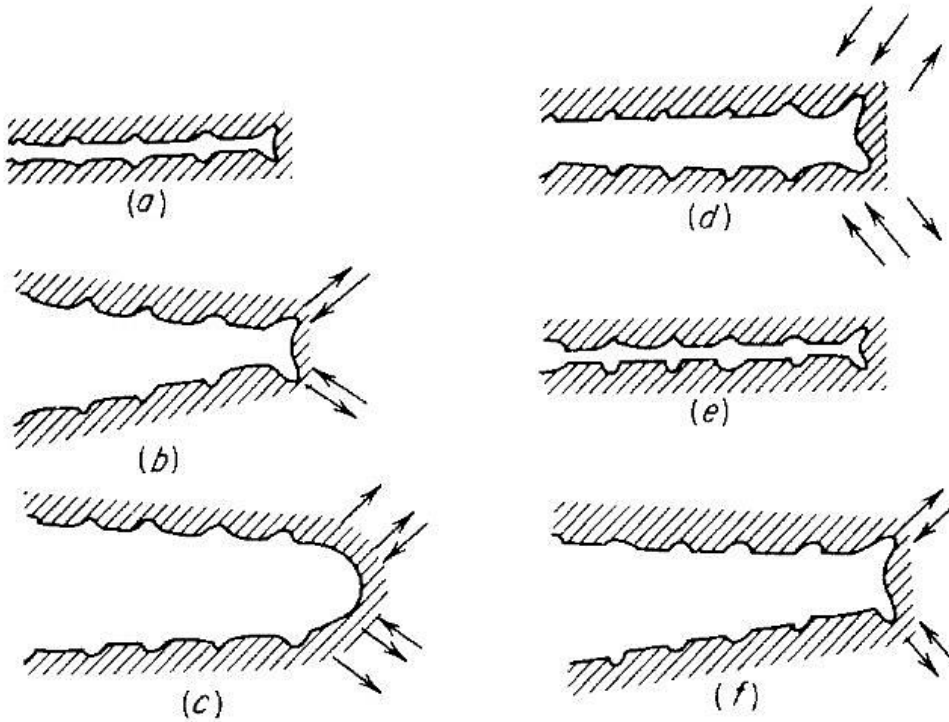
Figure 2.1.7 Plastic blunting process for growth of stage II fatigue crack [11]

2.1.2.2 Growth Mechanism under Shear Stress (Mode II)

Under shear stress fatigue crack propagates parallel to direction of the stress (Figure 2.1.8). The difference of Mode II growth with Mode I growth is in Mode II growth crack faces are in contact so they create friction. This decreases the propagation rate. Due to the rubbing of the faces, marks like striations are not formed, and its fracture surface is featureless. However, combined tension Mode I and Mode II load can reduce the rubbing of the faces and greatly accelerate the crack. As well, compression Mode I slows down the crack growth by increasing the friction forces [8, pp. 77-98].
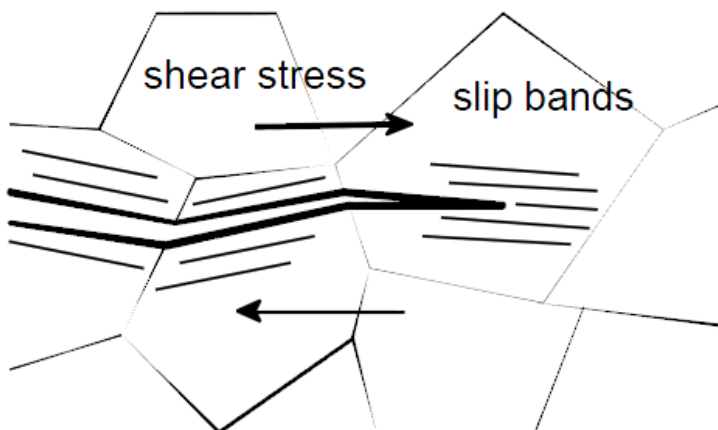
Figure 2.1.8 Crack growth under shear stress [8, pp. 77-98]

2.2   Proportionality and Nonproportionality of Multiaxial Loadings

Multiaxial fatigue stresses are classified in two categories: proportional loadings and nonproportional loadings. In proportional loading, principal stress directions remain fixed with respect to the loading axes and components of stress vary with time. In nonproportional loading, principal stress directions, components of stress and/or ratios between principal stresses vary with time.

Under nonproportional multiaxial fatigue loading conditions, different cyclic deformations (strain hardening or softening) and fatigue behaviors may be observed depending on the material type [8].

Proportional loading is illustrated for combined axial and torsion loading of a shaft shown in Figure 2.2.1(a). The loads in Figure 2.2.1(b) are applied in-phase, so that the maximum and minimum axial and torsion stresses occur simultaneously. The ratio of axial stress, σ_y, and torsion stress, τ_{xy}, remains constant during cycling as shown by the linear relationship in Figure 2.2.1(c). And also, Mohr's circles of stress at times 2 and 3 during the in-phase loading cycle are shown in Figure 2.2.1(d). It can be seen that the orientation of the principal normal stress directions remains fixed (i.e., angle 2α remains constant), even though the size of the circle changes as the magnitudes of the loads vary with time. This is, therefore, called proportional loading [10].

(a)   (b)

(c)   (d)
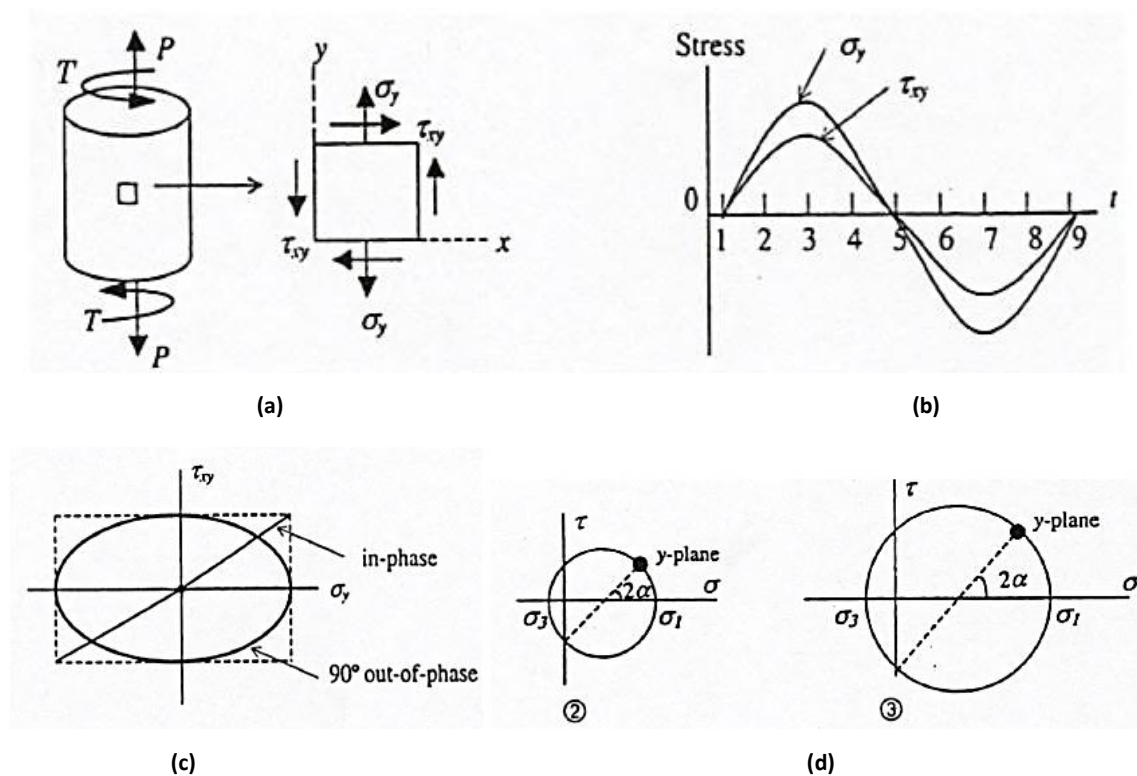
Figure 2.2.1 (a) Stress element in axial-torsion loading. (b) Applied in-phase axial and shear stress histories. (c) Stress path for in-phase and 90° out-of-phase loading. (d) Mohr's circle of stress at times 2 and 3 in the cycle for in-phase loading [10]

If the loads are applied 90° out-of-phase as shown in Figure 2.2.2 (a, b), the stress path, $\sigma_y - \tau_{xy}$, follows an ellipse, as shown in Figure 2.2.2 (c). The ratio of axial stress, σ_y, and torsion stress, τ_{xy}, continuously varies during the cycle. And also, Mohr's circles of stress at three times (1, 2, and 3) during the out-of-phase loading cycle are shown in Figure 2.2.2 (d). The orientations of the principal normal stress axes continuously rotate with respect to the loading axes (i.e. x-y axes). The maximum principal normal stress axis orientation starts out at $\alpha = 45°$ at time 1, decreases to a smaller α at time 2, and rotates to $\alpha = 0°$ at time 3. Then it continues to rotate in a clockwise direction until point 9, where it returns to $\alpha = 45°$. This is, therefore, an example of nonproportional loading [10].
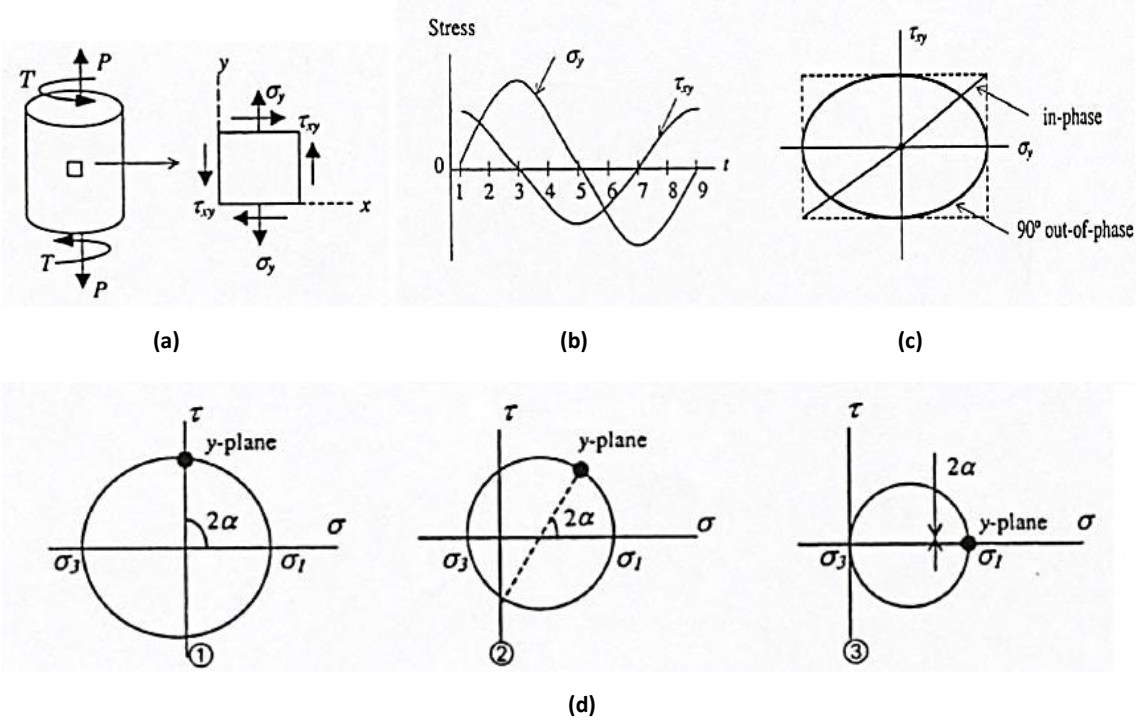
Figure 2.2.2 (a) Stress element in axial-torsion loading. (b) Applied 90° out-of-phase axial and shear stress histories. (c) Stress path for in-phase and 90° out-of-phase loading. (d) Mohr's circle of stress at times 1, 2, and 3 in the cycle for 90° out-of-phase loading [10]

2.2.1 Nonproportional Cyclic Hardening

Plastic deformation of a material results in work hardening because dislocations are generated in a large amount and their movements are hindered due to the frequent interactions with each other and dislocations pile up in front of barriers such as grain boundaries; these situations induce hardening of the materials. This phenomenon is strongly relevant to Von Mises yield surface. Yield surface is a separator convex surface between elastic and plastic regions. For strain hardened materials, yield surface changes the stresses beyond initial yield point according to hardening rule [13] [14].

Nonproportional loading produces additional cyclic hardening with respect to uniaxial or any proportional loadings. Therefore, it is expected that stress-strain curve of nonproportional loading is above proportional one which can be seen in Figure 2.2.3.
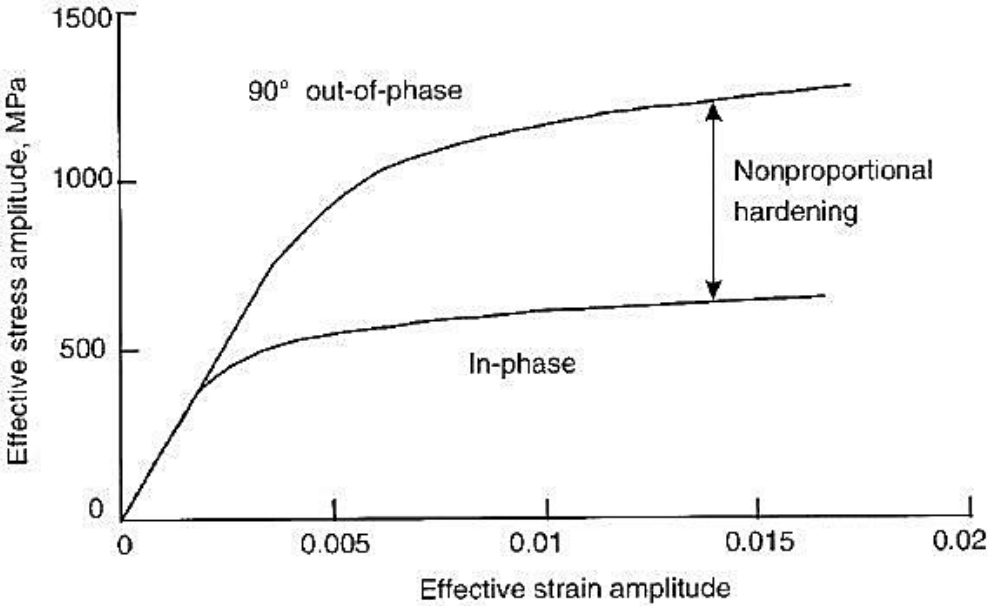
Figure 2.2.3 Cyclic stress-strain curve for proportional and nonproportional loading [9]

The reason of this additional hardening is interaction of slip planes, because slip systems are activated easily under nonproportional conditions due to the rotation of principal axes. Maximum Nonproportional hardening is seen with 90° out of phase loading path. In addition, amount of hardening is highly related to microstructure of the material [8, pp. 44-61] [10].

For some materials like 1100 aluminum, proportional and nonproportional behaviors are same; whereas, they are totally different for stainless steels [13].

2.3   Mean Stress

Mean stress has an important effect on fatigue life of components. Moreover, according to Papuga, effect of mean stress is much more important and dominant than out of phase loadings [15].Tensile mean normal stress has a tendency to decrease the fatigue life or compressive mean stress increases it; on the contrary, non-zero mean shear stress does not have an effect on fatigue life if it is lower than the material shear yield stress [16] [17].

Sines et al [18] ran some experiments to establish the effect of mean stress. These experiments include; cyclic axial with static tension and compression, cyclic torsion with static torsion, cyclic bending with static torsion and cyclic torsion with static bending.

Figure 2.3.1 shows that effect of static tension or compression is linear as long as the maximum stress does not exceed the yield strength of the material.
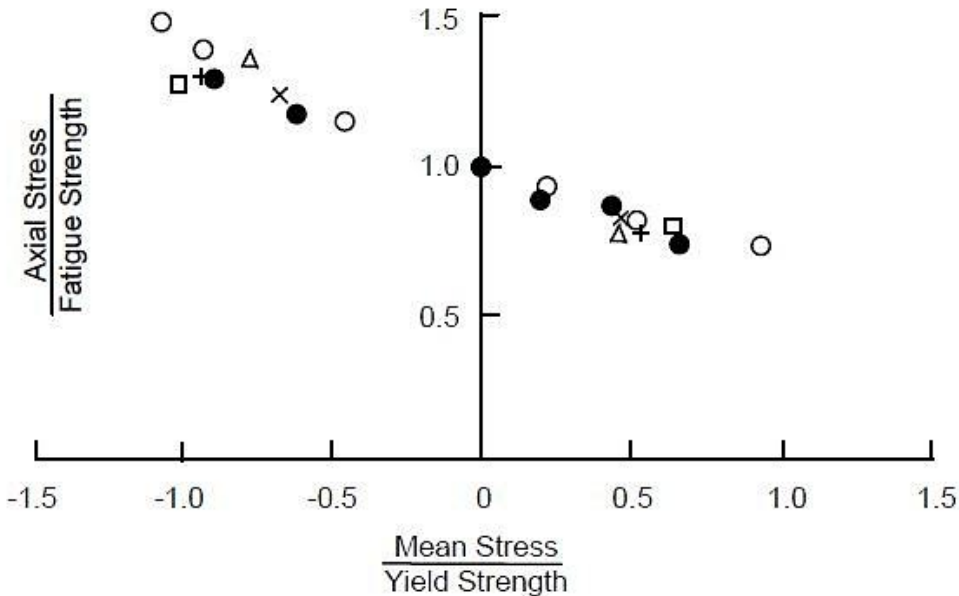
Figure 2.3.1 Cyclic axial stress with static tension and compression [8, pp. 129-169]

Figure 2.3.2 shows that torsional mean stress does not have any effect on fatigue as long as maximum shear stress remains below the yield strength of the material.
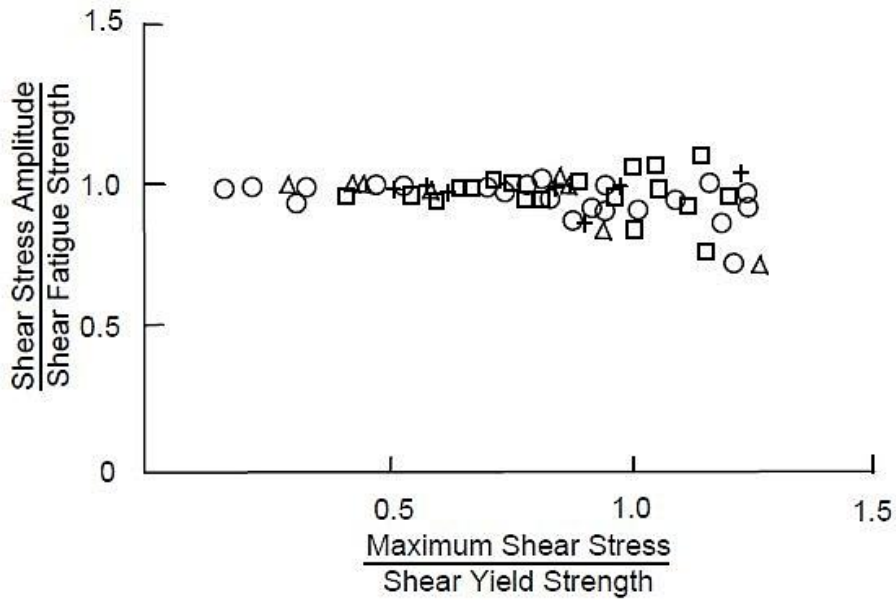
Figure 2.3.2 Cyclic torsion with static torsion [8, pp. 129-169]

Figure 2.3.3 shows that torsional mean stress does not affect the fatigue limit in reversed bending as long as the torsional yield strength is not exceeded by at least 50%.
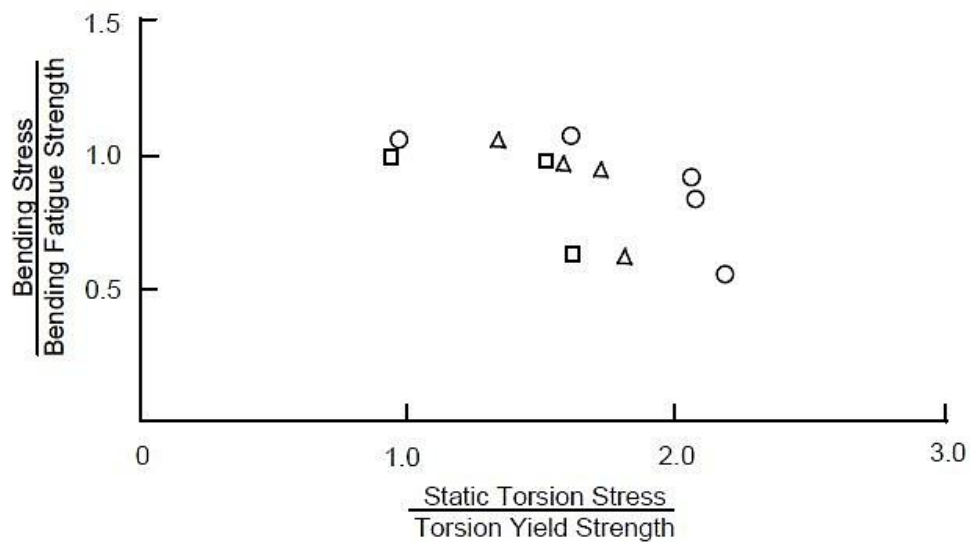
Figure 2.3.3 Cyclic bending with static torsion [8, pp. 129-169]

Figure 2.3.4 shows that effect of static tension on cyclic torsion results with the linearity between the amplitude of alternating torsion and the static tensile stress.
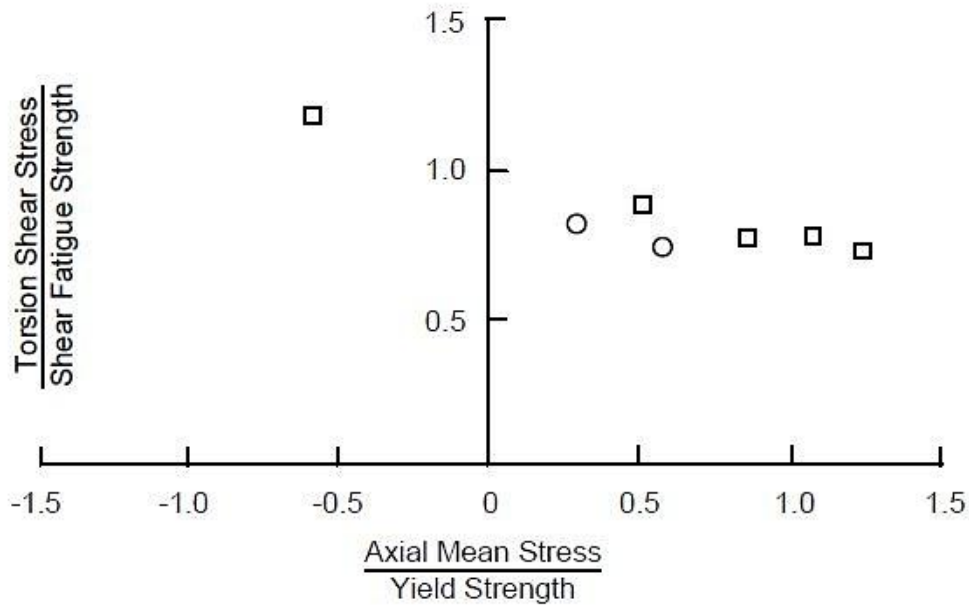
Figure 2.3.4 Cyclic torsion with static tension and compression [8, pp. 129-169]

For uniaxial fatigue, effect of mean stress is described by the general model of Marin. That is

$$\left(\sigma_{x,a}/f_{-1}\right)^n + \left(f\, \sigma_{x,m}/\sigma_{UTS}\right)^m = 1$$

Equation 2.3.1

where f_{-1} is fully reversed axial fatigue limit, $\sigma_{x,a}$ and $\sigma_{x,m}$ are nominal stress amplitude and nominal mean stress, respectively; and also, n, m, and f are constants. Constants change according to the model. For some models;

- Soderberg: n= 1, m= 1, $f = \sigma_{UTS}/\sigma_Y$,
- Goodman: n= 1, m= 1, f= 1,
- Gerber: n= 1, m= 2, f= 1,
- Dietman: n= 2, m= 1, f= 1,
- the so-called elliptical relationship: n= 2, m= 2, f= 1.

These models are compared with the experimental data in Figure 2.3.5 [17].
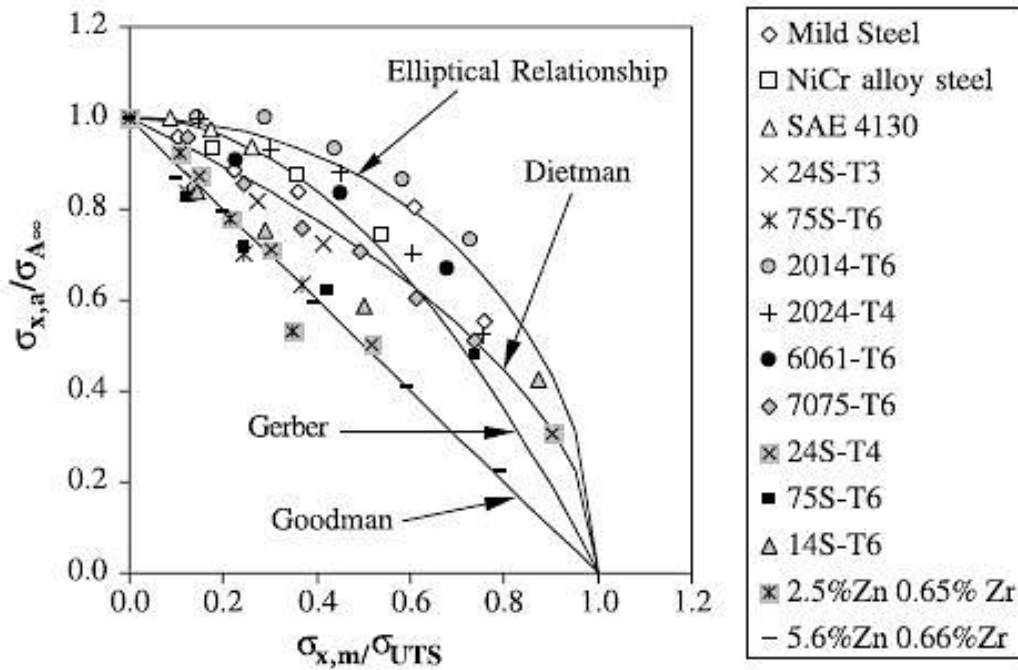
Figure 2.3.5 Comparison of experimental data with the models for uniaxial fatigue [17]

2.4 Multiaxial Fatigue Models

Multiaxial fatigue takes place due to the presence of axial, bending and/or torsion type of loadings together, at least two a of them at the same time.

There are two basic approaches for these problems; low cycle fatigue (under the condition of plastic deformation) and high cycle fatigue. For the former strain based models, for the latter stress based models are suggested to predict the multiaxial fatigue limit [19]. In this section, high cycle multiaxial fatigue will be mentioned with stress based models.

As mentioned before, the most important threshold for high cycle fatigue is crack nucleation. Therefore, the aim of the models is prediction of multiaxial fatigue limit in order to separate the stress space as safe and unsafe regions [1] [20].

Before mentioning the models, some stress quantities should be understood.

Firstly, components of stress under multiaxial conditions (Figure 2.4.1);
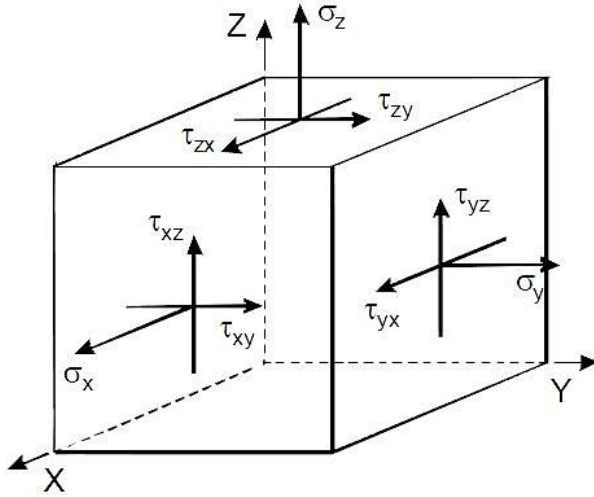
Figure 2.4.1 Components of stress in three dimensions [21]

These components can be separated as hydrostatic (σ) and deviatoric (τ) stresses. In the matrix form they can be written as Cauchy stress tensor that defines all the components of state of stress at a point.

$$\sigma = \begin{bmatrix} \sigma_{11} & \sigma_{12} & \sigma_{13} \\ \sigma_{21} & \sigma_{22} & \sigma_{23} \\ \sigma_{31} & \sigma_{32} & \sigma_{33} \end{bmatrix} \equiv \begin{bmatrix} \sigma_{xx} & \sigma_{xy} & \sigma_{xz} \\ \sigma_{yx} & \sigma_{yy} & \sigma_{yz} \\ \sigma_{zx} & \sigma_{zy} & \sigma_{zz} \end{bmatrix} \equiv \begin{bmatrix} \sigma_{x} & \tau_{xy} & \tau_{xz} \\ \tau_{yx} & \sigma_{y} & \tau_{yz} \\ \tau_{zx} & \tau_{zy} & \sigma_{z} \end{bmatrix}$$

Secondly, stress invariants; some models are based on mean hydrostatic stress tensor and stress deviator tensor. They are directly related to stress invariants and deviatoric stress invariants, especially I_1 and $\sqrt{J_{2,a}}$ [1]. When the applied load is uniaxial or in-phase multiaxial, I_1 and $\sqrt{J_{2,a}}$ are equal to;

$$I_1 = \sigma_x + \sigma_y + \sigma_z$$

Equation 2.4.1

$$\sqrt{J_{2,a}} = \left[\frac{1}{6} \left\{ \left(\sigma_{x,a} - \sigma_{y,a} \right)^2 + \left(\sigma_{y,a} - \sigma_{z,a} \right)^2 + \left(\sigma_{z,a} - \sigma_{x,a} \right)^2 + 6 \left(\tau_{xy,a}^2 + \tau_{yz,a}^2 + \tau_{zx,a}^2 \right) \right\} \right]^{1/2}$$

Equation 2.4.2

For out-of-phase multiaxial fatigue loading, calculation of $\sqrt{J_{2,a}}$ is complicated. It changes from author to author. $\sqrt{J_{2,a}}$ represents the equivalent shear stress amplitude and within each cycle its direction and magnitude changes. It can be seen on Figure 2.4.2, how $\sqrt{J_{2,a}}$ changes along the cycle on a proportional and nonproportional loading [1].

16
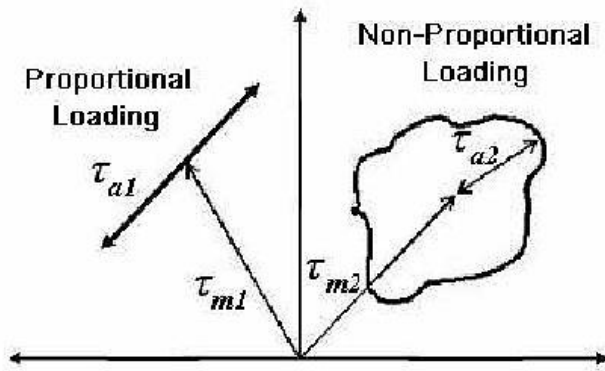
Figure 2.4.2 Behavior of the shear stress amplitude under proportional and nonproportional loading [1]

Thirdly, some models use stress quantities on specific planes. Δ sign in Figure 2.4.3 represents the plane under consideration. Stress acting on Δ is S_n which has the projection normal to the Δ as N and orthogonal projection on Δ as C. N is the normal stress vector and C is the shear stress vector.
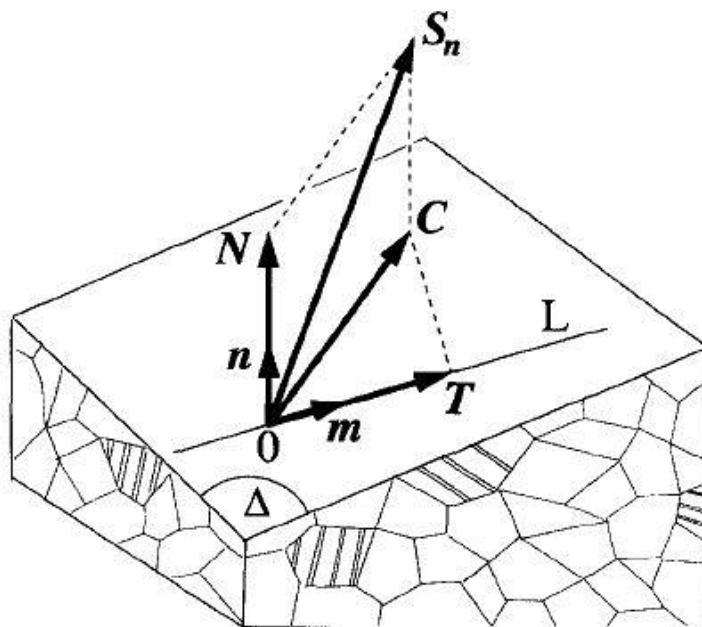
Figure 2.4.3 Stresses on plane Δ [20]

Another quantity is T which is the resolved shear stress vector. It is the shear stress acting along a slip line L of the plane Δ and is equal to the projection of shear stress C on this line (Figure 2.4.3) [20].

2.4.1   Stress Based Models

Most valid stress based models for high cycle fatigue can be classified into three categories; stress invariant, critical plane and average stress approach.

2.4.1.1 Stress Invariant Approach

This approach is based on hydrostatic stress and invariant of the stress deviator.

2.4.1.1.1   Sines Criterion

This criterion [18] is one of the oldest and famous models. It is the combination of equivalent shear stress amplitude, $\sqrt{J_{2,a}}$ and mean hydrostatic stress, $\sigma_{H,mean}$ [1].

$$\sqrt{J_{2,a}} + k\sigma_{H,mean} \leq \beta$$

Equation 2.4.3

where k and β are material constants which are obtained from repeated tension limit, f_0, and fully reversed torsion limit, t_{-1}.

$$k = \left(\frac{3t_{-1}}{f_o}\right) - \sqrt{3}; \ \beta = t_{-1}$$

Equation 2.4.4

Disadvantages of this criterion are; f_0 is rarely available to researchers, predictions are non-conservative for brittle metals, effect of mean stress is only used via mean hydrostatic stress which is not enough, application of this criterion under fully reversed bending results with the constant ration of $^{t_{-1}}/_{f_{-1}} = ^{1}/_{\sqrt{3}}$ for all metals; however, it varies from 0.5 for mild metals to 1 for brittle metals [15] [1] [20].

2.4.1.1.2   Crossland Criterion

The difference with Sines is that Crossland [22] considers the influence of the maximum hydrostatic stress, $\sigma_{H,max}$.

$$\sqrt{J_{2,a}} + k\sigma_{H,max} \leq \beta$$

Equation 2.4.5

where k and β are material constants which are obtained from fully reversed bending limit, f_{-1}, and fully reversed torsion limit, t_{-1}.

$$k = \left(\frac{3t_{-1}}{f_{-1}}\right) - \sqrt{3}; \ \beta = t_{-1}$$

Equation 2.4.6

By the change of the incorporation of mean stress, this criterion predicts much more better results than Sines; however its applicability to out-of-phase loading is poor [15].

2.4.1.2 Critical Plane Approach

This approach is based on a specified plane, Δ, which is the most severely loaded in the material and governs the fatigue process by nucleation of the fatigue crack on it. This plane changes model to model due to the different approaches to critical planes like maximum shear stress observed plane or maximum damaged plane, etc. Δ is searched via finding the normal and shear stress amplitudes and mean values on each possible Δ plane that passes by the point of interest [1].

Stresses on a defined plane are mentioned before. Under proportional cyclic loading conditions, shear stress vector, C, changes in magnitude and in direction; therefore, tip of C draws a closed curve Ψ on plane Δ. Then a circle is drawn around this curve which is unique and called minimum circumscribed circle. This circle's center point is defined by C_m and radius of this circle is C_a which can be seen in Figure 2.4.4 [20].
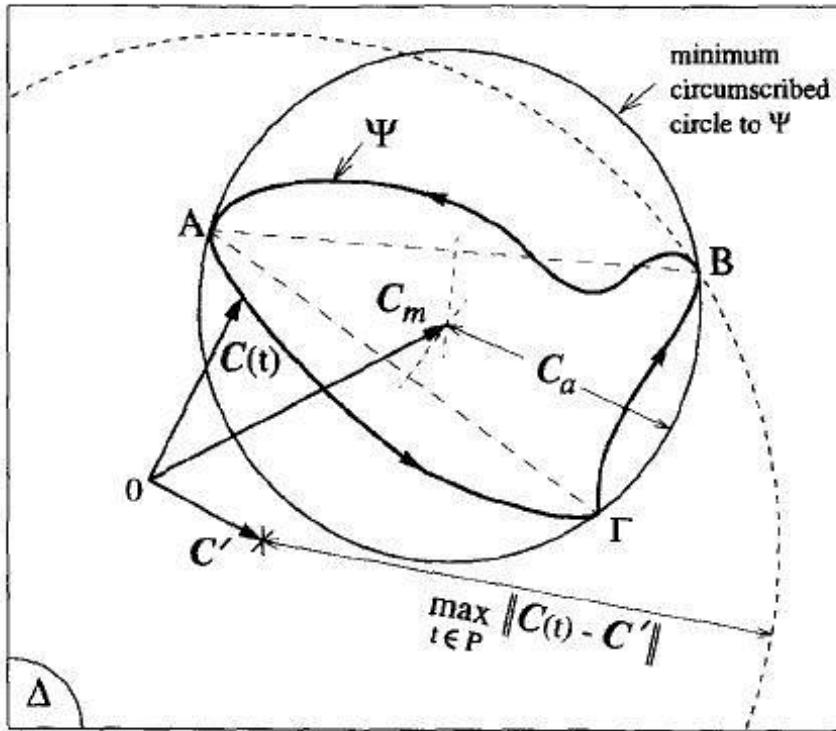
Figure 2.4.4 Construction of minimum circumscribed circle [20]

Also, resolved shear stress vector on Δ, T, changes only in magnitude so it moves back and forth between points A and Z on line L. Thus, T_a, and T_m are defined as in Figure 2.4.5 [20].
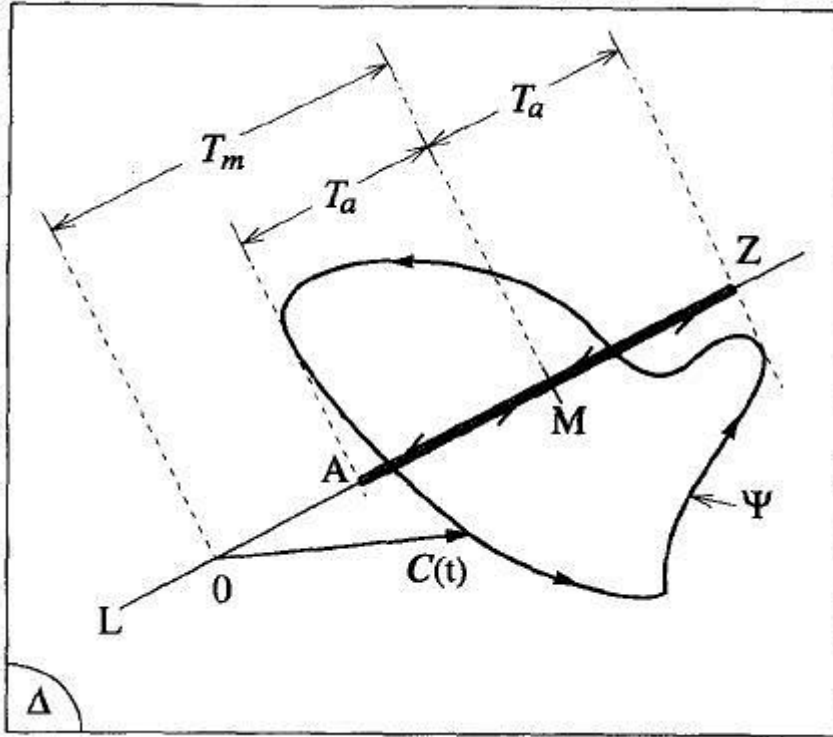
Figure 2.4.5 Definition of T$_a$ and T$_m$ [20]

2.4.1.2.1   Matake Criterion

Mateke criterion [23] uses a damage parameter of the linear combinations of C_a and N_{max} acting on the critical plane where shear stress reaches the maximum value. His criterion is formulized as;

$$C_a(\varphi^*, \theta^*) + \kappa N_{max}(\varphi^*, \theta^*) \leq \beta$$

Equation 2.4.7

where κ and β are material parameters, and (φ^*, θ^*) are the spherical coordinates of the critical plane [20] [24].

$$\kappa = \left(\frac{2t_{-1}}{f_{-1}}\right) - 1 \text{ and } \beta = t_{-1}$$

Equation 2.4.8

2.4.1.2.2 McDiarmid Criterion

Damage parameter and critical plane are same as Matake's model. Only difference is that McDiarmid [25] considers the concept of Case A and Case B cracks (Brown and Miller [26]). Case A crack propagates along the surface and case B crack propagates inwards toward the surface. Case B is more severe than A. McDiarmid's formula is

$$C_a(\varphi^*, \theta^*) + \frac{t_{A,B}}{2\sigma_f} N_{max}(\varphi^*, \theta^*) \leq t_{A,B}$$

Equation 2.4.9

where σ_f is ultimate tensile strength and $t_{A,B}$ is the fatigue limit depending on which case the critical plane corresponds to [16] [20].

2.4.1.2.3 Dang Van Criterion

Dang Van's criterion [27] is based on a linear combination of maximum mesoscopic shear stress and hydrostatic shear stress on the critical plane. This criterion is different from regular critical plane approaches; it considers the process at the mesoscopic scale which is a scale between micro and macro scales (Figure 2.4.6). According to Dang Van, crack nucleation is a local process which takes place in grains that are under the stress of plastic deformation [8, pp. 129-169].

This criterion's general formula is:

$$\tau(t) + a\sigma_H(t) = \beta$$

Equation 2.4.10

where $\tau(t)$ and $\sigma_H(t)$ are instantaneous microscopic shear stress and hydrostatic stress; and, a and β are material constants. These microscopic stresses are different from macroscopic stresses because material is not homogeneous or isotropic at the microstructural scale [8, pp. 129-169].

$$a = \frac{t_{-1} - \frac{f_{-1}}{2}}{\frac{f_{-1}}{3}}$$

$$\beta = t_{-1}$$

Equation 2.4.11
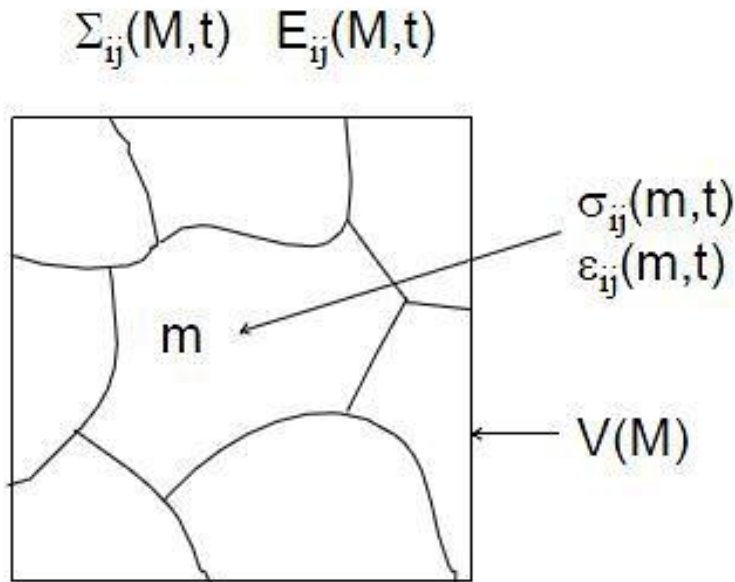
Figure 2.4.6 Microscopic, macroscopic stresses and strains $\Sigma_{ij}(M, t)$ **is macroscopic stresses,** $E_{ij}(M, t)$ **is macroscopic strains,** $\sigma(M, t)$ **is microscopic stresses,** $\varepsilon(M, t)$ **is microscopic strains,** $V(M)$ **is elementary volume and all of them are functions of position within the structure, M, and/or time [8, pp. 129-169]**

The plastic shear deformation of the grains with the most severe orientations is constrained due to the elastic behavior of neighboring grains having less severe orientations. As loading continues, the hardening takes place as kinematic and isotropic hardening. In order to find the local stresses, ρ^* has to be considered that is stabilized residual stress tensor. It represents the hardening of the material.

Therefore the resulting microscopic stresses are;

$$\sigma_{ij}(t) = \Sigma_{ij}(t) + dev\rho^*$$

Equation 2.4.12

where $dev\rho^*$ is the deviatoric part of the stabilized residual tensor [8, pp. 129-169].

Moreover, microscopic shear stress, $\tau(t)$, is calculated by the theory of Tresca maximum shear stress.

$$\tau(t) = \frac{1}{2}[\sigma_1(t) - \sigma_3(t)]$$

Equation 2.4.13

where $\sigma_1(t)$ and $\sigma_3(t)$ are microscopic principal stresses.

23

This criterion can be described with graph of $\tau(t)$ and σ_H, which are the main parameters of this criterion. It creates two zones that are safe and unsafe, respectively. If the loading path crosses the boundaries, material will have fatigue failure; if it stays within the boundaries it will have an infinite life (Figure 2.4.7) [8, pp. 129-169].
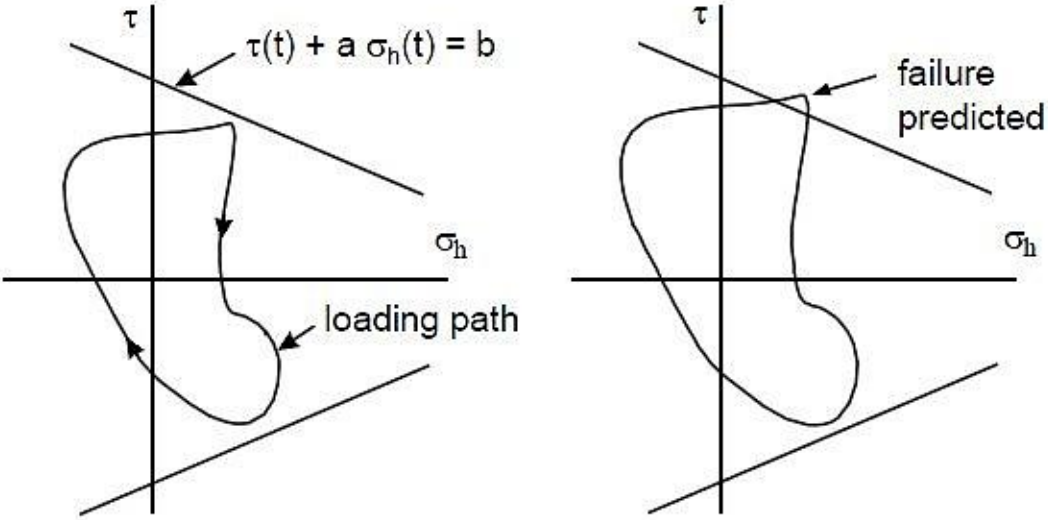
Figure 2.4.7 Application of Dang Van criterion [8, pp. 129-169]

2.4.1.3 Integral Approach (Average Stress Approach)

In this approach, the equivalent stress acting on plane (Δ) is calculated within a specified volume (V). It considers all the possible angles of Δ within V.

2.4.1.3.1   Liu and Zenner Criterion

This criterion [28] is the functions of the stresses on the intersection plane which are $\sigma_a(\varphi,\theta)$, $\sigma_m(\varphi,\theta)$, $\tau_a(\varphi,\theta)$, and $\tau_m(\varphi,\theta)$ as seen in Figure 2.4.8.
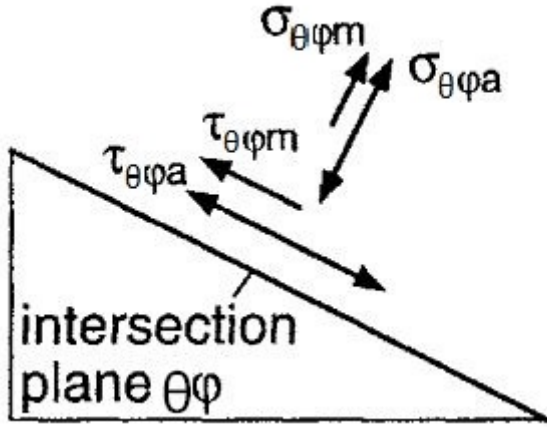
Figure 2.4.8 Stress components in an intersection plane [28]

And its general formula is:

$$a\tau_{eq,a}^2 + b\sigma_{eq,a}^2 + c\tau_{eq,m}^2 + d\sigma_{eq,m} \leq f_{-1}^2$$

Equation 2.4.14

where $\tau_{eq,a}$ and $\tau_{eq,m}$ are particular averages of the shear stresses amplitude and mean shear stresses acting on possible planes of Δ within volume V. They are defined as;

$$\tau_{eq,a} = \left[\frac{15}{8\pi} \int_{\theta=0}^{\pi} \int_{\varphi=0}^{2\pi} \tau_a^2(\varphi,\theta) \sin\theta \, d\varphi \, d\theta\right]^{1/2}$$

$$\tau_{eq,m} = \frac{1}{\tau_{eq,a}} \left[\frac{15}{8\pi} \int_{\theta=0}^{\pi} \int_{\varphi=0}^{2\pi} \tau_a^2(\varphi,\theta)\tau_m^2(\varphi,\theta) \sin\theta \, d\varphi \, d\theta\right]^{1/2}$$

Equation 2.4.15

And also, $\sigma_{eq,a}$ and $\sigma_{eq,m}$ are specific averages of the normal stress amplitude and mean value acting on plane Δ. They are defined as;

$$\sigma_{eq,a} = \left[\frac{15}{8\pi} \int_{\theta=0}^{\pi} \int_{\varphi=0}^{2\pi} \sigma_a^2(\varphi,\theta)\sin\theta \, d\varphi \, d\theta\right]^{1/2}$$

$$\sigma_{eq,m} = \frac{1}{\sigma_{eq,a}^2} \left[\frac{15}{8\pi} \int_{\theta=0}^{\pi} \int_{\varphi=0}^{2\pi} \sigma_a^2(\varphi,\theta)\, \sigma_m(\varphi,\theta)\sin\theta \, d\varphi \, d\theta\right]$$

Equation 2.4.16

One disadvantage of this model is that needs four stress quantities to calculate parameters a, b, c, and d which are functions of f_{-1}, f_0, t_{-1}, and t_0 [29].

$$a = \frac{1}{5}\left[3\left(\frac{f_{-1}}{t_{-1}}\right)^2 - 4\right]$$

$$b = \frac{1}{5}\left[6 - 2\left(\frac{f_{-1}}{t_{-1}}\right)^2\right]$$

$$c = \frac{f_{-1}^2 - \left(\frac{f_{-1}}{t_{-1}}\right)^2\left(\frac{t_0}{2}\right)^2}{\frac{4}{7}\left(\frac{t_0}{2}\right)^2}$$

$$d = \frac{f_{-1}^2 - \left(\frac{f_0}{2}\right)^2 - \frac{4c}{21}\left(\frac{f_0}{2}\right)^2}{\frac{5}{7}\left(\frac{f_0}{2}\right)}$$

Equation 2.4.17

However, Liu and Zenner proposed an easy formula (Equation 2.4.18) for t_0 and the concept of mean stress sensitivity for f_0 which is shown in Figure 2.4.9 and the formulae on the Figure 2.4.9.

$$t_0 = \frac{4t_{-1}}{\frac{2f_{-1}}{f_0} + 1}$$

Equation 2.4.18
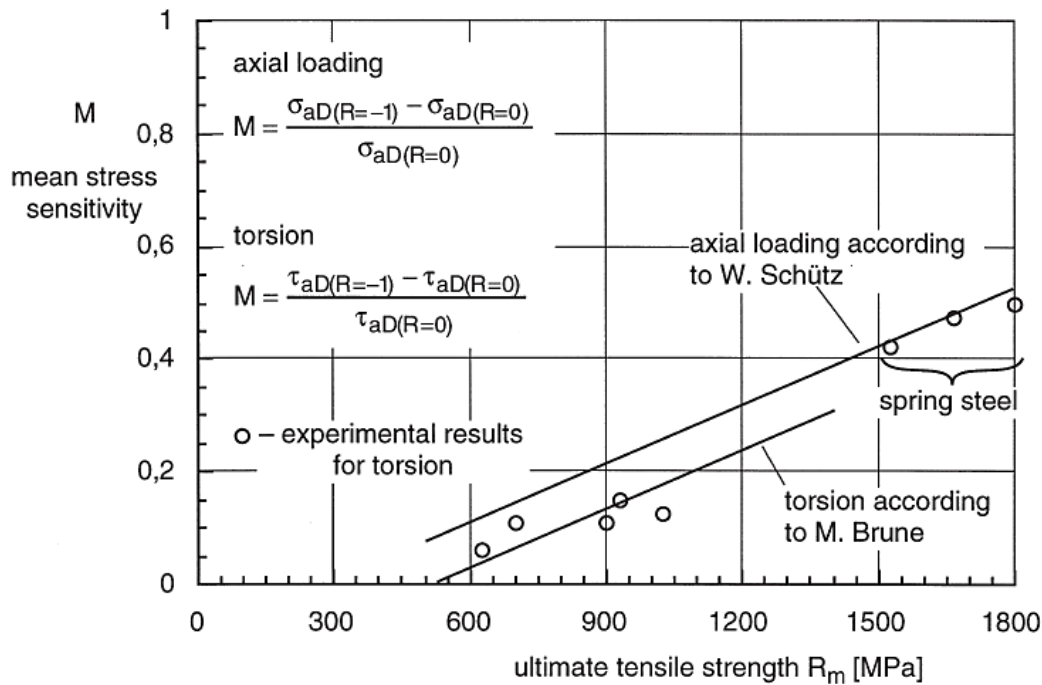
Figure 2.4.9 Mean stress sensitivity for axial loading and torsion [30]

This criterion belongs to ductile materials and limited to range of $0.577 < {}^{t_{-1}}\!/_{f_{-1}} < 0.866$ otherwise a or b might be negative.

Zenner et al [30] tested the material at 3 different phase differences and calculated their fatigue limits. That was concluded that under nonproportional loadings phase difference angle does not affect the fatigue limit. However; it is seen from Equation 2.4.15, it is claimed that superimposed static shear stress alter the fatigue limit.

According to Papadopoulos et al [29]; for τ_a and τ_m, Liu and Zener suggest an incorrect way of calculation that results with a non-unique value of τ_m under nonproportional condition.

2.4.1.3.2 Papadopoulos Criterion

After the works of Dang Van, in early seventies, on mesoscopic approach; in late eighties Papadopoulos developed his approach. In the mesoscopic approach, it is focused on the localized plastic strain, γ^p, on the material which causes the fatigue crack nucleation. For very high number of cycles (e.g. $\sim 10^6$ cycles) the accumulated plastic strain is proportional to resolved shear stress amplitude, T_a, and also independent from the mean resolved shear stress T_m. General formula of this criterion [4] is

$$\sqrt{\langle T_n^2 \rangle} + \alpha \sigma_{H,max} \leq \beta$$

Equation 2.4.19

where $\sqrt{\langle T_n^2 \rangle}$ is average value (volumetric root mean square) of T_n^2 within volume V. Its formula is mentioned below.

Under out-of-phase condition the path Ψ on plane Δ which is defined by C is seen in Figure 2.4.10.
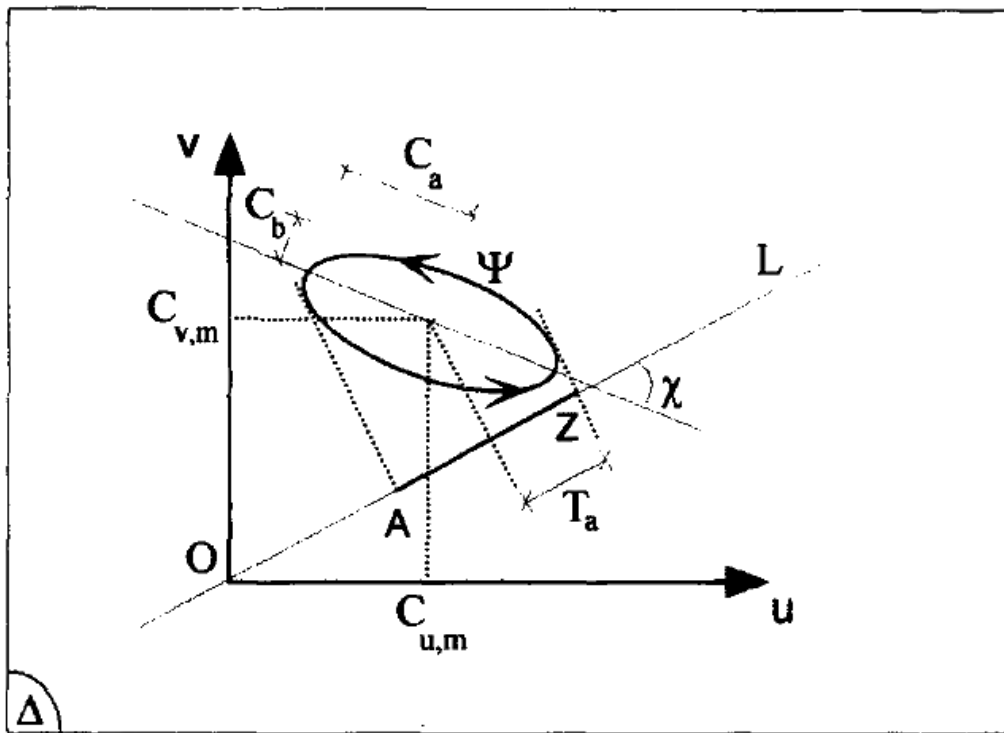
Figure 2.4.10 Elliptic path of Ψ on a plane Δ [4]

$$T_a = \sqrt{C_a^2 \cos^2 \chi + C_b^2 \sin^2 \chi}$$

Equation 2.4.20

where χ is the angle between line L and direction of the major axis of ellipse.

Then a new quantity is defined, T_n, which is the shear stress term of the general formula.

$$T_n(\varphi, \theta) = \sqrt{\frac{1}{2\pi} \int_{\chi=0}^{2\pi} \left(T_a(\varphi, \theta, \chi)\right)^2 d\chi}$$

$$\sqrt{\langle T_n^2 \rangle} = \sqrt{\frac{5}{4\pi} \int_{\varphi=0}^{2\pi} \int_{\theta=0}^{\pi} \left(T_n(\varphi, \theta)\right)^2 \sin \theta \, d\theta d\varphi}$$

Equation 2.4.21

After some calculations which can be found in Reference [4], $\sqrt{\langle T_a^2 \rangle}$ becomes

$$\sqrt{\langle T_n^2 \rangle} = \sqrt{\frac{\sigma_a^2}{3} + \tau_a^2}$$

Equation 2.4.22

In addition, the maximum hydrostatic stress is equal to

$$\sigma_{H,max} = \frac{\sigma_a + \sigma_m}{3}$$

Equation 2.4.23

Therefore, the formula becomes

$$\sqrt{\frac{\sigma_a^2}{3} + \tau_a^2} + \alpha \frac{\sigma_a + \sigma_m}{3} \leq \beta$$

Equation 2.4.24

where $\alpha = \frac{3t_{-1}}{f_{-1}} - \sqrt{3}$ and $\beta = t_{-1}$.

It is seen that under combined axial and torsional loading conditions the fatigue limit is independent of the phase difference angle. For this model, in order to keep the beneficial effect of compressive mean stresses t_{-1}/f_{-1} must be between 0.577 and 0.8 that corresponds to ductile metals.

3. Experimental Procedure

3.1   Introduction

Ten ductile iron specimens were tested at $R = \frac{\sigma_{min}}{\tau_{amp}} = -4$ and eight at R=-3 in the frequency range of 15-22.5 Hz under combination of compressive axial and torsional nonproportional loadings. This R ratio was decided on the basis of finite element analyses run by Tenaris (Figure 3.1.1). As seen in Figure 3.1.1 (y-axes is normalized with maximum negative stress) S22 and S23 are governing the fatigue by being the lowest compression and highest tensile stresses and their ratio is approximately R=-4. After these analyses, multiaxial fatigue tests were started with the general data mentioned in this section.
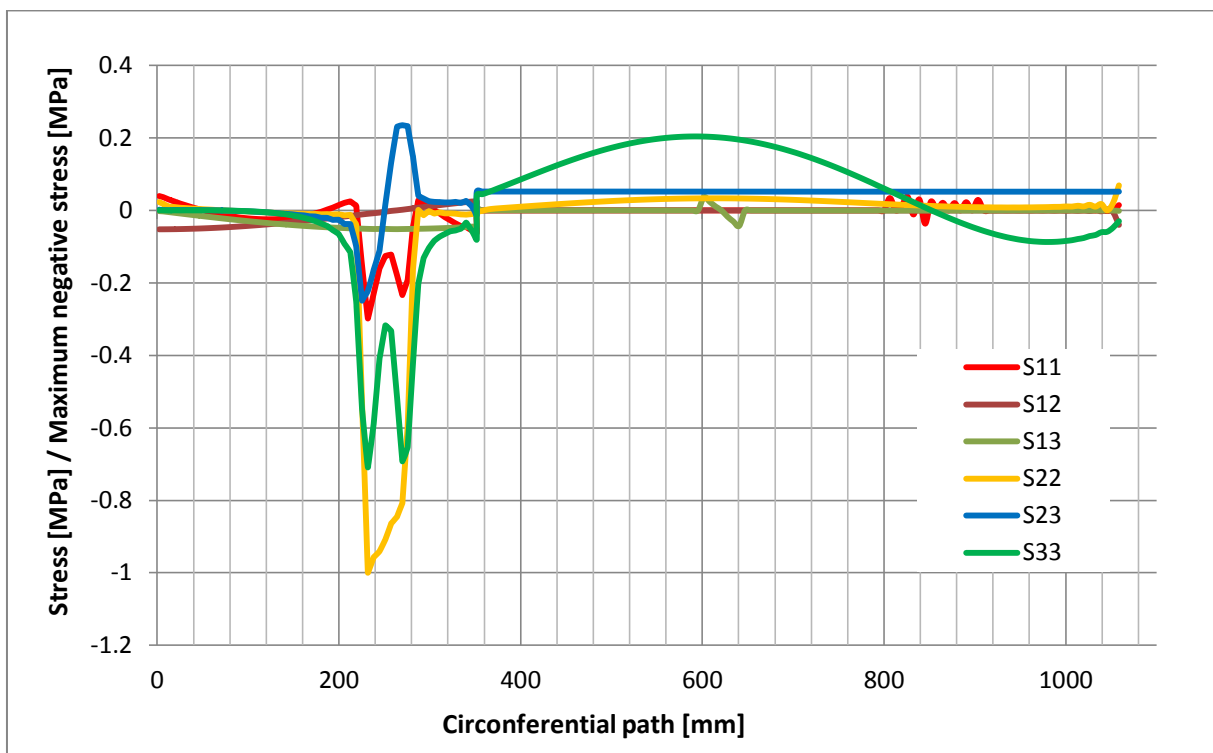
Figure 3.1.1 FEA of stress components

3.2   Material

3.2.1   General Information about the Material

The ductile irons (spheroidal cast iron) in this study were supplied in the name of SF1.

Cast irons can be classified according to their cooling rates from liquid form and compositions into two as: gray cast iron (high cooling rate) and white cast iron (low cooling rate). Gray cast irons divide into two types depending on graphite morphology as flake graphite iron, spheroidal graphite iron.

In this study, the material is ductile (spheroidal) cast iron. Spheroidal (nodular) cast irons are produced with the addition of minor elements that are magnesium, calcium, rare earth (cerium, lanthanum, etc.), and yttrium. These elements favor the formation of spheroidal graphite in order to have a relatively better material in strength and toughness than flake graphite iron [31].

However, excessive addition of some elements such as V, Mo, Cr, and Mn give rise to formation of carbides. Carbides increase the probability of shrinkage porosity formation by reducing the expansion effects produced by the formation of graphite during solidification [31].

As mentioned in Reference [31]: "Factors that promote shrinkage formation include lack of mold rigidity, unsuitable metal composition, incorrect pouring temperature, and a high degree of nucleation. These factors may operate independently or in combination."

3.2.2   Material Data

The material belongs to the ISO Standard 1083:2004 class of 700-2 which has the requirements of hardness in the range of 229-302 HB and fully pearlitic microstructure.

Brinell (HB) hardness values obtained from the investigated cast iron are shown in Table 3.2.1.

306	327	296	302	348	280
318	320	273	289	252	243
270	262	232	276	243	256

Table 3.2.1 Hardness values in Brinell

By calculating average of these data, 283 HB (300 HV10) was obtained.

Furthermore, chemical requirement ranges given to the supplier are shown below in Table 3.2.2 and it was seen that EDS data obtained via SEM fit these ranges.

	C	Si	Mn	Cr	Ni	Mo
Requirements	2.90-3.70	1.50-2.20	0.10-0.70	0.10-0.60	1.90-2.90	0.30-0.90

Table 3.2.2 Chemical composition range of the material (in weight %)

Metallographic examination was performed by two methods; optical microscope and SEM (Zeiss Evo 50) equipped with Oxford Instruments Inca X-Sight (X-ray microanalyzer).

The specimens were mechanically grounded and polished following to mounting. They were etched via Nital 2% in order to observe the microstructure of specimens. Moreover, fracture surfaces of broken specimens were observed via SEM by both secondary electron (SE) and quantitative back scattered electron (QBSE) modes.

The microstructure was observed as fully pearlitic by optical microscope as shown in Figure 3.2.1.
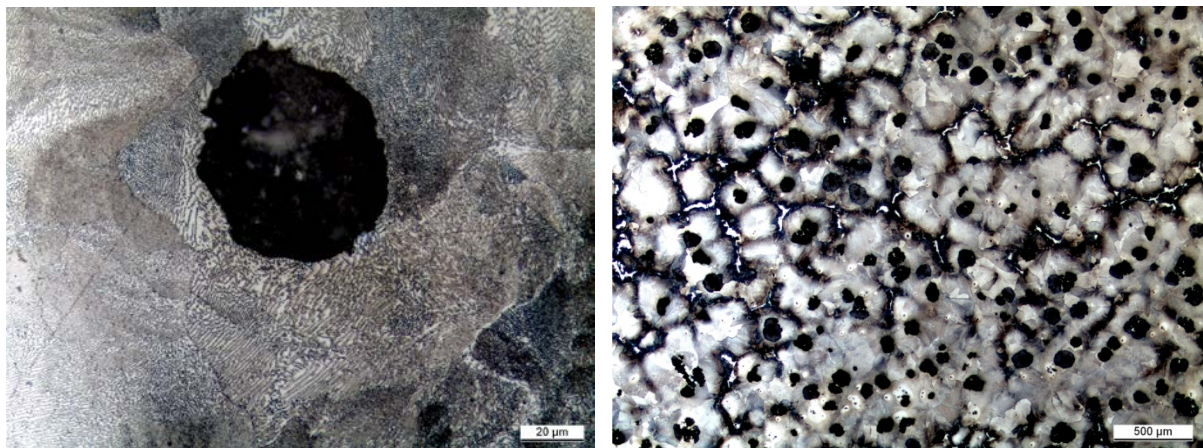
a) 500x magnification   b) 25x magnification

Figure 3.2.1 Microstructure of ductile iron a) Pearlite matrix, b) General view of the same specimen. Black circles are graphite nodules, white networks are intercellular carbides, black regions which are not circular are shrinkage porosities and the matrix is pearlite

In order to improve the fatigue properties of SF1, stress relieving heat treatment process was done (Figure 3.2.2). It eliminates tensile residual stresses remained from manufacturing and metalworking processes. This process does not involve major microstructural transformations.
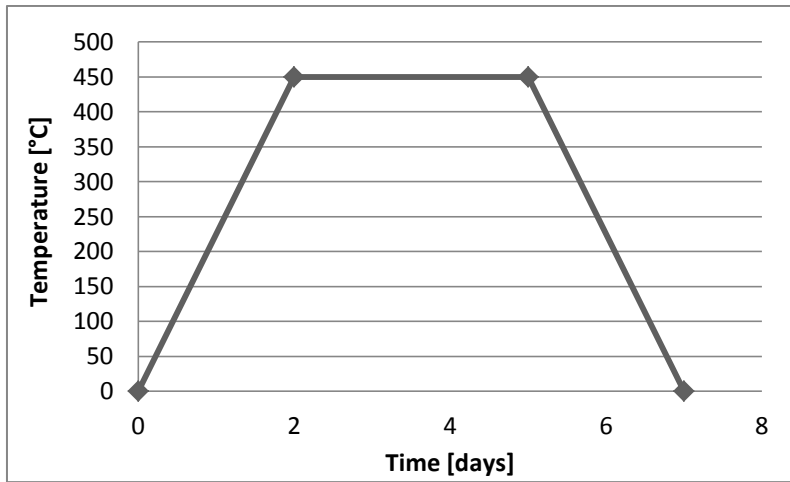
Figure 3.2.2 Stress relieving of SF1

Finally, pure axial and pure torsional fatigue limits were measured by Tenaris that are $f_{-1} = 196.5\ Mpa$ and $t_{-1} = 177.5\ Mpa$, respectively.

3.3 Experimental Method

3.3.1 Axial (Tensile) Fatigue Test

Axial fatigue tests were run at the laboratories of Tenaris Dalmine in the tensile direction, by applying staircase method with the steps of having stress difference of 40 MPa. The sequences of experiments were performed with the stress ratio of $R = \frac{\sigma_{min}}{\sigma_{max}} = -1$ (fully reversed).

Specimens used in these experiments had the diameter of 7 mm at their thinnest region.

3.3.2 Torsional Fatigue Test

Torsional fatigue tests were run at the laboratories of Tenaris Dalmine, by applying staircase method with the steps of having stress difference of 50 MPa. The sequences of experiments were performed with the stress ratio of $R = \frac{\sigma_{min}}{\sigma_{max}} = -1$ (fully reversed).

Specimens used in these experiments had the diameter of 16 mm at their thinnest region (same specimen dimensions in multiaxial tests).

3.3.3 Multiaxial Fatigue Test

Multiaxial tests were performed by means of Multiaxial Servohydraulic Test System – Walter+Bai LFV250–T2200 (Figure 3.3.1) that has limits of maximum axial dynamic force of 250 kN with 200 mm actuator stroke and maximum torque of 2200 Nm with ±50° torsional angle. Wedge grips were used for these tests and the specimen shape and dimensions according to Reference [32] are seen in Figure 3.3.2.

Figure 3.3.1 Multiaxial Servohydraulic Test System – Walter+Bai LFV250–T2200
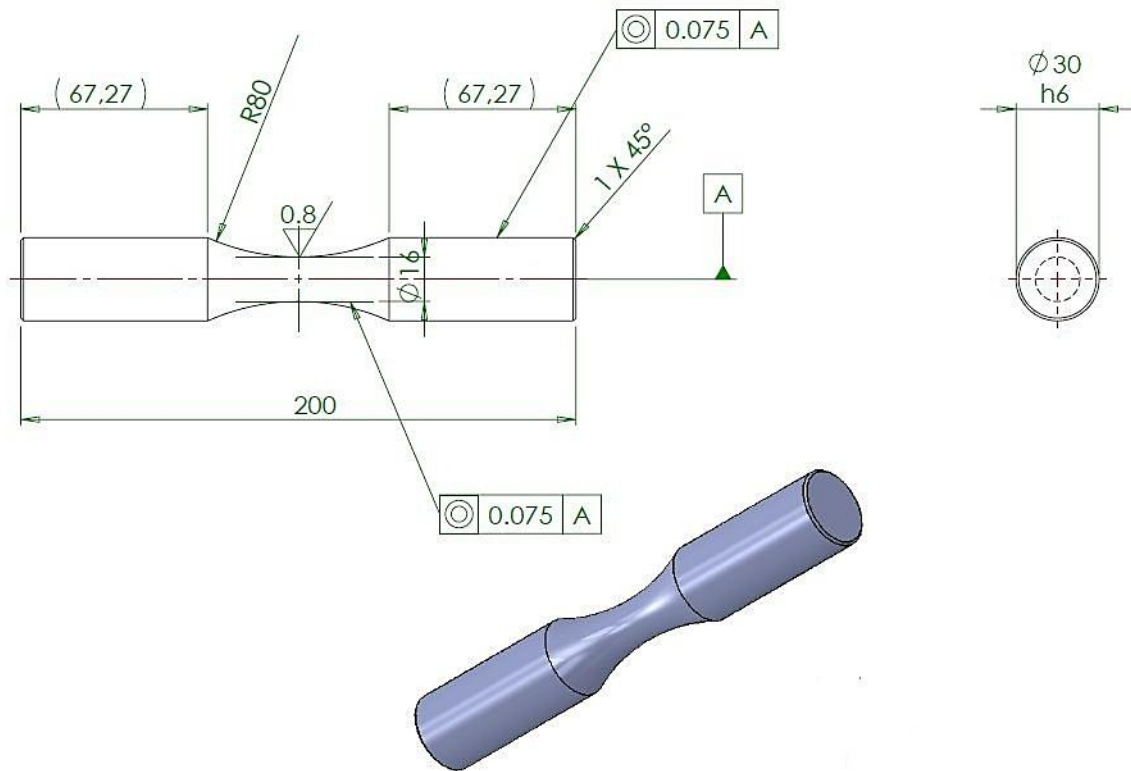
Figure 3.3.2 Dimensions of the specimen

SF1 specimens were cut from large section of cast iron and shaped to the actual form by the supplier as shown in Figure 3.3.3.

Figure 3.3.3 Cutting process of the specimen.

The sequences of experiments were performed in a manner of staircase. Staircase method is used widely because of its simplicity, and, in order to calculate the median value of fatigue strength and its standard deviation at a specific number of cycles that is 10^7 for this study. First specimen is tested at an initial stress level, which is the best guess from calculations made or experiences for median

fatigue strength. If that specimen fails before desired cycle number, for the next specimen, stress level is decreased; if not, increased.

The stress difference between stress levels should equal to the standard deviation but not obligatory. However, it cannot be larger than twice the value of the standard deviation [33] [34]. In this study, axial stress difference and torsional stress difference between all steps are 100 MPa and 50 MPa, respectively.

Ten specimens were tested at $R = \frac{\sigma_{min}}{\tau_{amp}} = -4$ and eight at $R = -3$ in frequency range of 15-22.5 Hz under combination of axial and torsion loadings. Frequencies were changed due to the vibration effect of the multiaxial testing system to the other experimental systems. Frequency difference is very narrow so it was considered that multiaxial fatigue limit is not affected.

Axial loading was always in compression with mean stress but torsional loading was fully reversed. Moreover, these loadings are nonproportional; there is a phase difference of 90°. Examples of sine curves are seen in Figure 3.3.4.
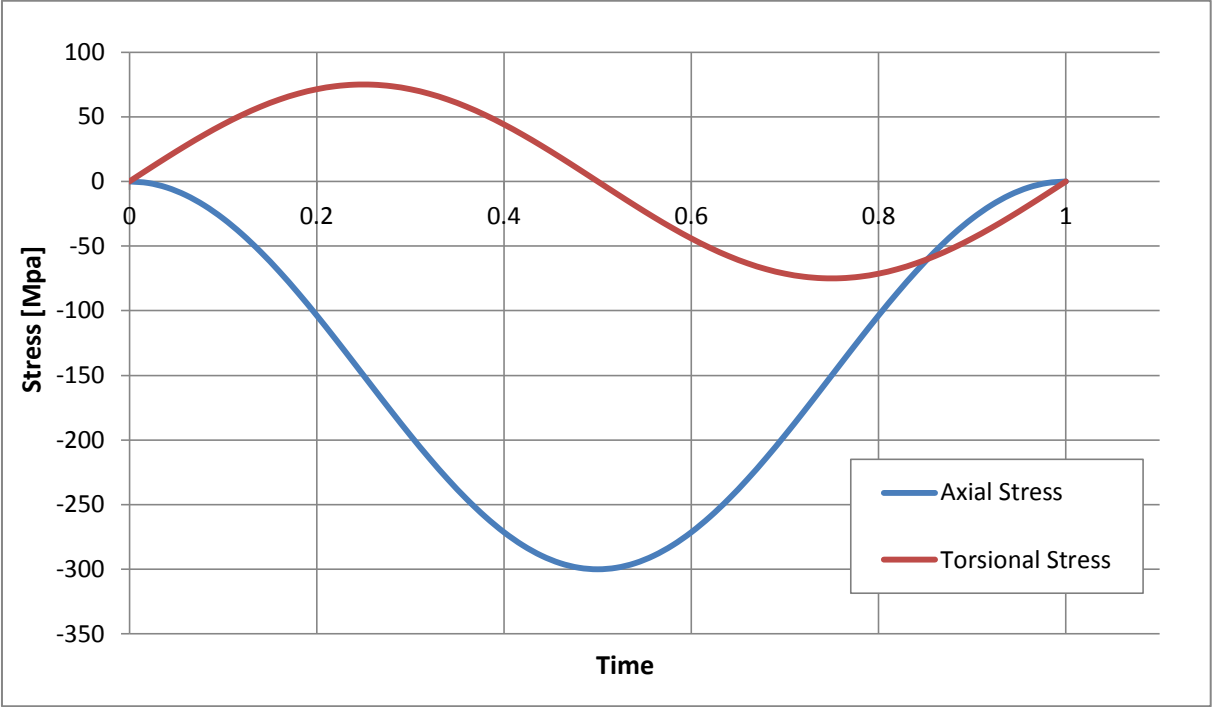
Figure 3.3.4 Sine curves of loadings at R=-4

4. Results and Discussion

4.1 Experimental Results

4.1.1 Results of Axial (Tensile) Tests

The 11 specimens were tested at the stress ratio of $R = \frac{\sigma_{min}}{\sigma_{max}} = -1$. Experimental results and the sequence of staircase method were reported in Table 4.1.1 and Table 4.1.2, respectively.

Test #	Spec. ID	Freq. [Hz]	$\Delta\sigma$ [MPa]	σ_{alt} [MPa]	σ_{mean} [MPa]	Cycle number	Result
1	3	120.2	480	240	0	12000000	Run-out
2	4	120	520	260	0	2457200	Failed
3	5	120	480	240	0	1386200	Failed
4	6	120.1	440	220	0	728800	Failed
5	7	120.1	400	200	0	8087100	Failed
6	8	120.2	360	180	0	11900000	Run-out
7	9	120.3	400	200	0	203000	Failed
8	10	120.2	360	180	0	4179200	Failed
9	11	120.2	320	160	0	2718600	Failed
10	30	120.1	280	140	0	12000000	Run-out
11	31	120.4	320	160	0	12000000	Run-out

Table 4.1.1 Results of axial experiments

$\Delta\sigma$ [MPa]	Test #											
	1	2	3	4	5	6	7	8	9	10	11	12
520		x										
480	o		x									
440				x								
400					x		x					
360						o		x				o
320									x		o	
280										o		

Table 4.1.2 Staircase table of axial experiments(x: failed, o: run-out)

By applying staircase method, the calculated axial fatigue limit for R=-1 is $\Delta\sigma = 393\ MPa$. This value was calculated with the method of Hodge-Rosenblatt [35] (explained detailed in Section 4.1.3).

4.1.2 Results of Torsional Tests

The 7 specimens were tested at the stress ratio of $R = \frac{\tau_{min}}{\tau_{max}} = -1$. Experimental results and the sequence of staircase method were reported in Table 4.1.3 and Table 4.1.4, respectively.

Test #	Spec. ID	$\Delta\tau$ [MPa]	τ_{alt} [MPa]	τ_{mean} [MPa]	Cycle number	Result
1	G3	380	190	0	976428	Failed
2	G4	330	165	0	10000000	Run-out
3	G6	380	190	0	879576	Failed
4	G8	330	165	0	10060006	Run-out
5	G9	380	190	0	777011	Failed
6	G5	330	165	0	10012590	Run-out
7	G7	380	190	0	1657797	Failed

Table 4.1.3 Results of torsional experiments

$\Delta\tau$	Test #							
[MPa]	1	2	3	4	5	6	7	8
380	x		x		x		x	
330		o		o		o		o

Table 4.1.4 Staircase table of torsional experiments(x: failed, o: run-out)

By applying staircase method, the calculated torsional fatigue limit for R=-1 is $\Delta\tau = 355\ MPa$. This value was calculated with the method of Hodge-Rosenblatt [35] (explained detailed in Section 4.1.3).

4.1.3 Results of Multiaxial Tests

The 18 specimens were tested at two different values of R=-4 and R=-3 (which is defined in Section 3.1). The first set was tested under cyclic compressive load and cyclic torsional load (R=-4) whose data are seen in Table 4.1.5 and the results were analyzed by means of staircase method [36] as reported in Table 4.1.6. Results and staircase method [36] of the second set, which was tested with R=-3, are reported in Table 4.1.7 and Table 4.1.8.

Test #	Spec. ID	Freq. [Hz]	$\Delta\sigma$ [MPa]	σ_{alt} [MPa]	σ_{mean} [MPa]	$\Delta\tau$ [MPa]	τ_{alt} [MPa]	τ_{mean} [MPa]	Cycle number	Result
1	3.6	22.5	600	300	-300	300	150	0	1337004	Failed
2	4.6	22.5	500	250	-250	250	125	0	10017026	Failed
3	2.6	22.5	400	200	-200	200	100	0	9172111	Run-out
4	5.6	15	500	250	-250	250	125	0	910812	Failed
5	6.6	22.5	400	200	-200	200	100	0	9317233	Failed
6	7.6	22.5	300	150	-150	150	75	0	10104404	Run-out
7	8.6	22.5	400	200	-200	200	100	0	10005347	Run-out
8	9.6	15	500	250	-250	250	125	0	3908321	Failed
9	10.6	15	400	200	-200	200	100	0	10000207	Run-out
10	1.7	15	500	250	-250	250	125	0	2708292	Failed

Table 4.1.5 Results of multiaxial experiments (R=-4)

$\Delta\sigma$ [MPa]	$\Delta\tau$ [MPa]	1	2	3	4	5	6	7	8	9	10	11
600	300	x										
500	250		x		x				x		x	
400	200			o		x		o		o		o
300	150						o					

(Test #)

Table 4.1.6 Staircase table R=-4 (x: failed, o: run-out)

Test #	Spec. ID	Freq. [Hz]	$\Delta\sigma$ [MPa]	σ_{alt} [MPa]	σ_{mean} [MPa]	$\Delta\tau$ [MPa]	τ_{alt} [MPa]	τ_{mean} [MPa]	Cycle number	Result
11	3.7	15	450	225	-225	300	150	0	993165	Failed
12	4.7	22.5	375	187.5	-187.5	250	125	0	10007033	Run-out
13	6.7	15	450	225	-225	300	150	0	1124024	Failed
14	5.7	15	375	187.5	-187.5	250	125	0	5944760	Failed
15	7.7	22.5	300	150	-150	200	100	0	10003288	Run-out
16	8.7	15	375	187.5	-187.5	250	125	0	2577235	Failed
17	10.7	15	450	225	-225	300	150	0	1397668	Failed
18	9.7	15	375	187.5	-187.5	250	125	0	10192777	Run-out

Table 4.1.7 Results of multiaxial experiments (R=-3)

$\Delta\sigma$ [MPa]	$\Delta\tau$ [MPa]	Test #								
		11	12	13	14	15	16	17	18	19
450	300	x		x			x			o
375	250		o		x		x		o	
300	200					o				

Table 4.1.8 Staircase table R=-3 (x: failed, o: run-out)

By applying staircase method, the calculated multiaxial fatigue limit for R=-4 is $\Delta\sigma = 430\ MPa$, $\sigma_{mean} = -215\ MPa$, $\Delta\tau = 215\ MPa$ and for R=-3 it is $\Delta\sigma = 400\ MPa$, $\sigma_{mean} = -200\ MPa$, $\Delta\tau = 267\ MPa$. These values were calculated with the method of Hodge-Rosenblatt [35]. The formulae used for these calculations are defined below:

$$\Delta\sigma = \frac{\sum_{i=1}^{n}(\Delta\sigma)_i + \Delta\sigma_{fe}}{n+1}$$

$$\Delta\tau = \frac{\sum_{i=1}^{n}(\Delta\tau)_i + \Delta\tau_{fe}}{n+1}$$

Equation 4.1.1

where n is number of experiments performed, $(\Delta\sigma)_i$ and $(\Delta\tau)_i$ are the applied axial and torsional stress ranges. Moreover, the method implies the use of a fictitious step (see red colored Test #11 in Table 4.1.6 and Test #19 in Table 4.1.7) to be added at the end of the stair case as the last stress level: for axial stress $\Delta\sigma_{fe}$ and for torsional $\Delta\tau_{fe}$. For R=-4 case, they are $\Delta\sigma_{fe} = 400\ MPa$ and $\Delta\tau_{fe} = 200\ MPa$.

Within these calculations, Test #1 has been discarded due to the high stress predictions made in the beginning of the staircase method.

The tests were defined as run-out when they reach to 10^7 cycles; the failed condition was defined when the crack could be observed visually during the experiments except Specimen 3.6 that failed during test, and Specimen 4.6 that was considered as well a failed specimen even if completed the 10^7 cycles because exhibited a visual crack during test. Based on this observation we decided to interrupt the tests at the moment when a visual crack appears. This explains why most of the fatigue zones of the specimens are not large.

Failed specimens were submerged into the liquid nitrogen and then separated by multiaxial test system in order to keep their fracture surfaces as same in the experiments.

Run-out specimens were broken in multiaxial test system under higher stresses in order to have the fracture surface led by defects.

In the next section the fracture surfaces and defect dimensions of axial, torsional and multiaxial specimens for both cases of R=-4 and R=-3, which are essential to understand the mechanism of multiaxial fatigue.

4.2 Fractography

4.2.1 Fractography of Axial Test Specimens

All the axial test specimens were observed and it was seen that all of them have shrinkage porosities (Figure 4.2.1) in different dimensions which are reported in Table 4.2.1. Moreover, the fatigue zones are fully covered with striation marks as seen in Figure 4.2.2 and Figure 4.2.3.
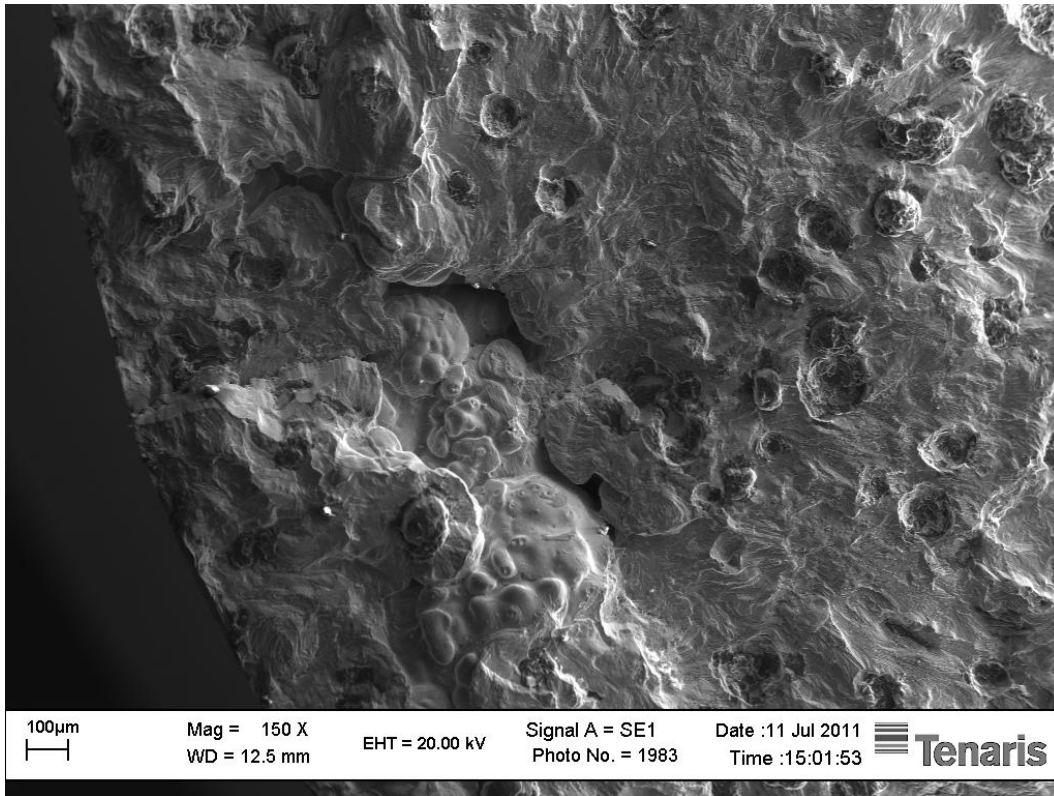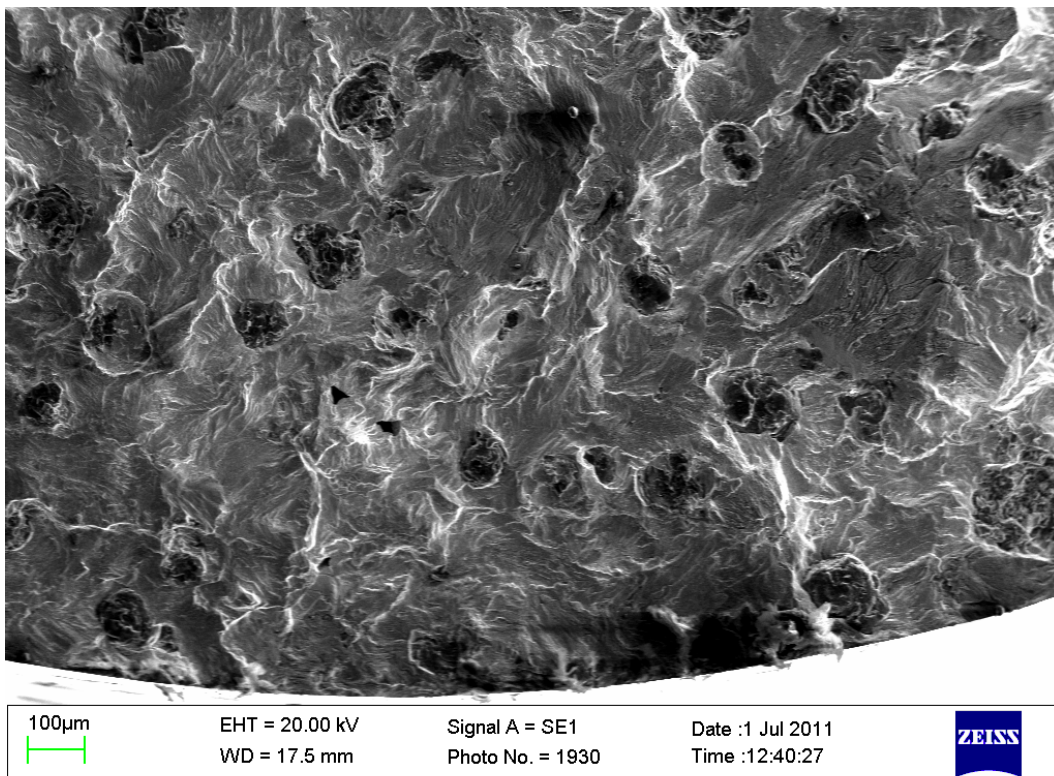
Figure 4.2.1 Shrinkage porosity (Specimen 5)
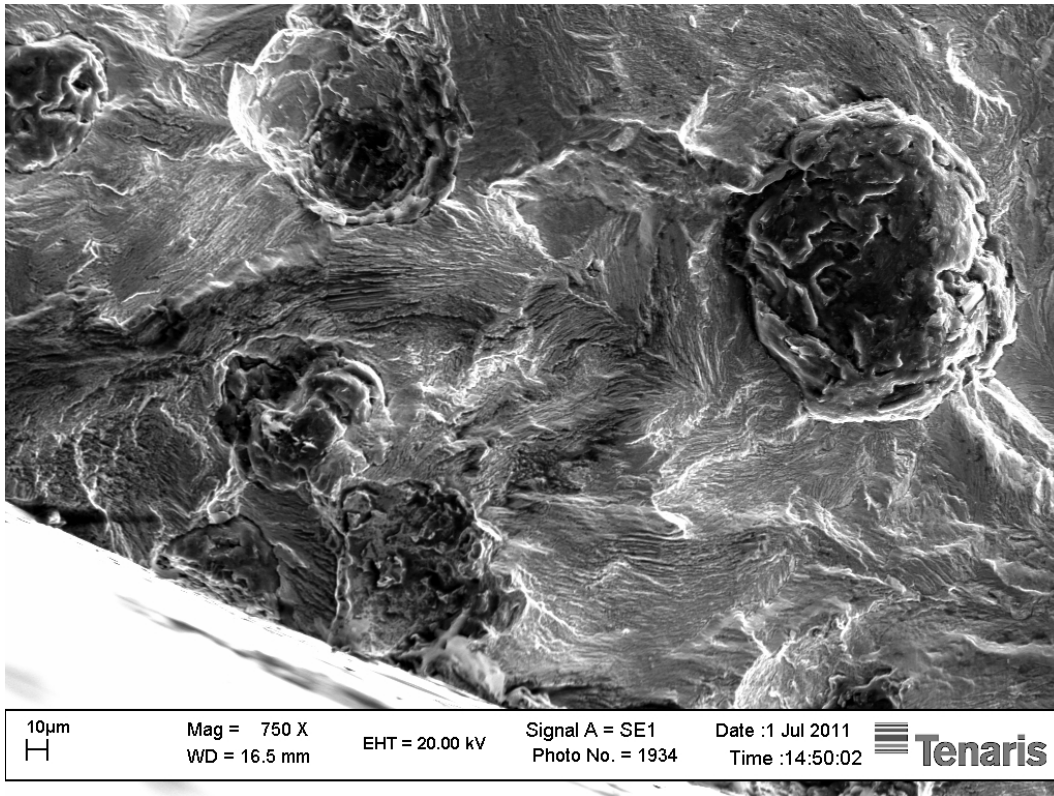

Figure 4.2.2 Fatigue zone (Specimen 4)

Figure 4.2.3 Fatigue zone in detail (Specimen 4)

Specimen #	Area [μm²]	$\sqrt{area}$ [μm]	Result
1	1000000	1000	Failed
2	750000	866	Failed
4	175000	418	Failed
5	1161000	1077	Failed
6	1341000	1158	Failed
7	960000	980	Failed
9	1400000	1183	Failed
10	1350000	1162	Failed
11	6511000	2552	Failed
8	134000	366	Run-out
3	70000	265	Run-out
Average	1350182	1161.973	

Table 4.2.1 Defect dimensions of axial specimens

4.2.2 Fractography of Torsional Test Specimens

Torsional test specimens could not be observed due to their 45° and rolling fracture surfaces but one of the clear photos taken from these specimens is seen in Figure 4.2.4. For this reason their defect dimensions could not be measured.
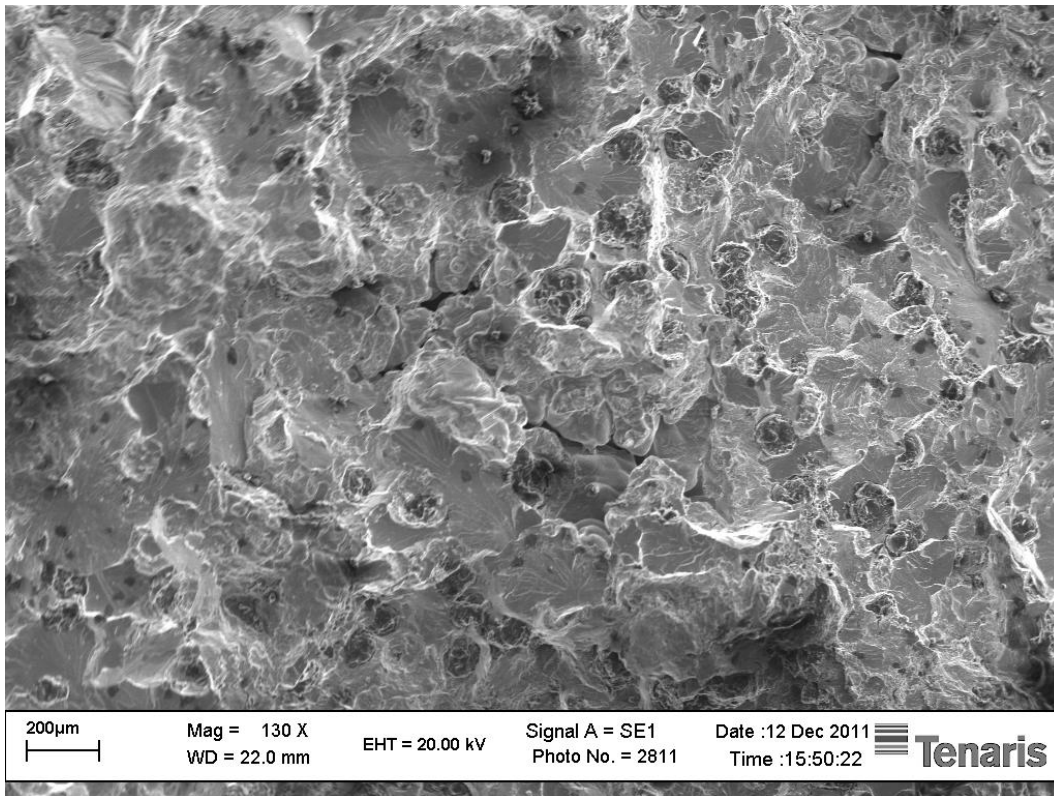

Figure 4.2.4 Shrinkage porosity (Specimen G7)

4.2.3 Fractography of Multiaxial Test Specimens

It is observed that for ductile irons, fatigue crack mostly initiates with the mechanism which is governed by the largest shrinkage porosity in the specimen. These shrinkage porosities behave as stress risers and decrease the stress bearing cross section area of the component. They were observed in different dimensions in all specimens we have, and measured in terms of area by image processing free software "Fiji". Their dimensions are reported in Table 4.2.2.

Specimen #	Area [µm²]	$\sqrt{area}$ [µm]	Result
6.6	1220000	1104.5361	Failed
9.6	320000	565.68542	Failed
10.6	460000	670.82039	Run-out
1.7	1650000	1284.5233	Failed
5.7	572000	768.11457	Failed
6.7	3530000	1878.8294	Failed
8.7	948000	974.67943	Failed
9.7	1845000	1358.3078	Run-out
10.7	1287000	1135.7817	Failed
5.6	7027000	2650.8489	Failed
7.6	840000	916.51514	Run-out
4.7	6510000	2551.4702	Run-out

Table 4.2.2 Defect dimensions of multiaxial specimens

The general characteristic of the external multiaxial fatigue crack path on the surface can be seen in Figure 4.2.5 (photos taken at every 90°).
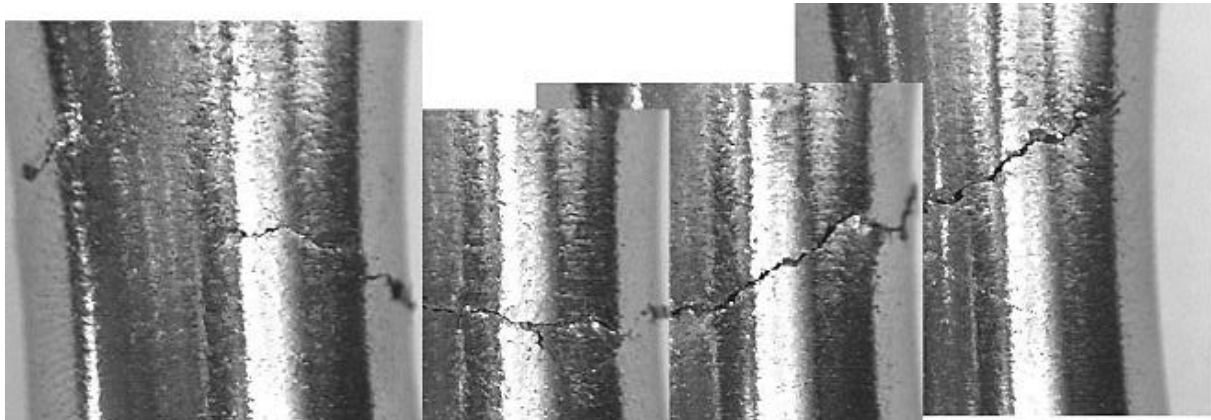

Figure 4.2.5 External crack path (Specimen 3.6)

Figure 4.2.5 is the external crack path of Specimen 3.6 which was left in the testing system until the fracture occurred. This path was observed in the same way for all multiaxial test specimens. This path compared with pure axial and torsional loads:

- Under pure axial stresses the fracture surfaces are flat that are perpendicular to applied load (Figure 4.2.6-a);
- Under pure torsional stresses the fracture surfaces are at 45° (Figure 4.2.6-b).

However, multiaxial fracture surfaces consist of both flat and 45° failure paths as seen in Figure 4.2.6-c.
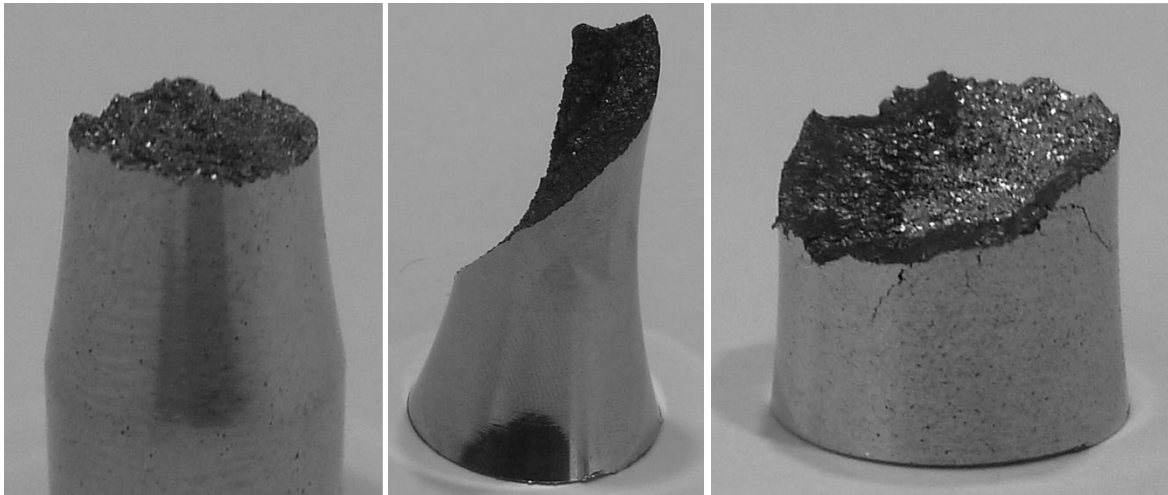
<div align="center">a)   b)   c)</div>

Figure 4.2.6 Fracture surfaces: a) pure axial (Specimen AG7) b) pure torsional (Specimen TG2) c) multiaxial (Specimen 3.6)

4.2.3.1 Specimens Tested at R= -4

4.2.3.1.1   Specimen 3.6

Fracture surface of Specimen 3.6 is seen from top in Figure 4.2.7, fatigue zone almost encircles the fracture surface which was initiated from surface shrinkage porosity that was seen barely from the top view (due to the fact that the position of the imperfection was under the first layers of the fracture surface), but by tilting the specimen as reported in Figure 4.2.8 the observation is clear.
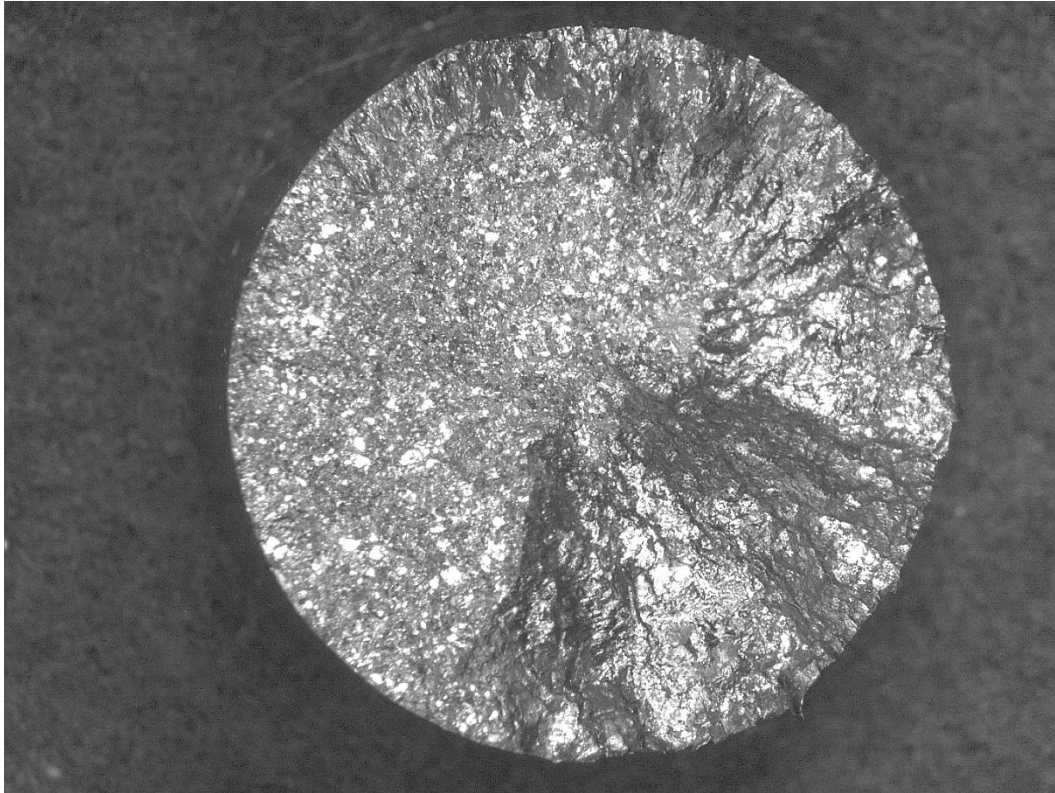
Figure 4.2.7 General photo of the fracture surface (Specimen 3.6)
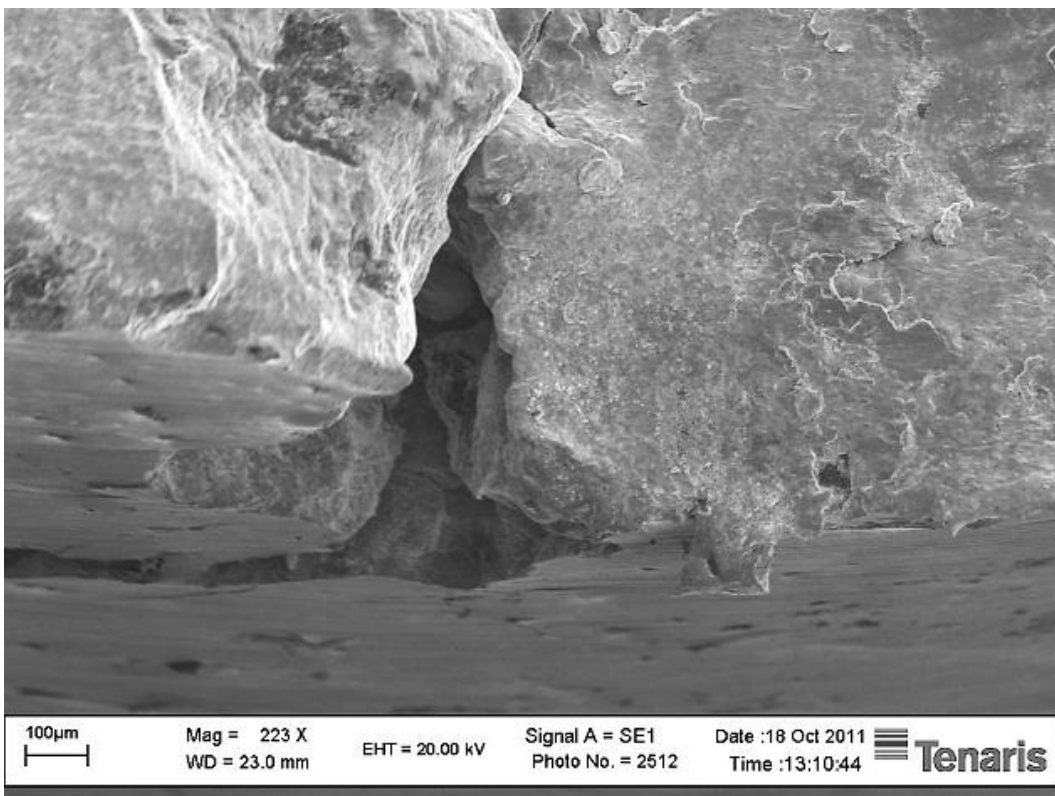

| 100µm | Mag = 223 X | EHT = 20.00 kV | Signal A = SE1 | Date :18 Oct 2011 | Tenaris |
| | WD = 23.0 mm | | Photo No. = 2512 | Time :13:10:44 | |

Figure 4.2.8 Nucleation point of the fatigue crack (Specimen 3.6)

In detail, as seen in Figure 4.2.9, there are smooth areas on fracture surface that are in the fatigue zone. These are due to the high friction and rubbing between surfaces during the test (as mentioned in Section 2.1.2.2 combination of compressive and torsional stresses give rise to friction and rubbing).
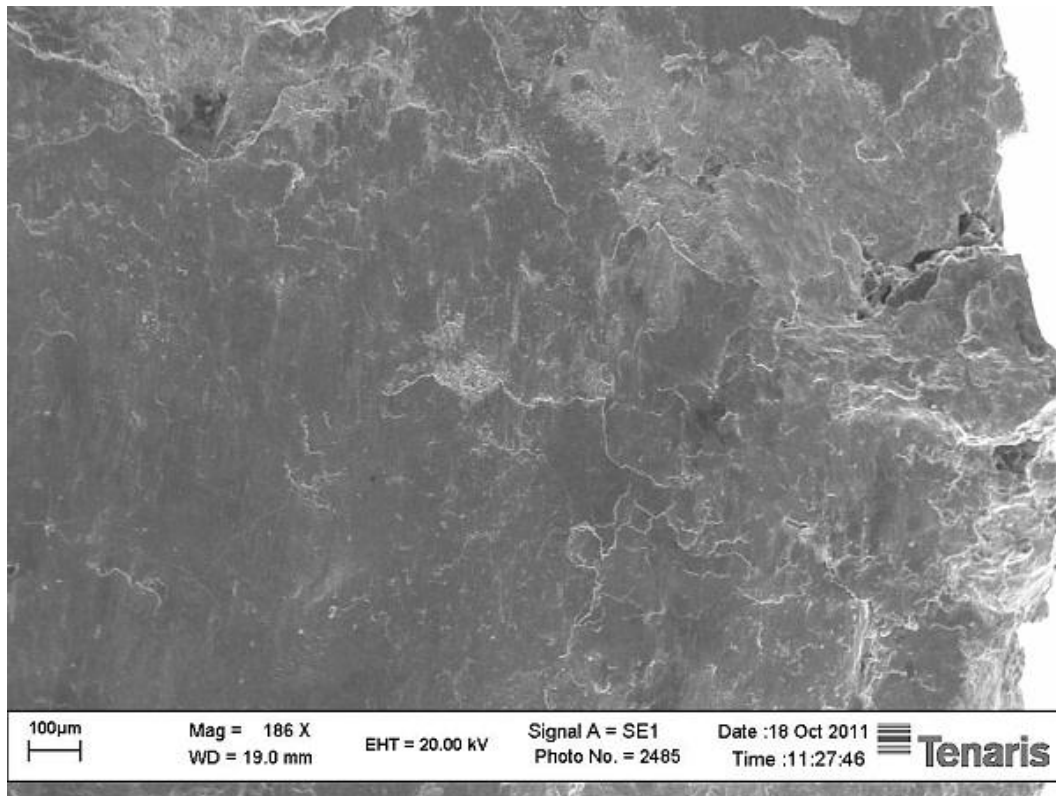
Figure 4.2.9 Fracture surface (Specimen 3.6)

Moreover, in the fatigue zone, graphite nodules cannot be seen. Likely, combination of compressive stresses and torsional stresses on ductile iron give rise to fracture of graphite nodules and their remaining particles are covered with matrix due to the plastic deformation in the fatigue zone; on the other hand, brittle zone is different due to the lack of plastic deformation (both zones are in Figure 4.2.10).
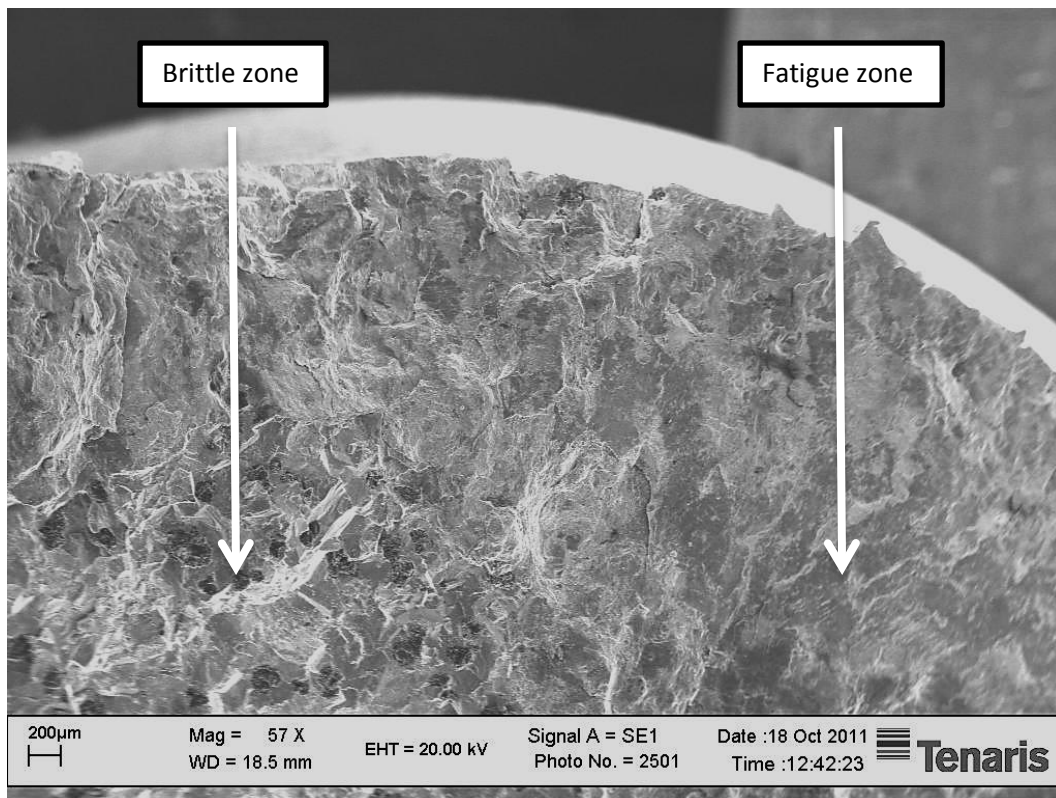
Figure 4.2.10 Transition area: fatigue and brittle zones (Specimen 3.6)

4.2.3.1.2   Specimen 4.6

Unlike others, specimen 4.6 (Figure 4.2.11) does not exhibit dangerous shrinkage porosity on the fracture surface. However, it is seen that SF1 could not resist these stresses ($\sigma_{amp} = 250\ MPa, \sigma_{mean} = -250\ MPa, \tau_{amp} = 125\ MPa$). Consequently, it is understood that equivalent stress of these stresses is higher that the material's multiaxial fatigue limit.
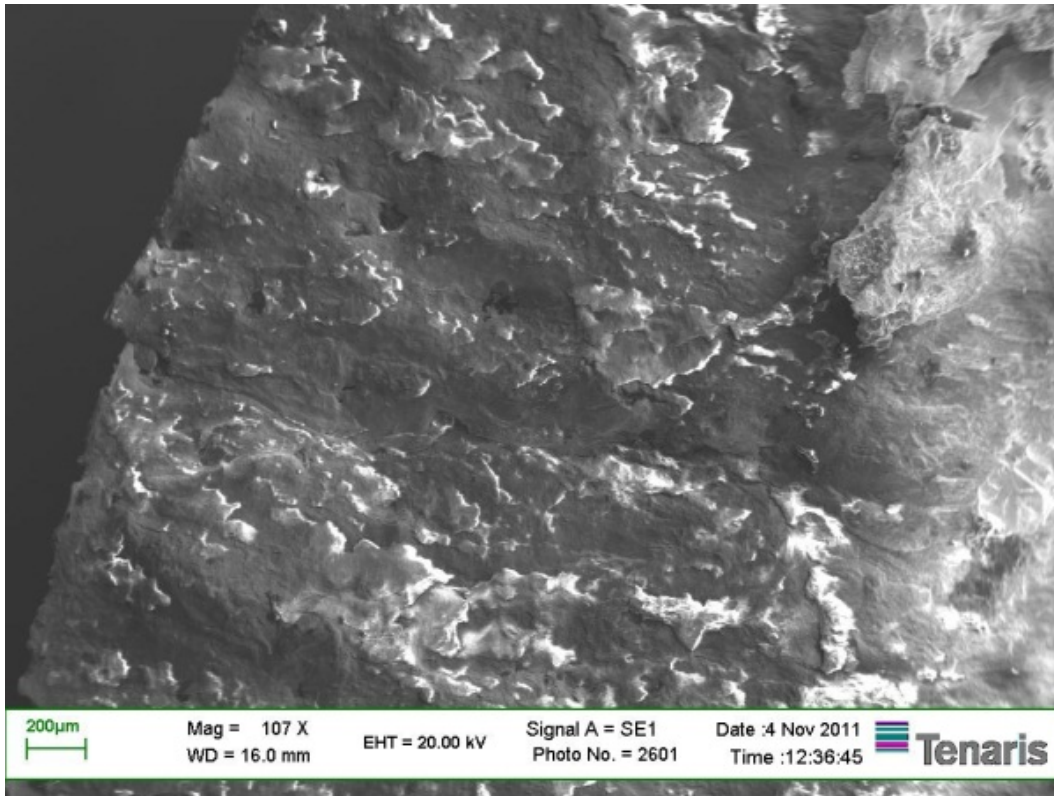
Figure 4.2.11 Fatigue zone (Specimen 4.6)

4.2.3.1.3 Specimen 5.6

Specimen 5.6 has very large shrinkage porosity (Figure 4.2.12) next to the surface and one more in the center of the fracture surface (Figure 4.2.13). These porosities, in particular, the large one decrease the multiaxial fatigue limit.
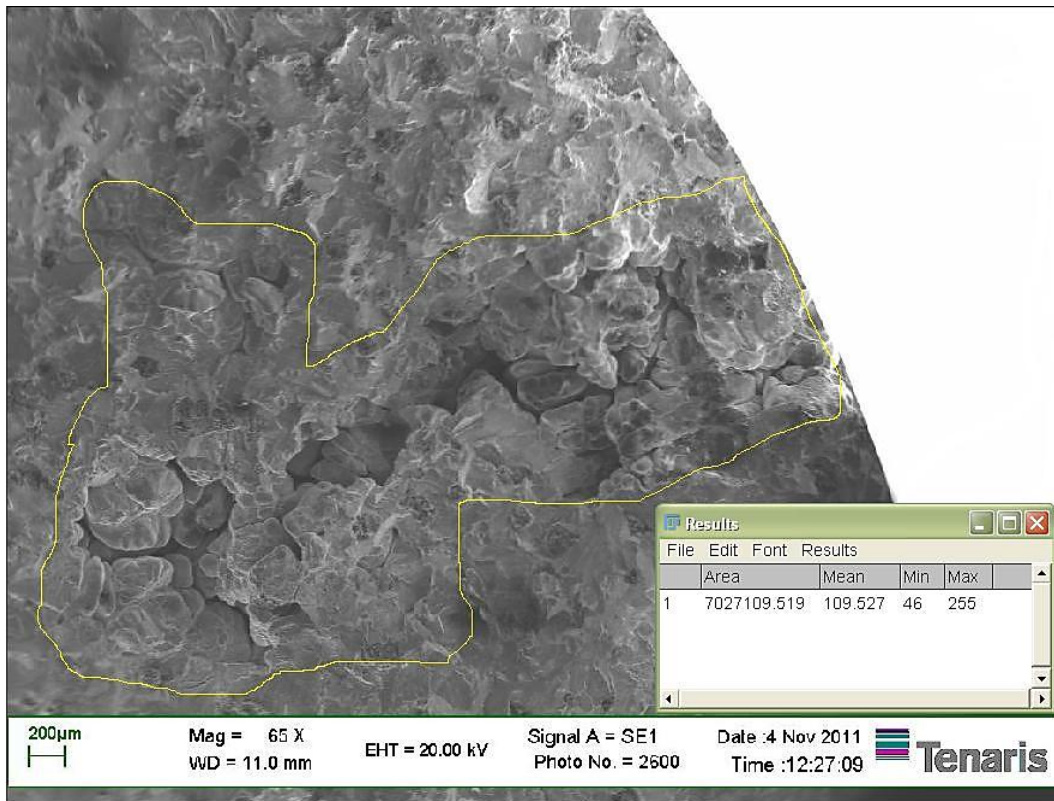
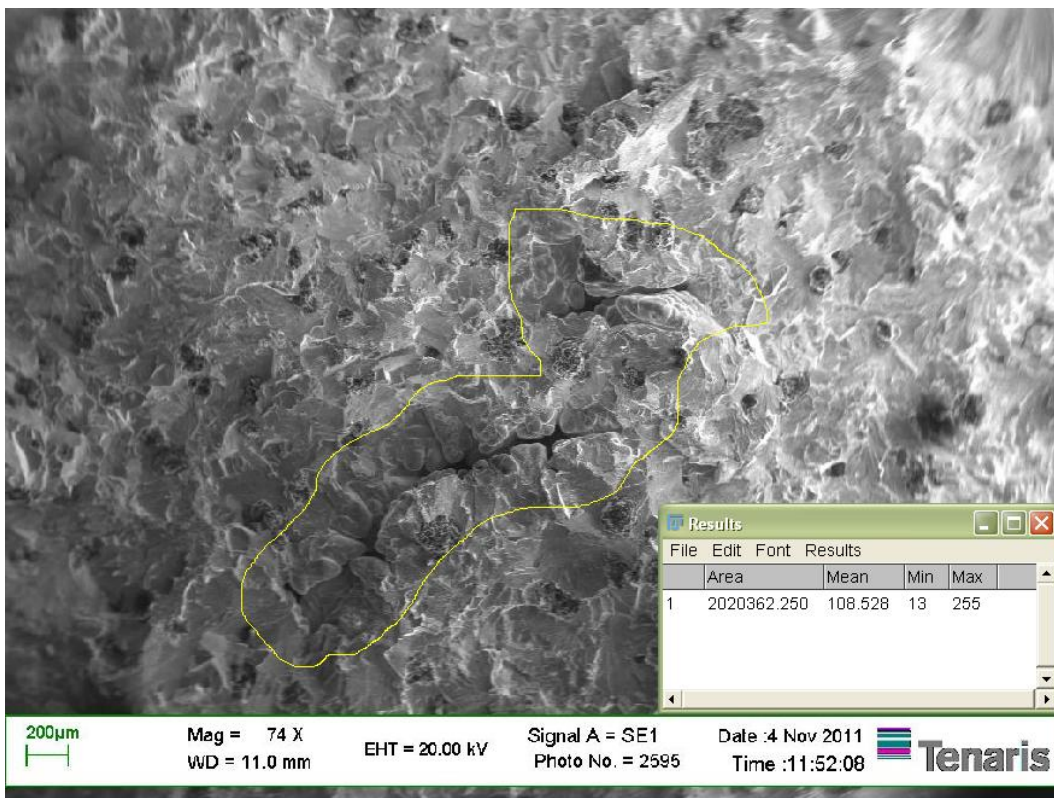**Figure 4.2.12 Shrinkage porosity next to the surface and its area [μm^2] (Specimen 5.6)**

Figure 4.2.13 Shrinkage porosity in the center and its area [μm^2] (Specimen 5.6)

4.2.3.1.4   Specimen 6.6

In the general case, fatigue cracks nucleate at the surface; however for defective materials like ductile iron, it might be different. Due to the presence of the shrinkage porosity, it behaved as a stress riser and fatigue crack nucleated then crack propagated towards surface (Figure 4.2.14).
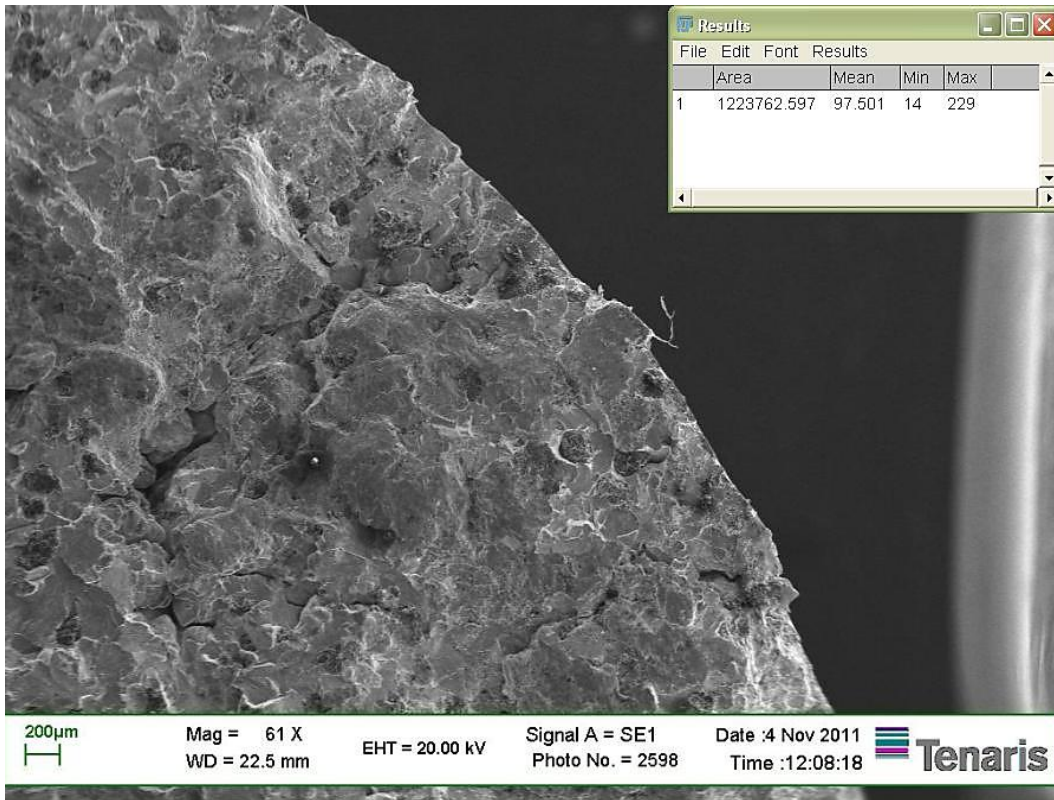
Figure 4.2.14 Fatigue zone and shrinkage porosity with area [μm^2] (Specimen 6.6)

4.2.3.1.5   Specimen 7.6

Specimen 7.6 is a run-out specimen and its observation by SEM showed that it does not have a large shrinkage porosity. The only one (Figure 4.2.15) is in the center of the specimen, it is not a dangerous site due to its position.
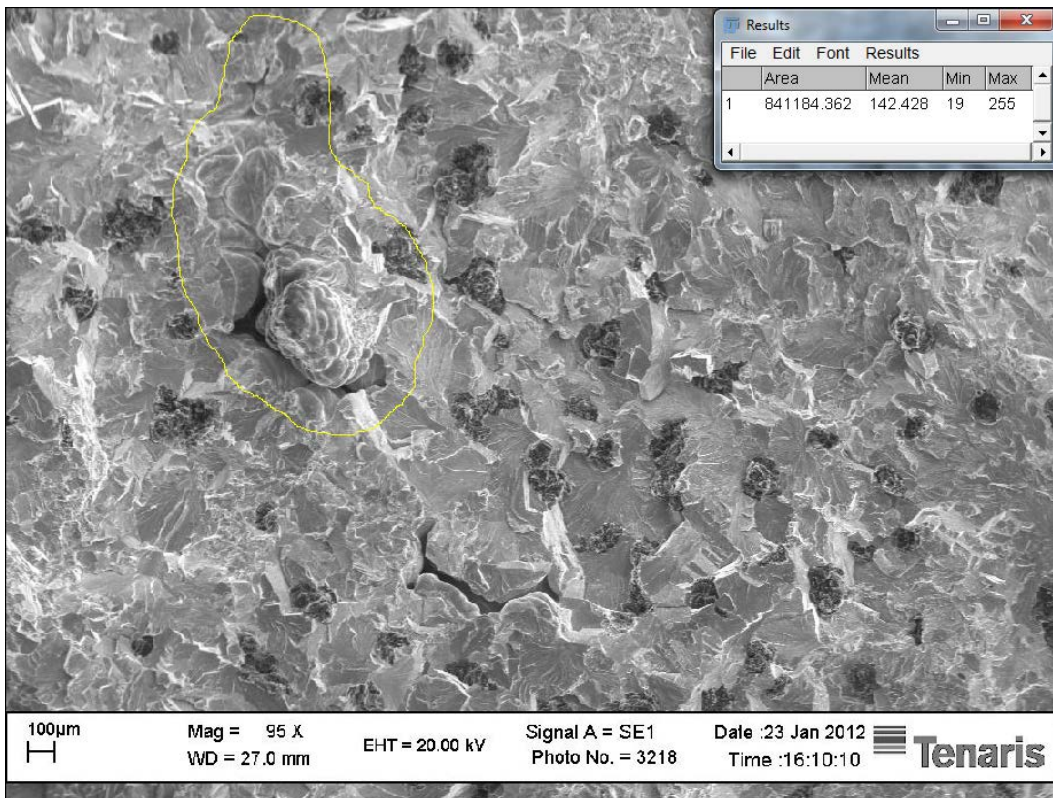
Figure 4.2.15 Shrinkage porosity with area [μm^2] (Specimen 7.6)

4.2.3.1.6   Specimen 9.6

As for specimen 6.6, also for specimen 9.6 crack probably nucleated at the shrinkage porosity and propagated to surface (see Figure 4.2.16, with the other fracture surface details shown in Figure 4.2.17 and Figure 4.2.18).

Figure 4.2.16 Shrinkage porosity with area [µm^2] and fatigue zone (Specimen 9.6)

Figure 4.2.17 Specimen 9.6 has multiple numbers of shrinkage porosities (shown with arrows) on the fracture surface

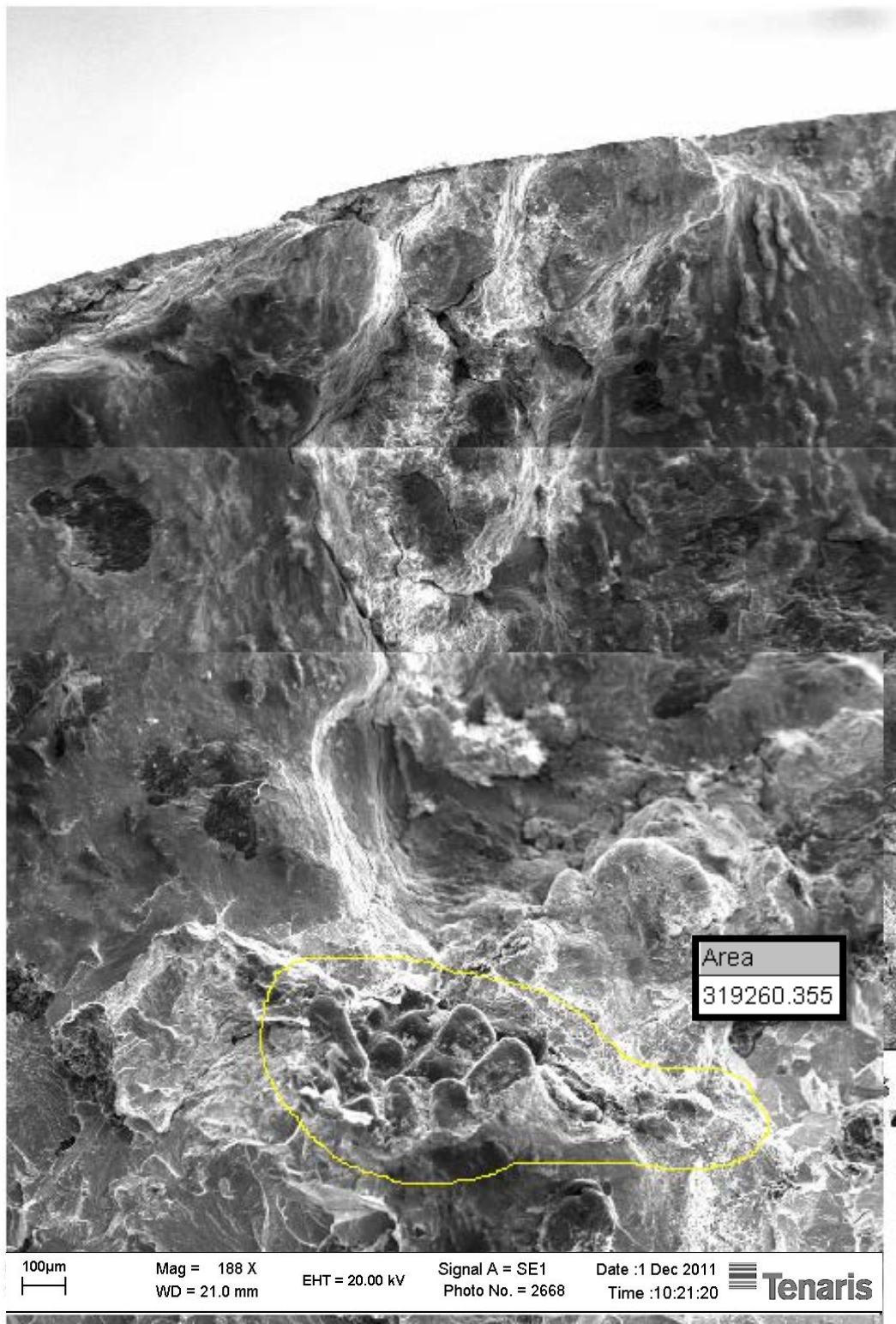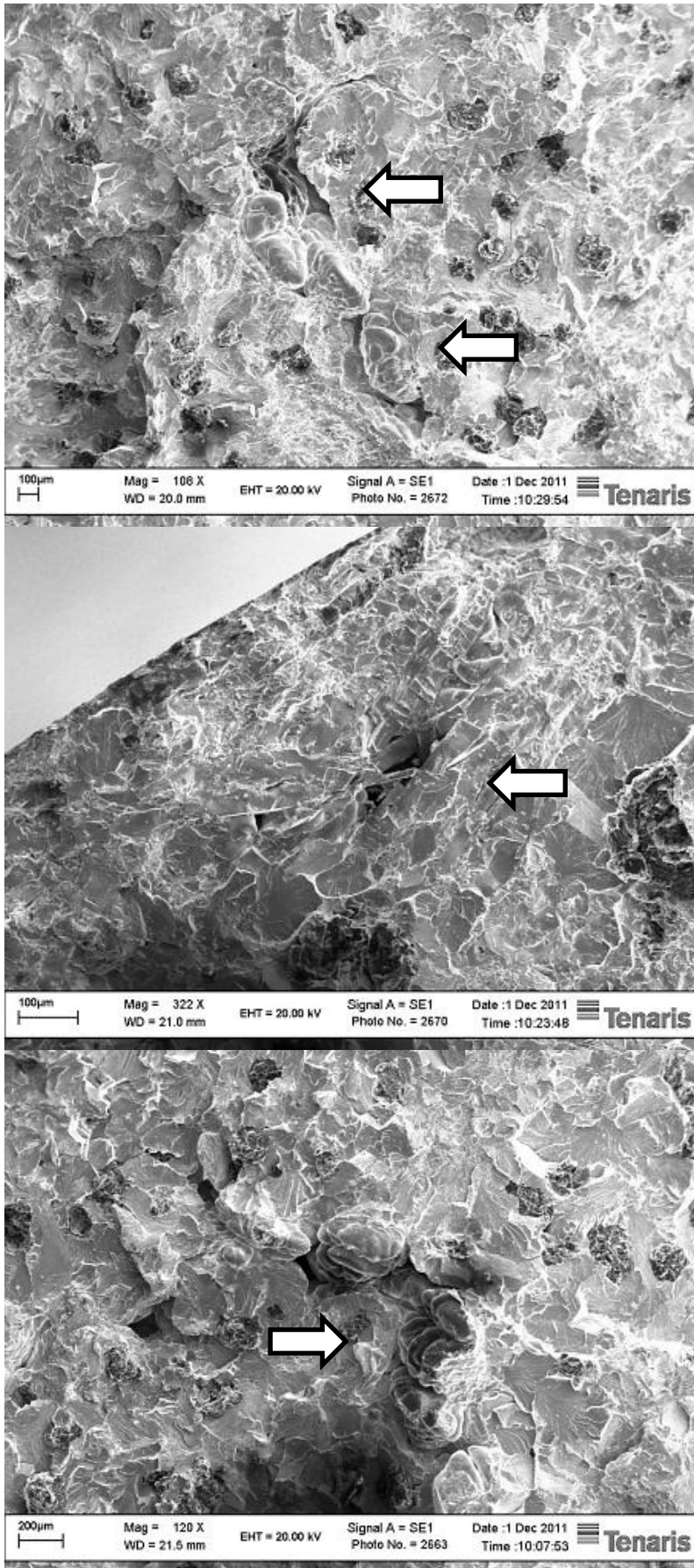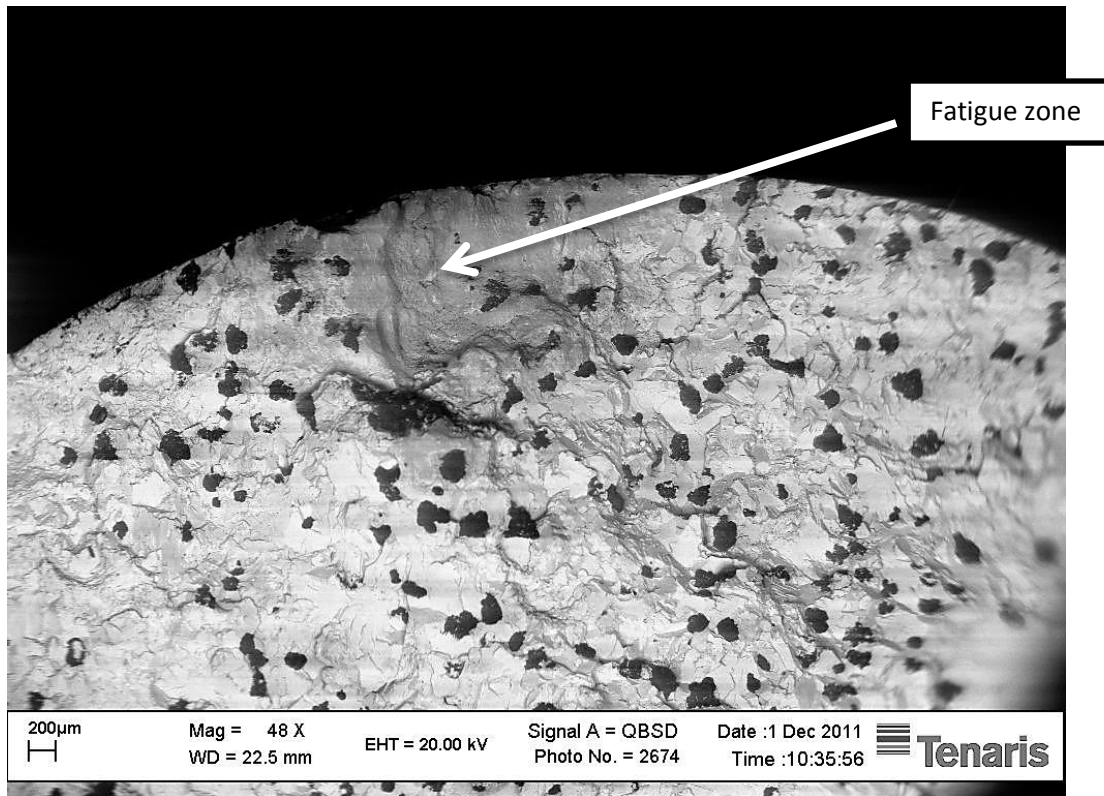**Figure 4.2.18 Fatigue zone (taken at QBSE mode) (Specimen 9.6)**

4.2.3.1.7 Specimen 10.6

Specimen 10.6 is a run-out specimen however it was broken after test in order to see if there is a presence of a manufacturing imperfection from which fatigue crack can nucleate. It can be seen in Figure 4.2.19 that fatigue has not initiated although the specimen has porosities and some of them are close to surface. The measurements performed on these imperfections shows that the areas were lower than the ones found on the failed specimens. Therefore, its equivalent stress is lower than the multiaxial fatigue limit calculated with method of Hodge-Rosenblatt (see Section 4.1.1).

Figure 4.2.19 Three of the shrinkage porosities (shown with arrows) and their areas [μm²] (Specimen 10.6)

4.2.3.1.8 Specimen 1.7

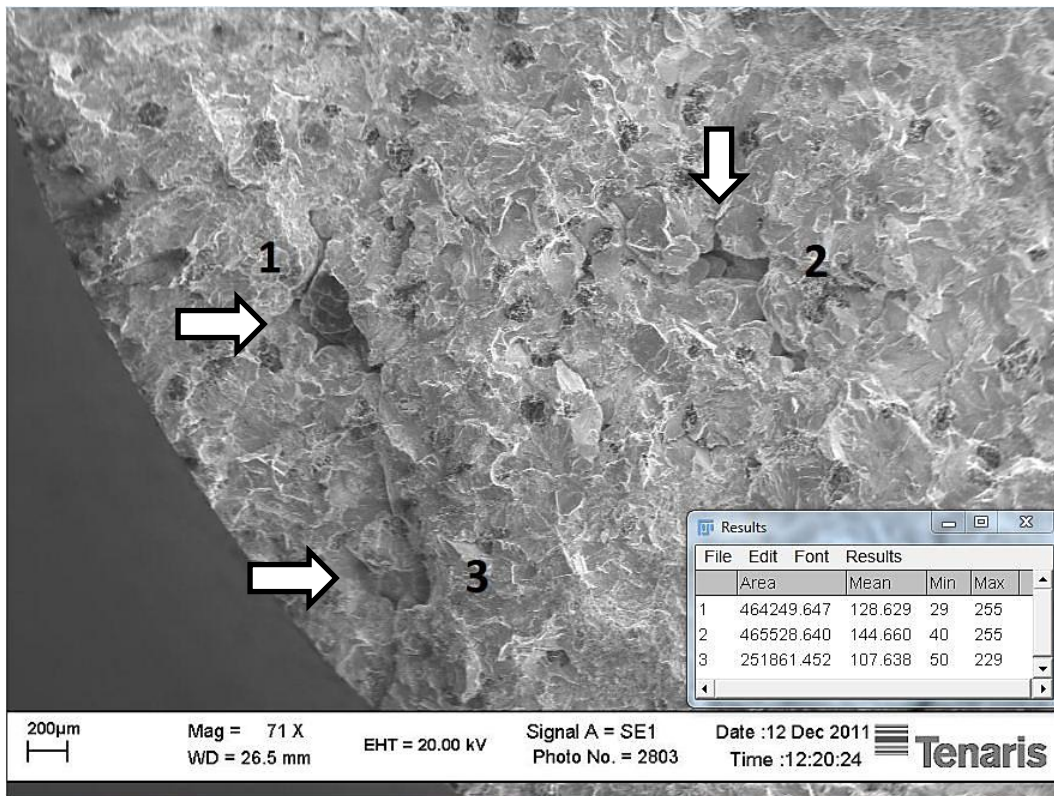Fatigue zone of Specimen 1.7 is seen in Figure 4.2.20 and Figure 4.2.21 which are taken at the same magnification at quantitative back scattered electron (QBSE) and secondary electron (SE) modes, respectively. The QBSE method was used in order to clearly underline the presence of the fatigue region, it can be observed that is characterized by a darker color in Figure 4.2.20 (black circular constituents are graphite nodules).

Fatigue initiated from a large porosity near the center that propagates to the surface (Figure 4.2.21). Moreover, the specimen contains a second shrinkage porosity positioned close to the surface (Figure 4.2.22) with lower dimensions: $0.57 * 10^6 \mu m^2$, 65% smaller than the large one ($1.65 * 10^6 \mu m^2$).

Figure 4.2.20 Fatigue zone (taken at QBSE mode) (Specimen 1.7)
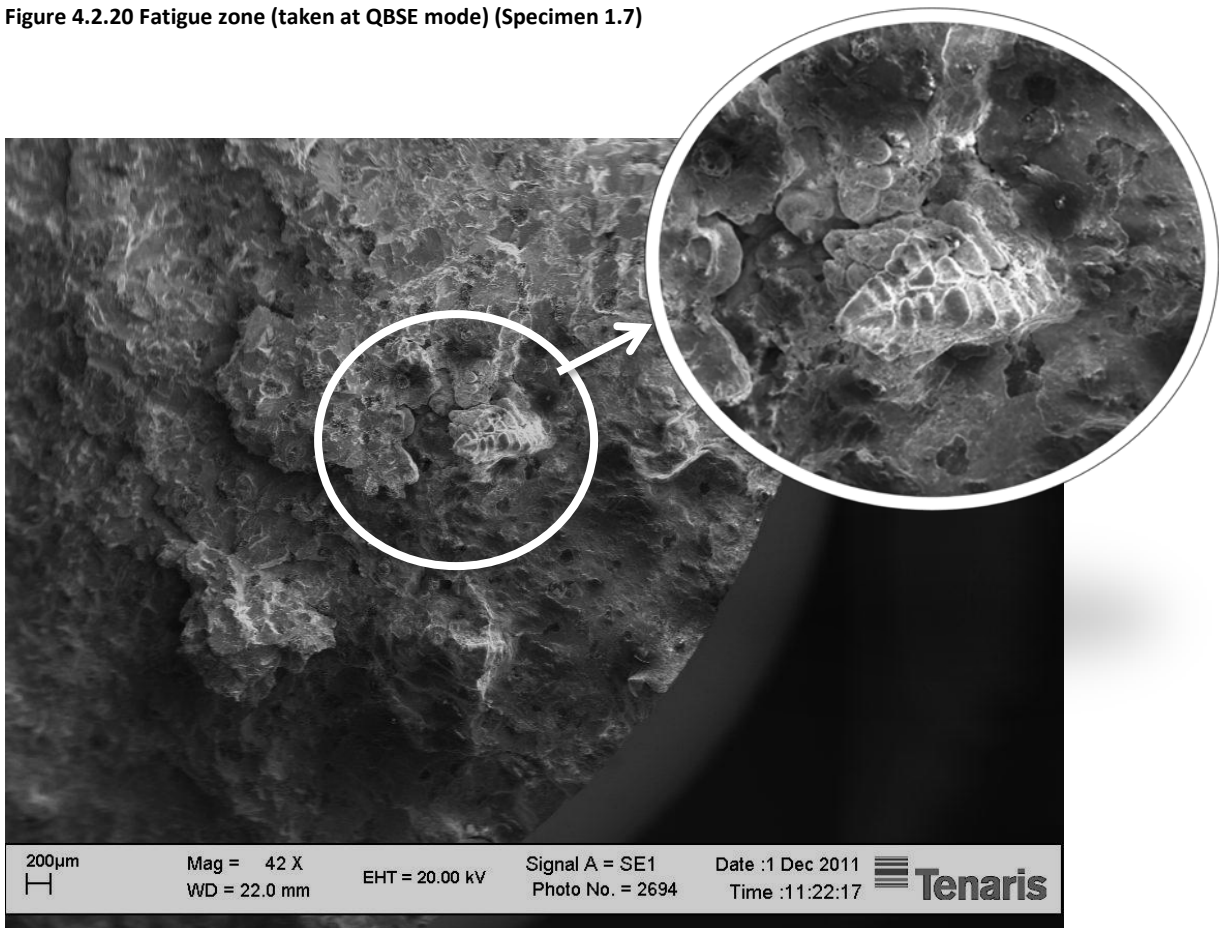
Figure 4.2.21 Fatigue zone and dendritic morphology of shrinkage porosity with an attached detailed image (Specimen 1.7)
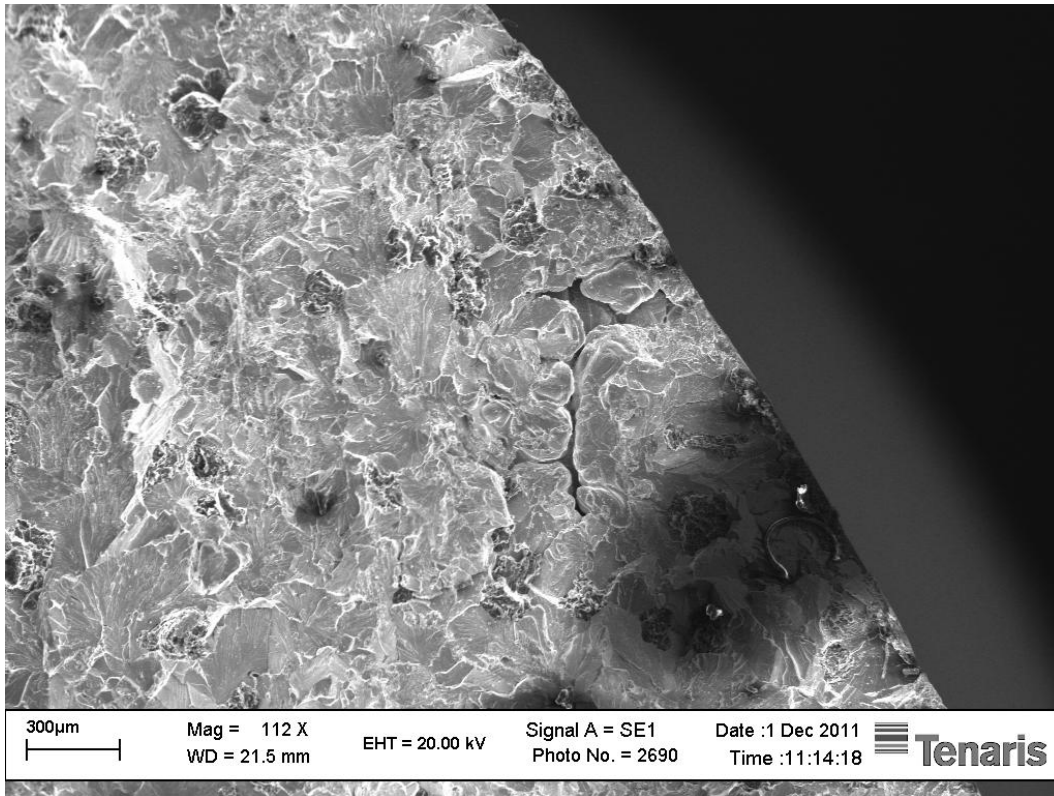
Figure 4.2.22 Shrinkage porosity next to the surface (Specimen 1.7)

Moreover, specimen 1.7's counter piece's fracture (Figure 4.2.23) surface was also observed by SEM. It was seen that clearly the large shrinkage porosity governs the fatigue and its area was calculated.
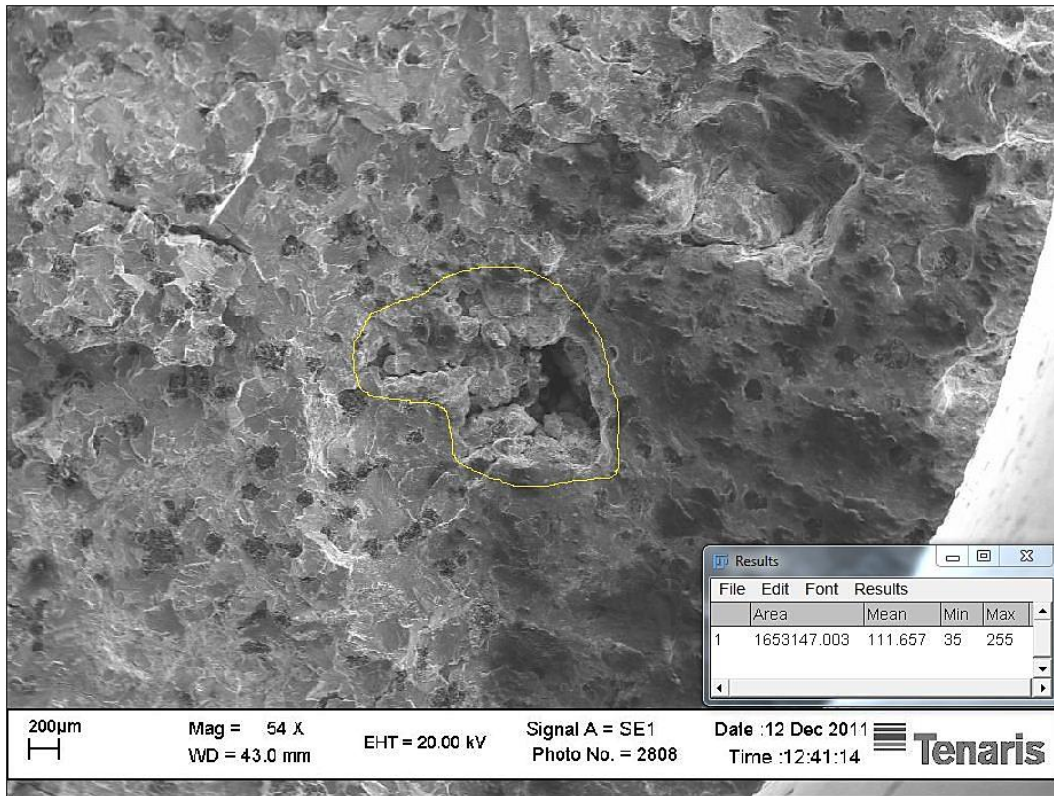
Figure 4.2.23 Shrinkage porosity with area [μm^2] (Specimen 1.7 – Counter piece)

During the experiments a lot of rust points were formed (also observed visually) on the stress bearing part of the specimens due to the oxidation of micro cracks on the surface. These cracks are non-propagating cracks; one of them is seen in Figure 4.2.24. The number of these rust points has increased while approaching to the fatigue crack nucleation point and failure moment for each specimen.
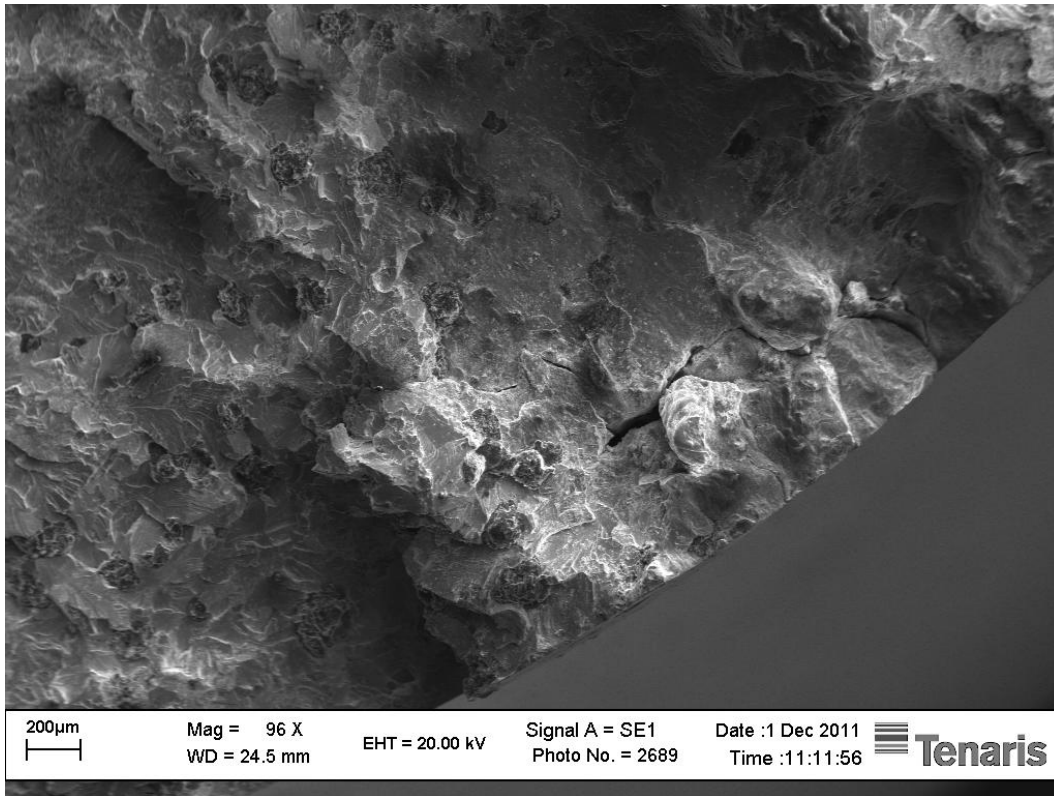
Figure 4.2.24 Non-propagating crack (Specimen 1.7)

4.2.3.2 Specimens Tested at R= -3

4.2.3.2.1   Specimen 3.7

No dangerous shrinkage porosities were observed for this specimen via SEM due to the high plastic deformation in the fatigue zone. Its fatigue region via SE and QBSE modes is shown in Figure 4.2.25 and Figure 4.2.26, respectively.
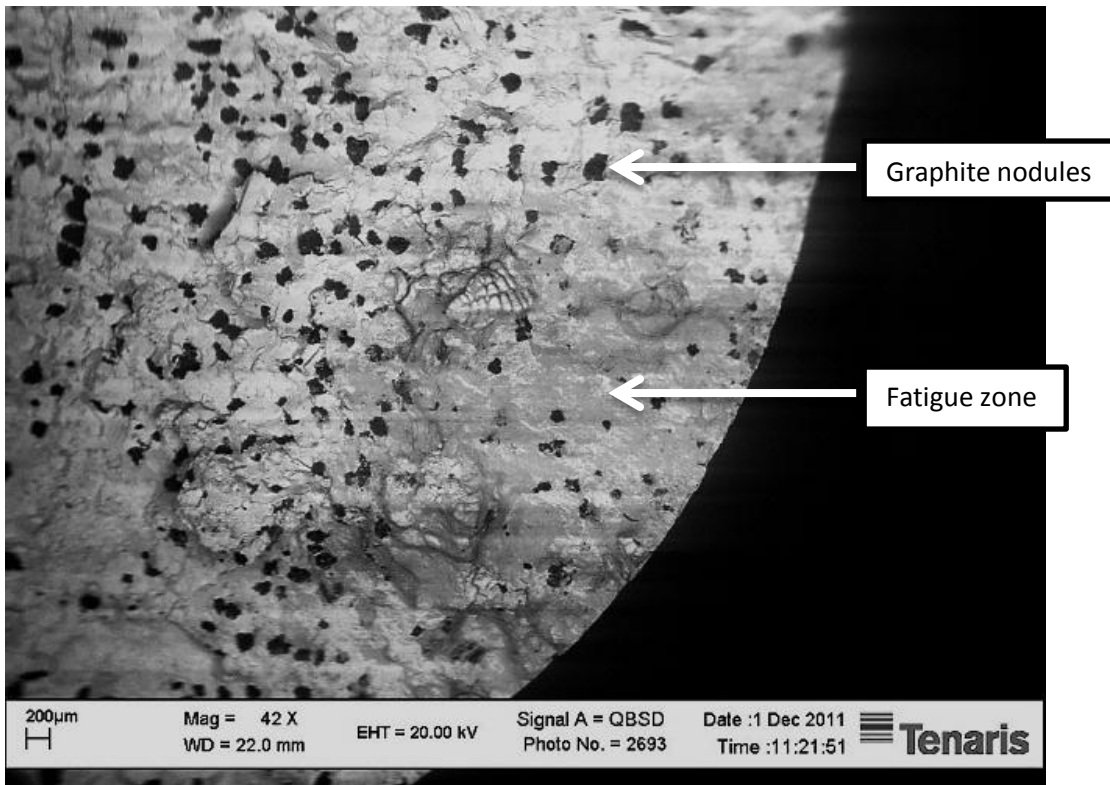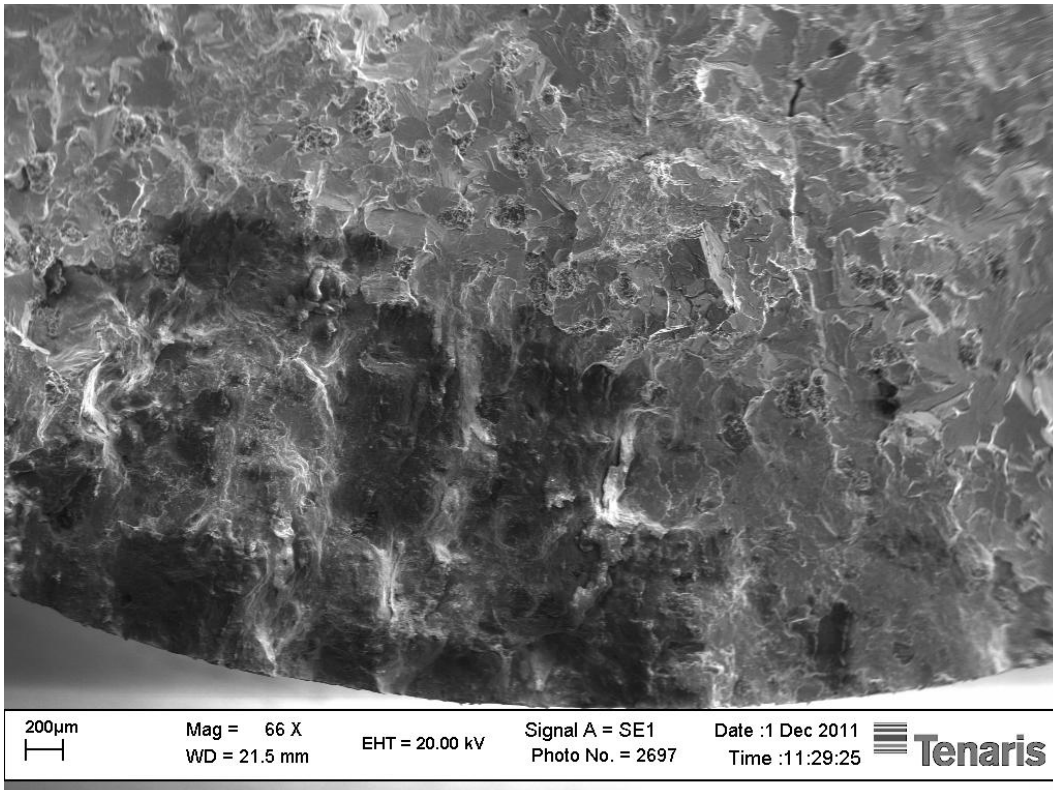
Figure 4.2.25 Fatigue zone (Specimen 3.7)
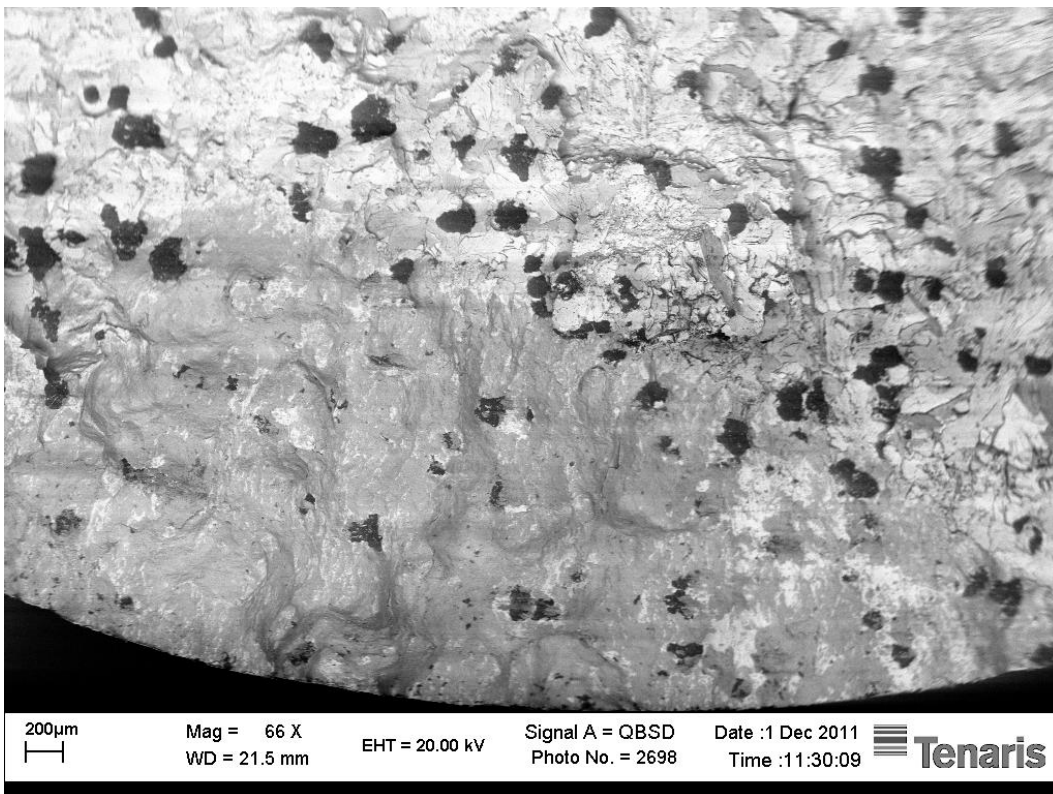
Figure 4.2.26 Fatigue zone (taken at QBSE mode) (Specimen 3.7)

### 4.2.3.2.2 Specimen 6.7

Fatigue zone and shrinkage porosity with its dimensions are shown in Figure 4.2.27.
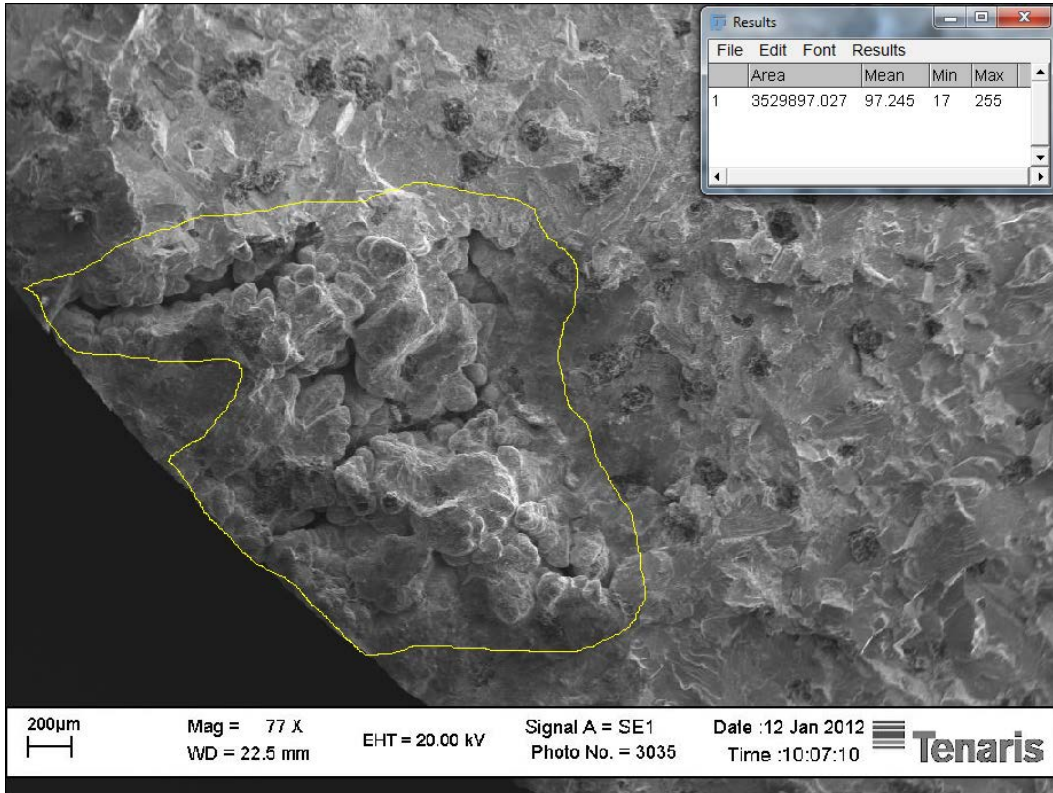
Figure 4.2.27 Fatigue zone and shrinkage porosity and its area [μm^2] (Specimen 6.7)

4.2.3.2.3 Specimen 5.7

General fatigue region (Figure 4.2.28) and shrinkage porosity with its dimensions (Figure 4.2.29) are shown below.
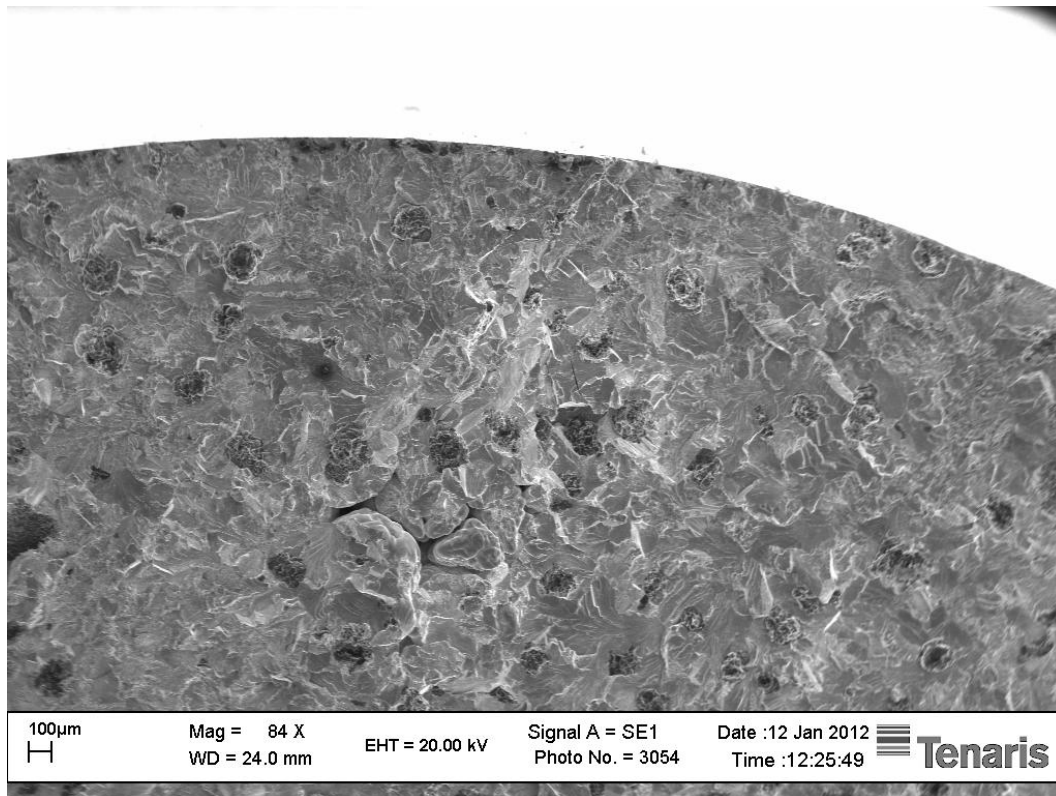
Figure 4.2.28 Fatigue zone and shrinkage porosity (Specimen 5.7)
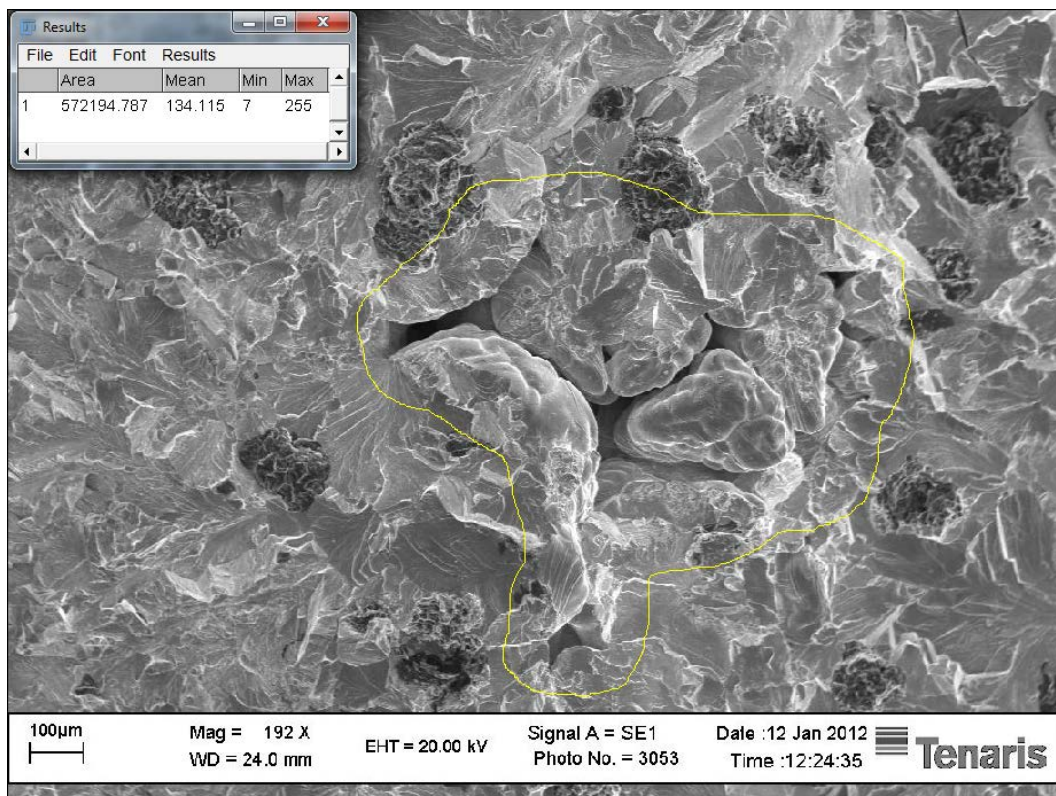
Figure 4.2.29 Shrinkage porosity and its area [μm^2] (Specimen 5.7)

4.2.3.2.4   Specimen 8.7

On the fracture surface there are 4 crucial shrinkage porosities; number 1 initiated the fatigue (Figure 4.2.31), number 2 is nearby the fatigue zone (Figure 4.2.32), number 3 is in the center (Figure 4.2.33) and number 4 is near to surface (Figure 4.2.34) but at the other side of the specimen. With respect to their positions and areas, it can be commented that shrinkage porosities number 1 and number 2 act as one porosity due to their positions (which are shown by arrows in Figure 4.2.30) and initiated the fatigue together. Because porosity number 4 is larger than number 1, under normal conditions it should have initiated the fatigue.
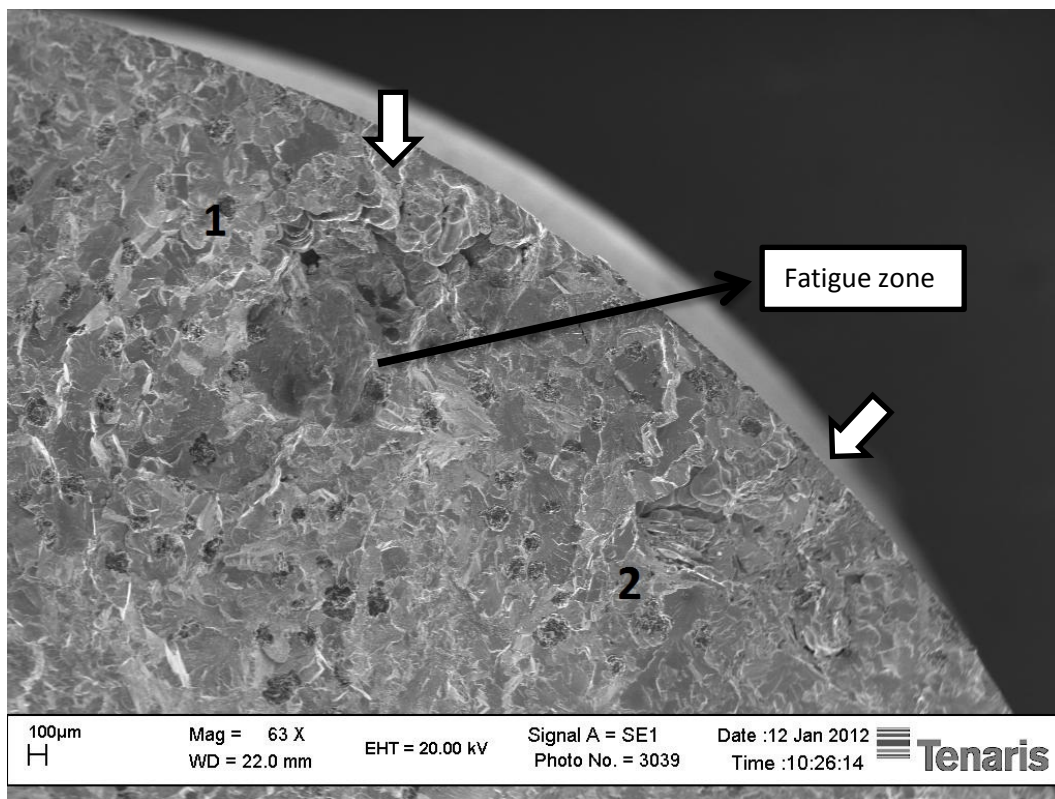
Figure 4.2.30 Shrinkage porosities: number 1 and 2 (shown with arrows) (Specimen 8.7)
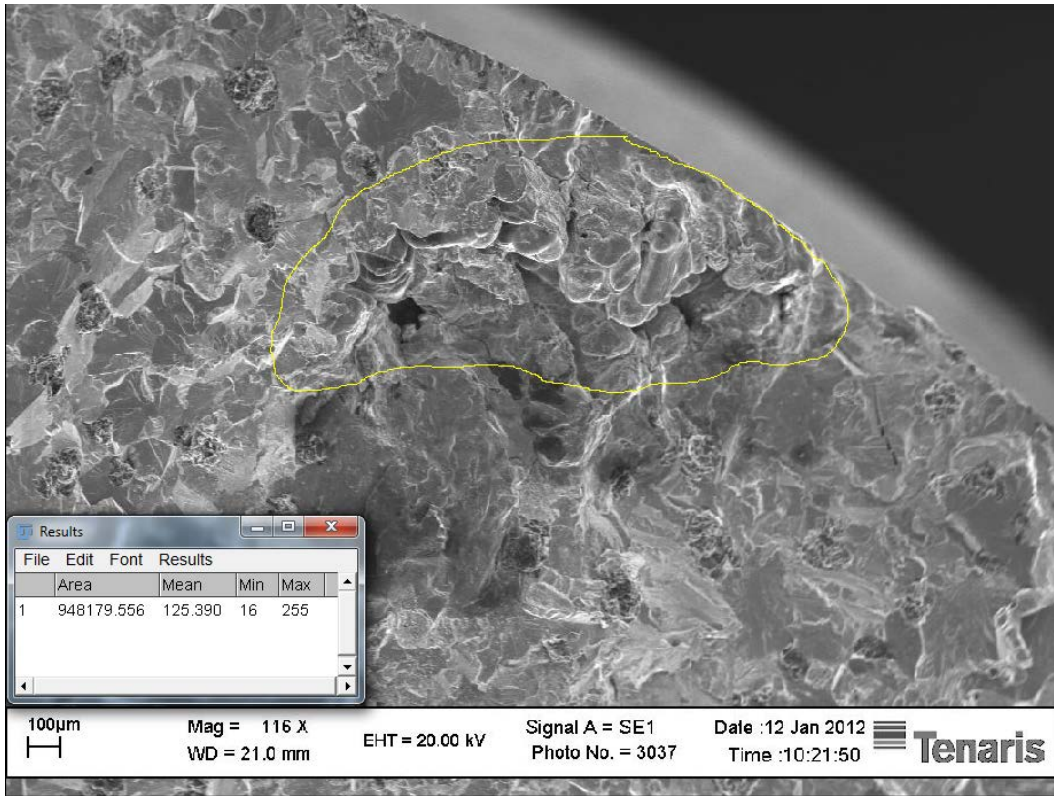
Figure 4.2.31 Shrinkage porosity number 1 and its area [μm^2] (Specimen 8.7)
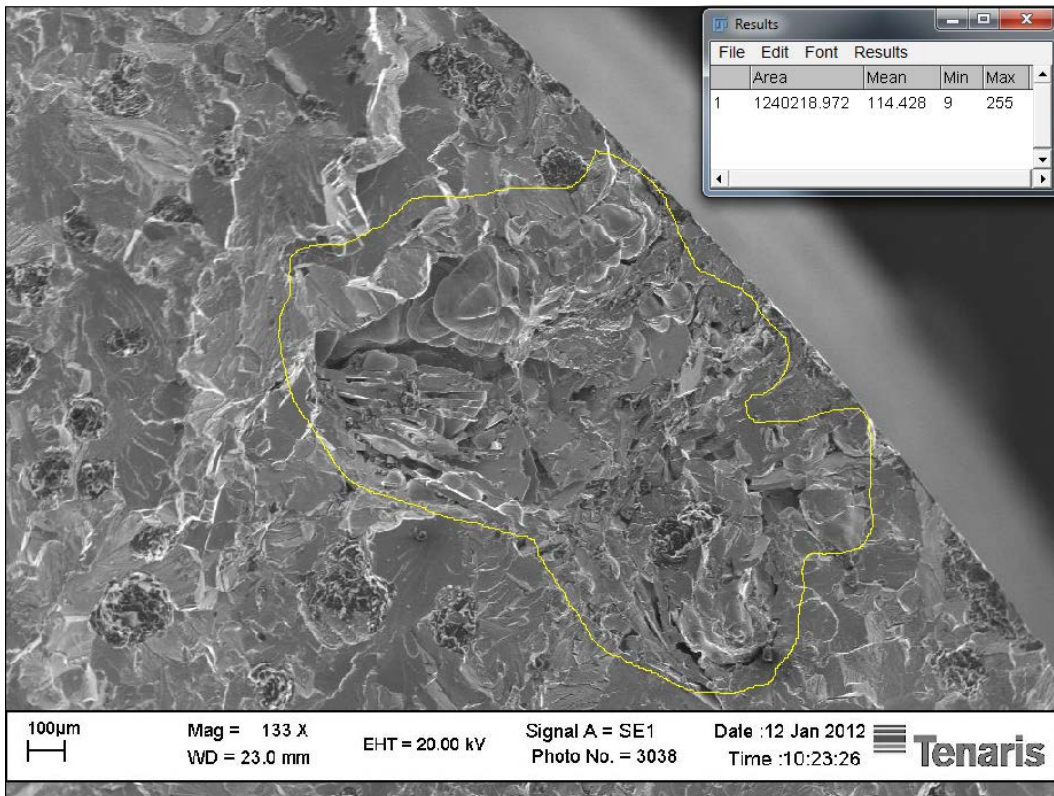
Figure 4.2.32 Shrinkage porosity number 2 and its area [μm^2] (Specimen 8.7)
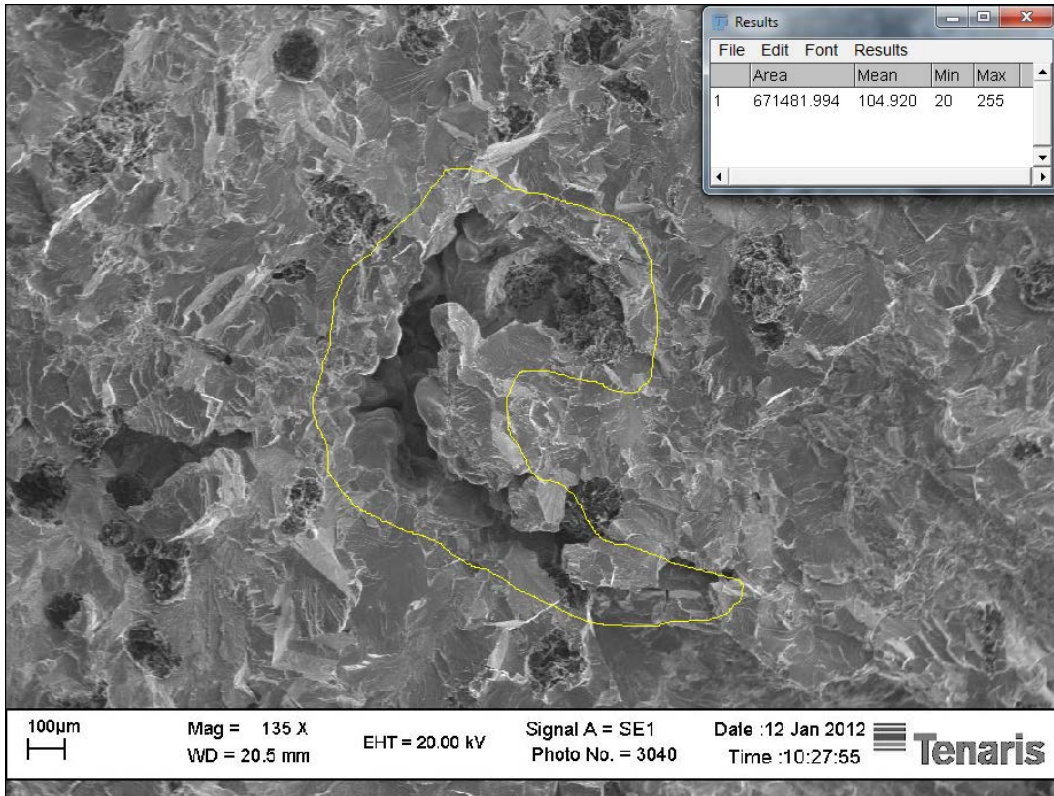
Figure 4.2.33 Shrinkage porosity number 3 and its area [µm^2] (Specimen 8.7)
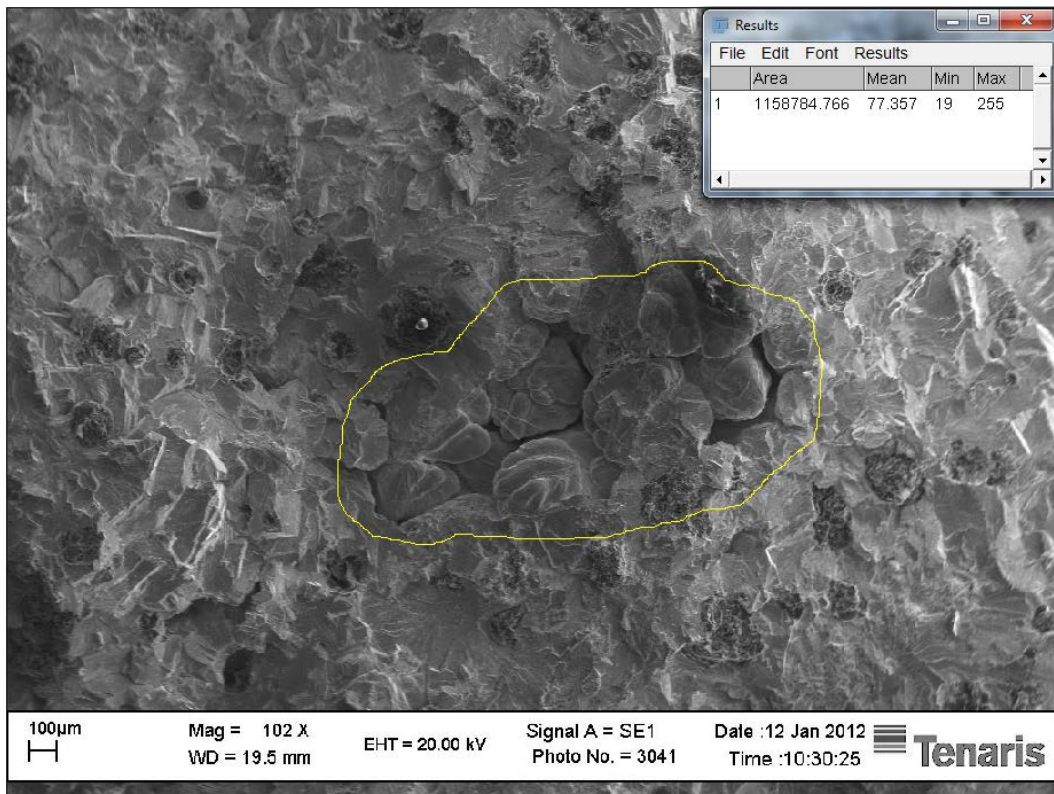
Figure 4.2.34 Shrinkage porosity number 4 and its area [µm^2] (Specimen 8.7)

4.2.3.2.5   Specimen 10.7

Specimen 10.7 has multiple numbers of shrinkage porosities on the fracture surface and most of them are nearby the fatigue region but one of them governs the failure of the specimen which is the number 3 in Figure 4.2.35 and the largest one in the specimen.
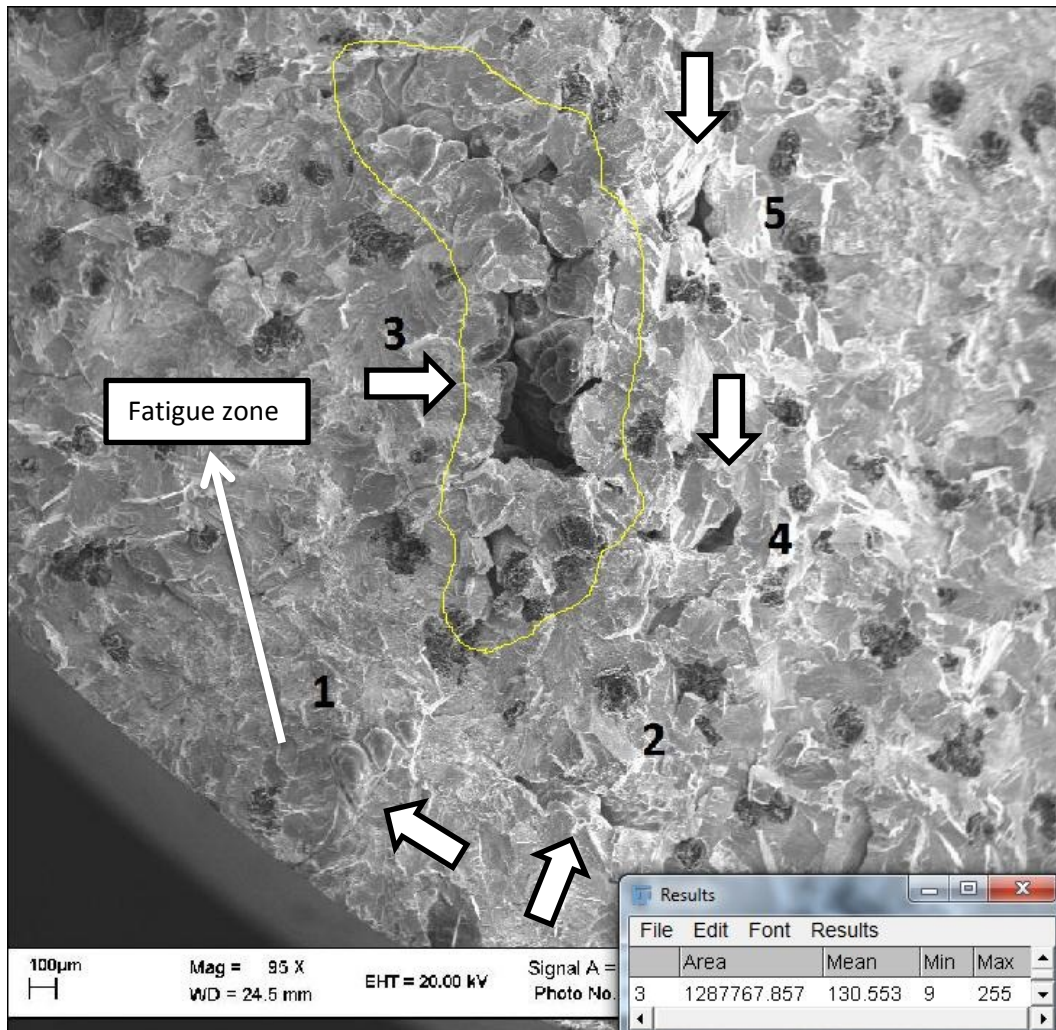
Figure 4.2.35 Shrinkage porosities (shown with arrows) and the area of porosity number 3 [μm^2] (Specimen 10.7)

4.2.3.2.6 Specimen 9.7

Specimen 9.7 is a run-out specimen and its shrinkage porosity with dimensions is shown in Figure 4.2.36.
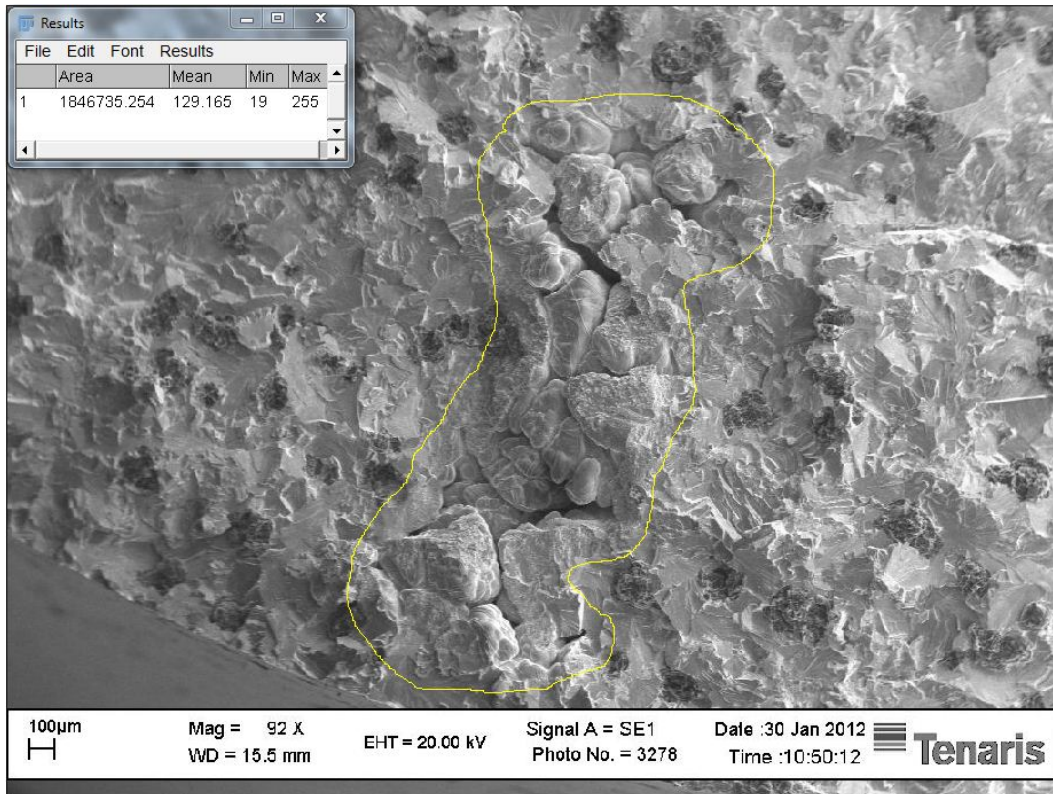
Figure 4.2.36 Shrinkage porosity and its area [µm^2] (Specimen 9.7)

4.3 Microstructural Characterization

Microstructure is one of the most important parameters of ductile iron besides composition, graphite nodule and shrinkage porosity shape, size, and distribution. It affects directly hardness, yield strength, tensile strength, fatigue resistance, and many other mechanical properties of the ductile iron.

SF1 has a fully pearlitic matrix as shown in Figure 4.3.1 taken by optical microscope.
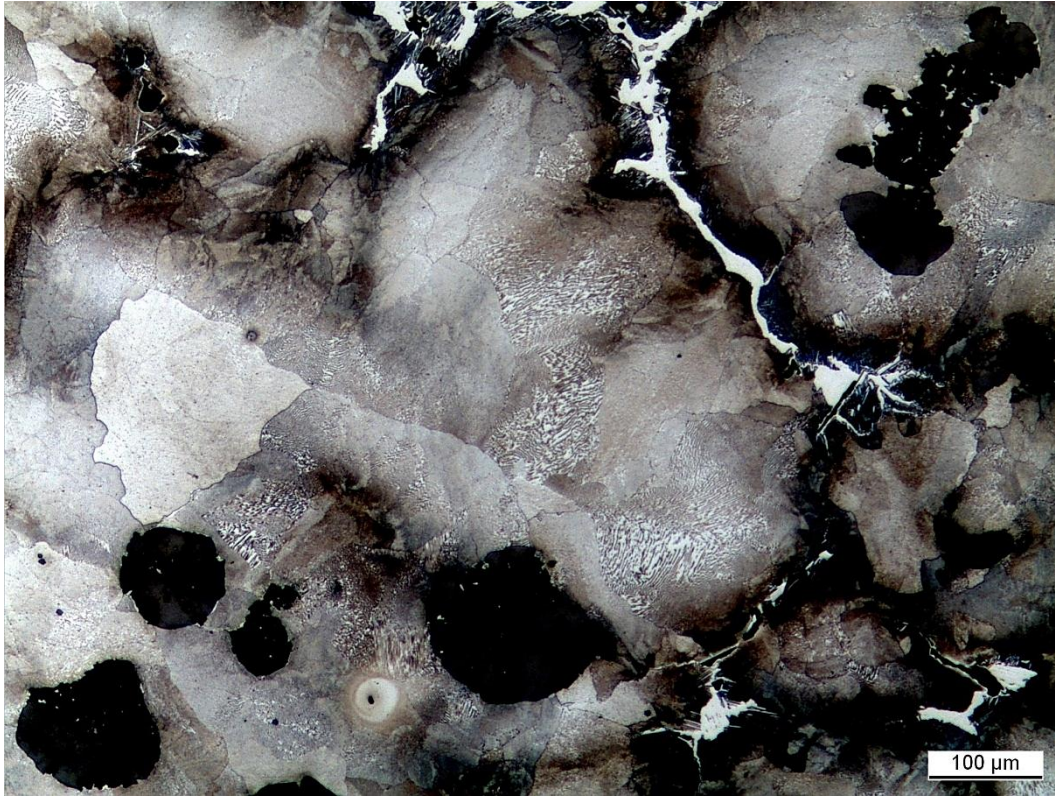
Figure 4.3.1 Microstructure at 100x magnification
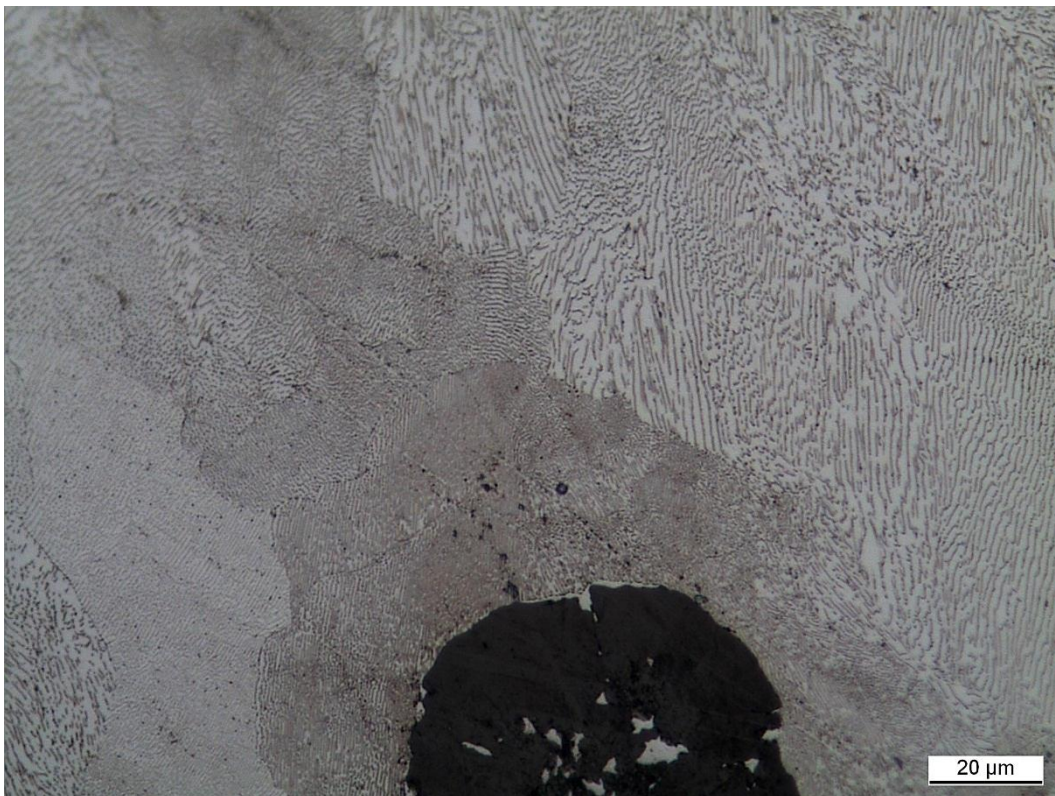
Figure 4.3.2 Detailed image of matrix (500x)

In Figure 4.3.1, black circular constituents are graphite nodules, matrix is pearlite (Figure 4.3.2) and white network is intercellular (segregation) carbide that formed due to the addition of excess amount of some elements such as V, Mo, Cr, and Mn. Segregation patterns of some alloy elements are shown in Figure 4.3.3. These elements segregate to the grain boundaries and promote intercellular carbides. Intercellular carbides lead to an increase in yield strength and a decrease in the elongation capability and tensile strength of ductile iron (Figure 4.3.4). Furthermore, it was mentioned in Section 3.2.1, these carbides give rise to shrinkage porosities during solidification. Figure 4.3.5 and Figure 4.3.6 show that carbides cause porosities even within themselves as micro voids (black regions in the white network) which were formed next or into the intercellular carbides. According to data obtained from X-Ray microanalyzer of SEM, these carbides are Mo rich up to 80% (in weight) and also contain Cr and V.
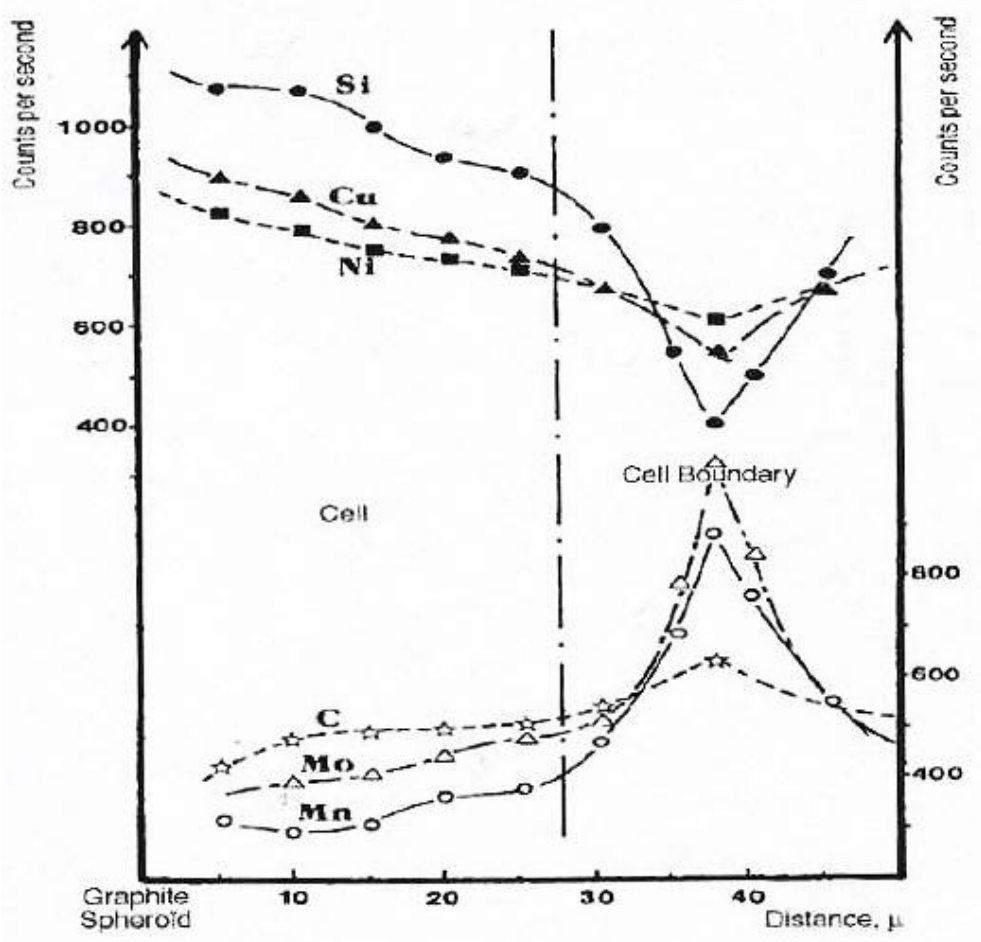
Figure 4.3.3 Segregation patterns of some elements in ductile iron [37]
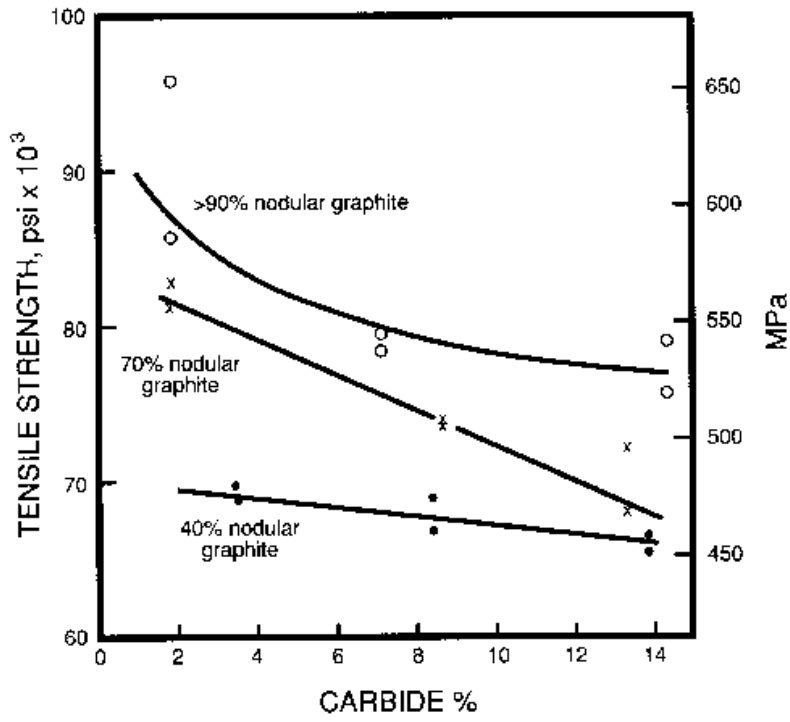
Figure 4.3.4 Effect of nodularity and carbide content on tensile strength of pearlitic ductile iron [31]
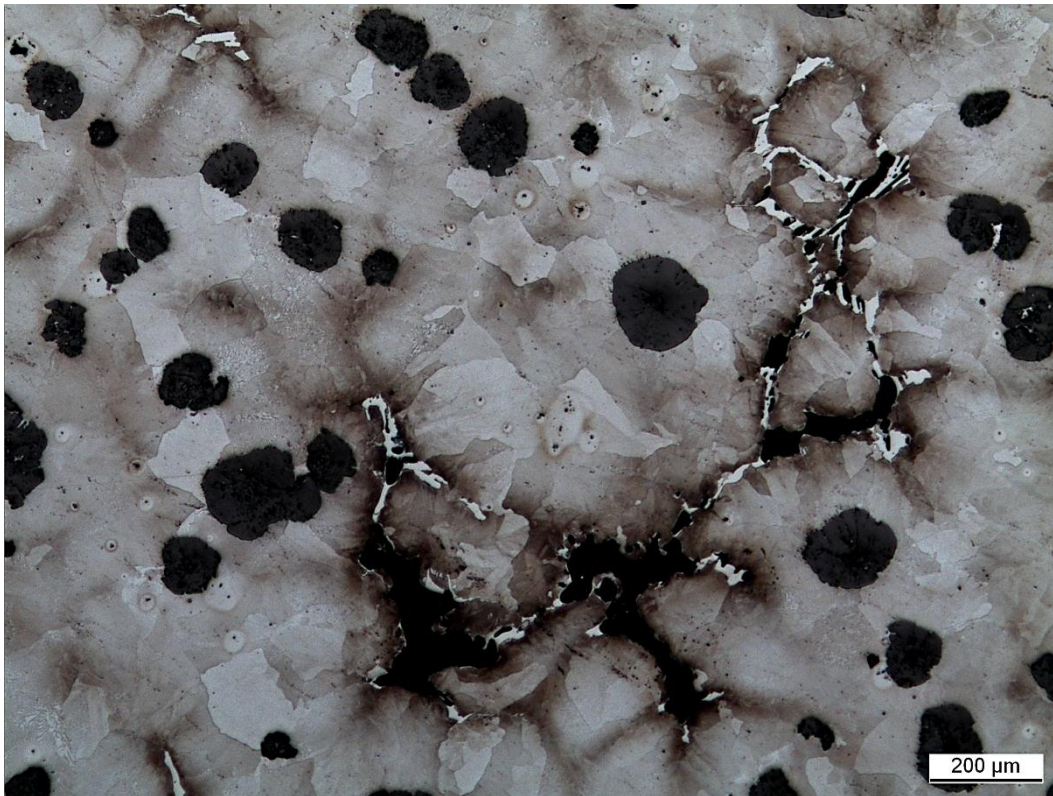
Figure 4.3.5 Intercellular carbide (50x)
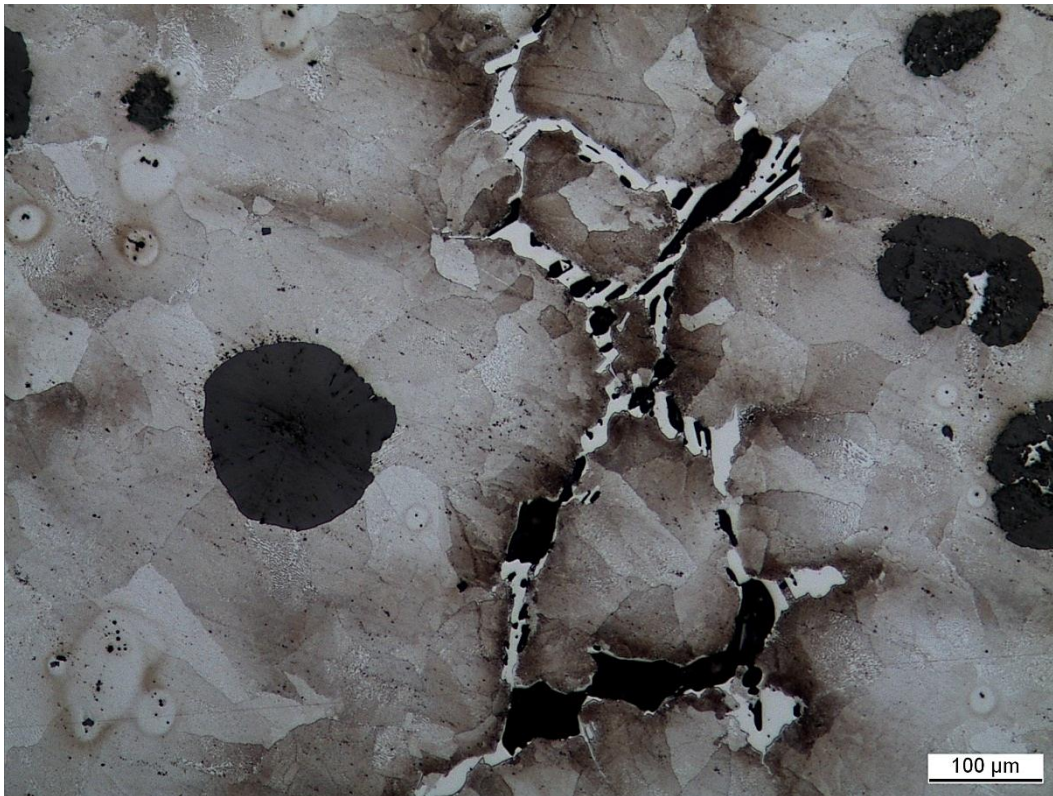
Figure 4.3.6 Intercellular carbide and micro voids (100x)

Graphite shape is more important than dimensions or distribution of graphite nodules. In the case of SF1, most of the graphites are nodular as spheroidal graphite on ASTM A 247 (Figure 4.3.7) which is the optimum shape. Other shapes lead to a decrease in the mechanical properties.
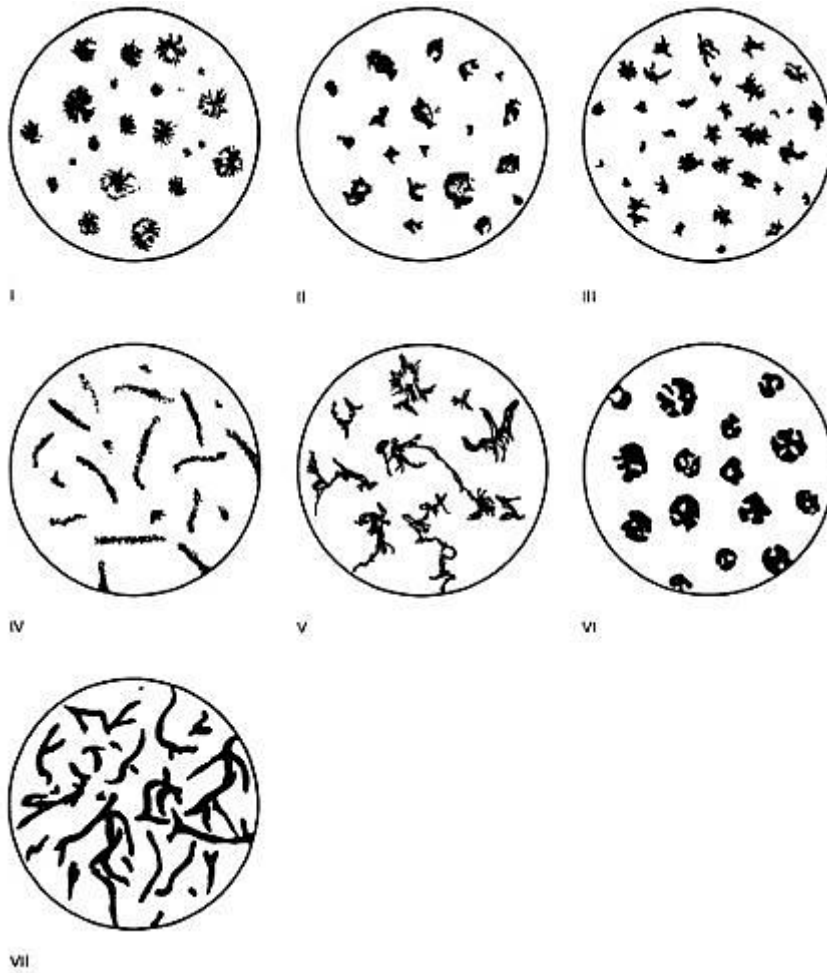
Figure 4.3.7 Typical graphite shapes. I) spheroidal graphite, II) imperfect spheroidal graphite, III) temper graphite, IV) compacted graphite, V) crab graphite, VI) exploded graphite, VII) flake graphite [38]

SF1's graphite diameters are mostly in the range of 100 μm to 200 μm; one of them is seen in Figure 4.3.8.

Finally, steadite formation is observed as in Figure 4.3.9. Steadite formation occurs in the presence of phosphorus element. Upon solidification, this phosphorus may solidify according to Fe-Fe$_3$P eutectic. The resulting microstructure contains Fe$_3$P particles and these particles are hard and brittle. Also, steadite causes the formation of micro voids and shrinkage porosities in carbides as seen in Figure 4.3.6. Therefore, presences of steadite decrease the fatigue limit of the material and make it more brittle. 0.044% is the phosphorus content of SF1 that is higher than 0.02% which is the lowest amount of phosphorus for steadite formation; on the other hand, very low phosphorus content decreases the fluidity of the molten state during casting [39] [31].
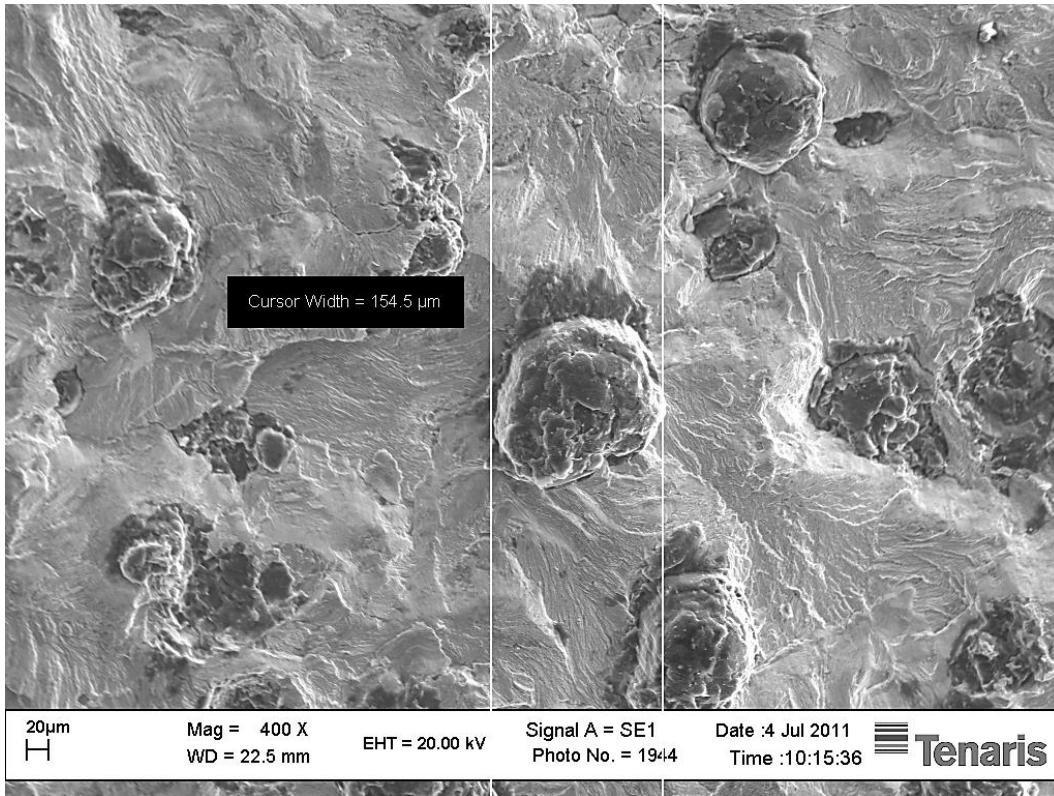
Figure 4.3.8 Graphite nodule dimension (fracture surface of fatigue test specimen)
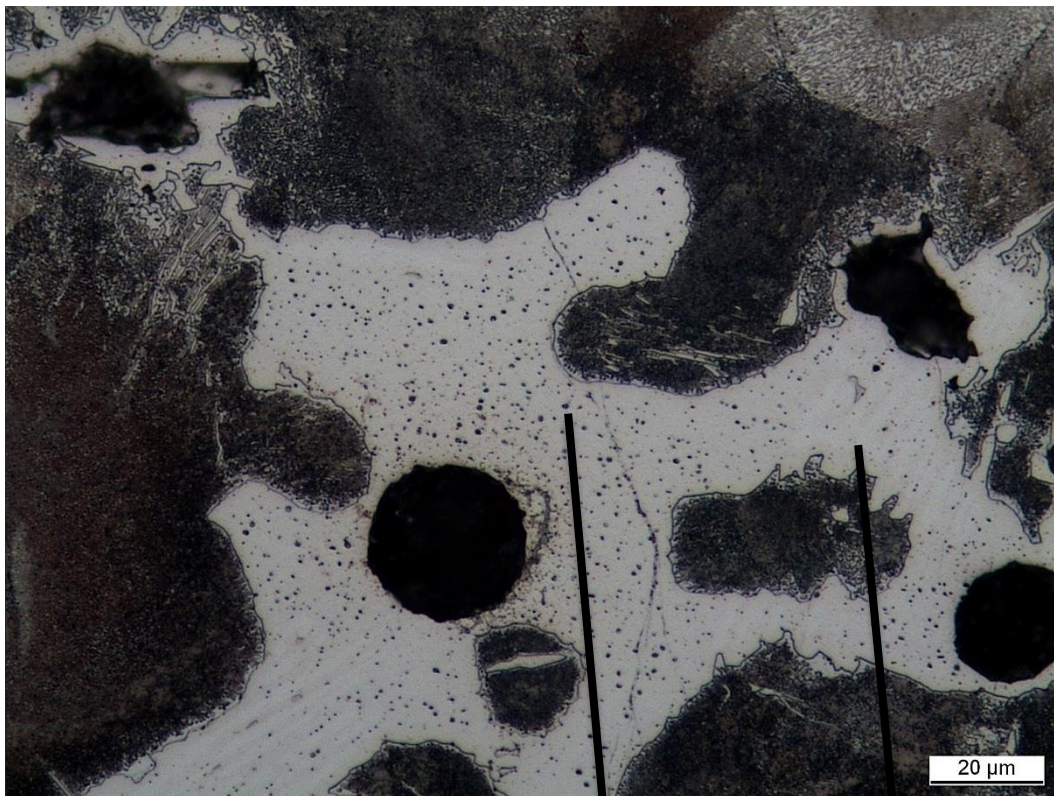
Figure 4.3.9 Steadite

Steadite (black dots)

Carbide (white background)

4.4   Comparison of Experimental Results with the Results of Papadopoulos Criterion

In this study in order to get best results an integral approach was selected due to the fact that: for defective materials, predicting the critical plane is difficult because the applied stresses give rise to a stress gradient on the material. For instance; Hoffman et al [40] showed that for "defect free" materials experimental results match the results of Dang Van criterion; however, for defective materials Dang Van criterion fails. It can be explained by the failure of the homogenization assumption of Dang Van criterion. In detail: only a few grains near defect experience higher stresses than bulk load. Therefore, the likelihood of any slip system of the grain near the defect is aligned with the most critical plane predicted by Dang Van or other critical plane approaches is low. Another reason is: Dang Van criterion cannot be used under compressive hydrostatic stresses.

Moreover, within integral approaches, Papadopoulos was selected due to its high applicability to nonproportional multiaxial loading conditions.

It has to be mentioned that, for the ratio of t_{-1}/f_{-1}, SF1 (0.903) is in the limits of brittle materials (>0.8). We assumed that as a ductile material due to its ductile manner and it is very close to ductile to brittle transition threshold ratio (0.8) for Papadopoulos criterion. This assumption has a detrimental effect on results because in this manner the beneficial effect of compressive mean stress on multiaxial fatigue limit is avoided. However; for our case α does not affect the multiaxial fatigue limit because both for R=-4 and R=-3, sum of normal stress amplitude and normal mean stress is always 0 which gives rise to the value 0 for "$\alpha * \frac{\sigma_a + \sigma_m}{3}$" term of Papadopoulos criterion (Equation 2.4.24). The results are shown below both for R=-4 and R=-3 in Table 4.4.1 and σ_a, σ_m, and σ_m are the experimental values calculated by staircase method.

Error function used in this study is:

$$Error\ (\%) = \frac{\sigma_{eq} - t_{-1}}{t_{-1}}$$

Equation 4.4.1

$R = \dfrac{\sigma_{min}}{\tau_{amp}}$	Uniaxial Test Results		Multiaxial Test Results			Papadopoulos Criterion's Results	
	$t_{-1}\,[MPa]$	$f_{-1}\,[MPa]$	$\sigma_a\,[MPa]$	$\sigma_m\,[MPa]$	$\tau_a[MPa]$	$\sigma_{eq}\,[MPa]$	Error (%)
-4	177.5	196.5	215	-215	107.5	164.209	-7.49
-3	177.5	196.5	200	200	133.5	176.509	-0.56

Table 4.4.1 Experimental and Papadopoulos criterion's results

Furthermore, according to these data the graphs of Papadopoulos criterion on the plane of τ_a and σ_a are shown in Figure 4.4.1 for R=-4 and in Figure 4.4.2 for R=-3 with the marked points of experimental multiaxial fatigue limits.
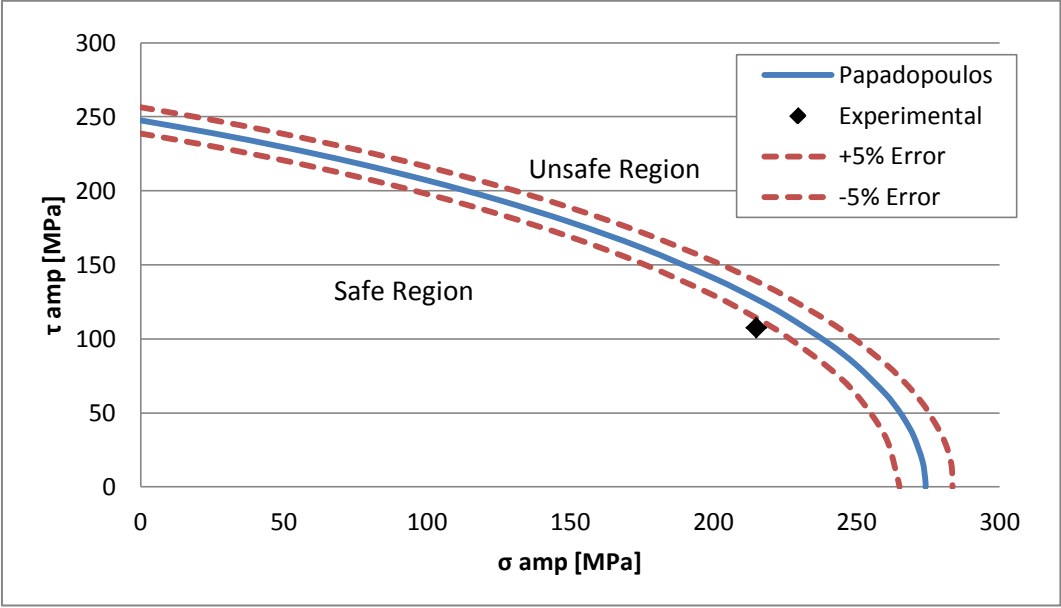
Figure 4.4.1 Papadopoulos criterion at R= -4 with 5% error lines
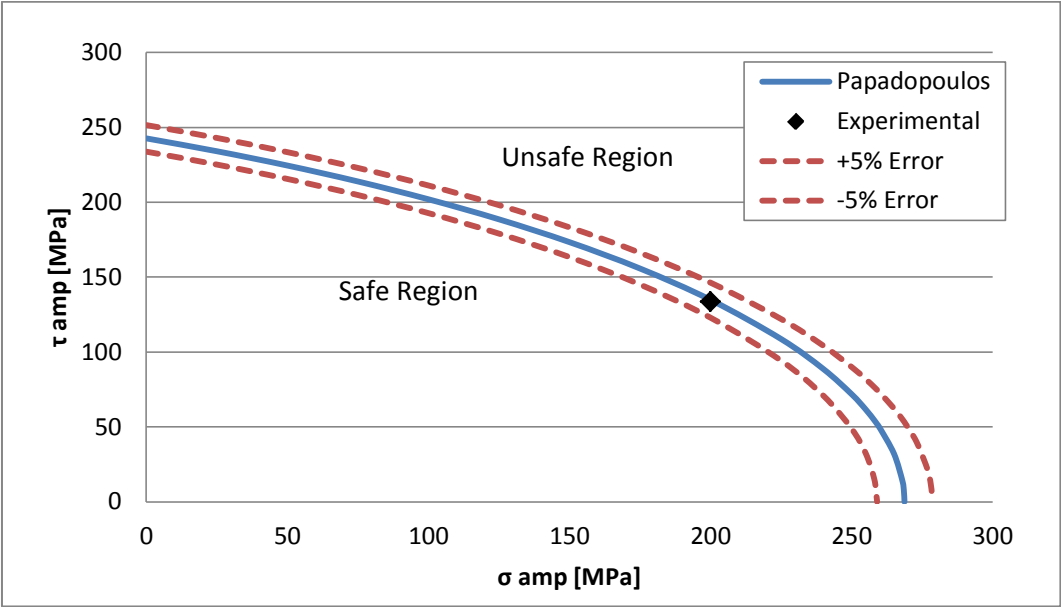
Figure 4.4.2 Papadopoulos criterion at R= -3 with 5% error lines

As seen from the Table 4.4.1, errors percentages of the predictions of Papadopoulos are -7.49% for R=-4 and -0.56% for R=-3 that are lower than 10% so they can be assumed as reasonable results.

Moreover, both of them are conservative results which are preferable in engineering. Therefore, it can be said that according to these data, Papadopoulos criterion is convenient to be used for nonproportional multiaxial fatigue conditions even for defective materials as SF1.

4.5   Effect of Defect Size on Multiaxial Fatigue Limit

In the Papadopoulos criterion defect size is not considered however fully reversed pure axial and fully reversed pure torsional fatigue limits are obtained from the specimens which are dependent on the existence of defects. Therefore, defective materials are also considered indirectly within Papadopoulos criterion. Moreover; due to the dependence of inputs to defect size, stress gradient in the specimen can be neglected. Despite the fact that they are considered indirectly, Nadot et al [5] offered a methodology in order to define the effect of defect size on multiaxial fatigue limit. They proposed to combine Murakami method [6] with multiaxial fatigue limit prediction criteria (i.e Dang Van). Murakami proposed a relation between defect size and fully reversed fatigue limits which is:

$$t_{-1} = D \Big/ \left(\sqrt{area}\right)^{1/n}$$

$$f_{-1} = G \Big/ \left(\sqrt{area}\right)^{1/n}$$

Equation 4.5.1

where G and D are material parameters describing the influence of defect on fatigue limit and *n* is a constant which depends on the defect dimension (small and large cracks).

According to Murakami with respect to his own studies, and Frost [41], Kobayashi and Nakazawa [42], for small defects which are in the range of 10 μm to 800 μm, *n* is equal to 6; for transition zone between small and large defects, *n* is equal to 12; and for large defects which are larger than 1000 μm, *n* is equal to 2.

Figure 4.5.1 shows the relation between threshold stress intensity factor range, ΔK_{th}, and $\sqrt{area}$.

$$\Delta K_{th} = Y\Delta\sigma\sqrt{\pi\sqrt{area}}$$

Equation 4.5.2

where *Y* is shape factor.
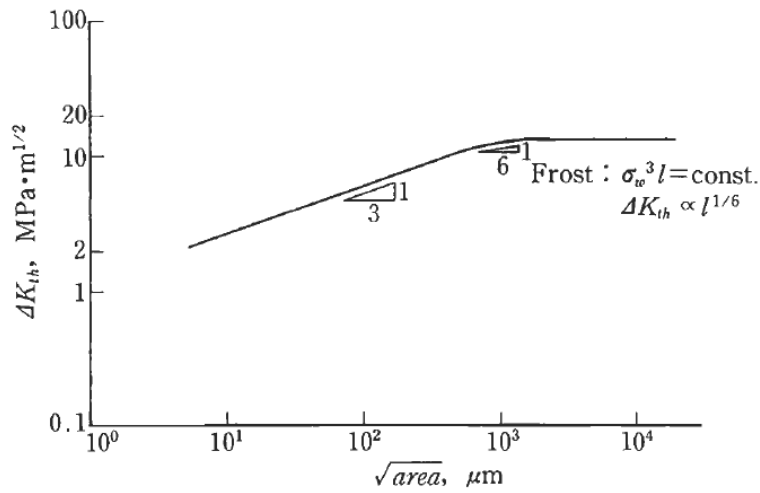
Figure 4.5.1 Dependence of ΔK_{th} on defect size [6]

In this study, Dang Van criterion was changed with Papadopoulos criterion with unlike Reference [5] and average defect size in Nadot's study was in the small defect zone so *n* was taken as 6 but in this study average defect size is in the large defect zone, therefore *n* was taken as 2.

All the defect dimensions are presented in Table 4.5.1 (for some specimens, defects could not observed due to the high plastic deformation occurred during the fatigue tests). Only the specimens that were loaded close to fatigue limit were considered as Nadot did in his own work so specimen 7.6 was excluded. And also, specimen 5.6 and specimen 4.7 were excluded from the average defect size calculations because of having extremely large defects. Therefore, average defect size became 1146.59 μm. Variations of t_{-1} and f_{-1} with respect to defect area are seen in Figure 4.5.2 and dependence of multiaxial fatigue limit on defect size for R=-4 and R=-3 are seen in Figure 4.5.3 and Figure 4.5.4, respectively.

Specimen #	Area [μm²]	$\sqrt{area}$ [μm]	Result
6.6	1220000	1104.5361	Failed
9.6	320000	565.68542	Failed
10.6	460000	670.82039	Run-out
1.7	1650000	1284.5233	Failed
5.7	572000	768.11457	Failed
6.7	3530000	1878.8294	Failed
8.7	948000	974.67943	Failed
9.7	1845000	1358.3078	Run-out
10.7	1287000	1135.7817	Failed
Average	1314667	1146.5891	
5.6	7027000	2650.8489	Failed
7.6	840000	916.51514	Run-out
4.7	6510000	2551.4702	Run-out

Table 4.5.1 Defect dimensions of multiaxial specimens
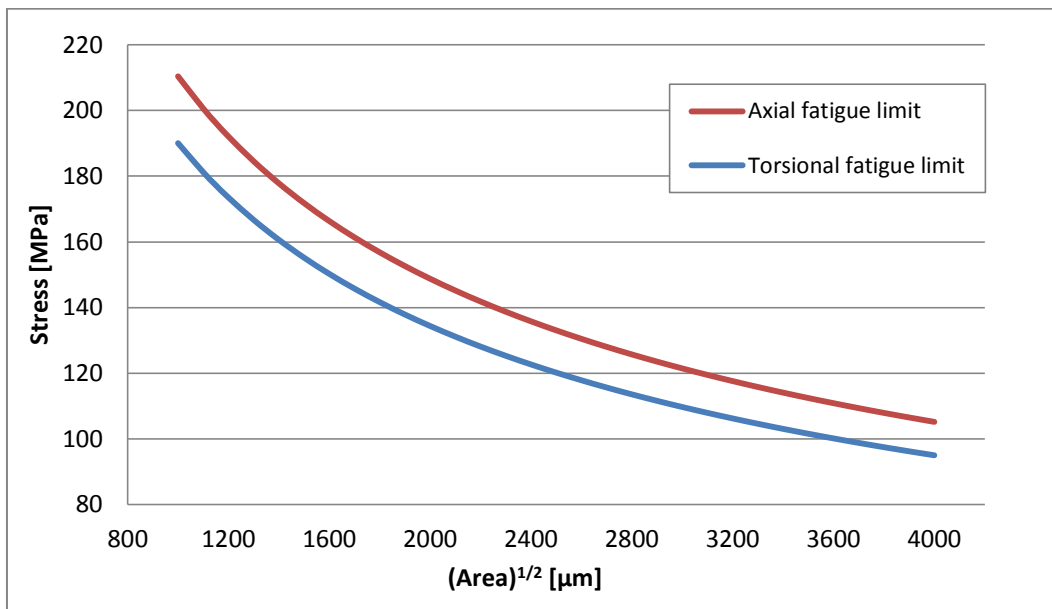
Figure 4.5.2 Effect of defect area on fatigue limits
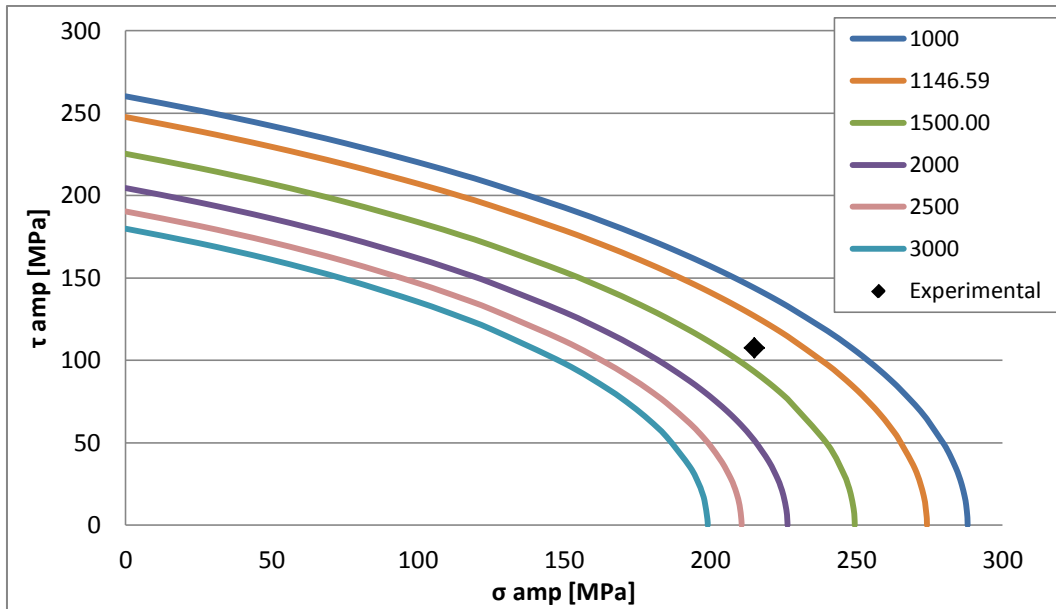
Figure 4.5.3 At R= -4 for different defect dimensions
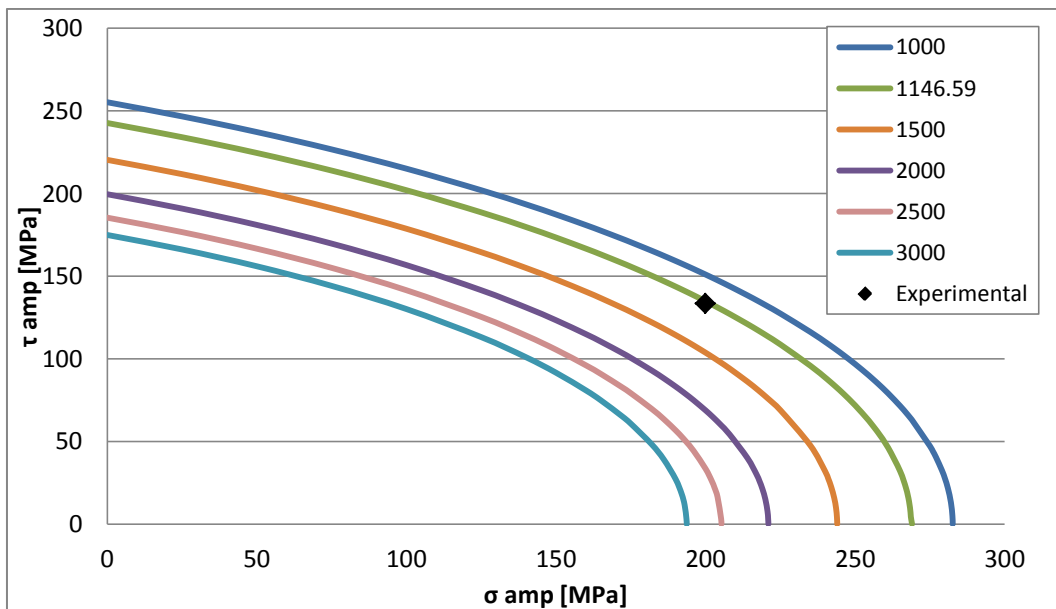
Figure 4.5.4 At R= -3 for different defect dimensions

This methodology was also run at MATLAB for both cases; it was found that D and G values are 6653.75 and 6010.38, respectively; and square root of maximum critical defect size under conditions of the R=-4 case is 1341 μm which is close to 1146.59 μm. It gives an error of 16.96%. For R=-3 case; that square root of maximum critical defect size is 1160 μm. It gives an error of 1.17% which is very

low. It can be concluded that for this methodology error of defect size is mostly dependent on the error of Papadopoulos criterion.

Moreover, even though broad prediction range of this methodology, Figure 4.5.3 and Figure 4.5.4 shows that detrimental effect of defect size on multiaxial fatigue limit decreases with the increase in defect size. Error functions of this methodology were calculated in terms of square root of area, for this reason the error percentages are higher than usual for some cases. If we consider in terms of fatigue limit the error function will decrease due to the suppressed effect of defect size on fatigue limit for high defect dimensions. For instance, torsional fatigue limit difference for defect dimensions 2000 μm and 3000 μm is -18.36% however difference in area is 50%. Therefore, effect of defect size must be considered in terms of fatigue limit.

Furthermore, knowing the real working conditions and material behavior, this methodology can be applied for the prediction of the full scale components by measuring the average defect size or extrapolating from measured data of specimens.

5. Conclusion

In this study, multiaxial fatigue behavior of a ductile iron was aimed to be understood. Specimens were tested under combined compressive axial and torsional nonproportional loadings at $R = \frac{\sigma_{min}}{\tau_{amp}} = -4$ and R=-3. In all the specimens casting defects of shrinkage porosities in a broad range of size were observed; each of them has unique and irregular shapes. The main outputs of this study are:

Fatigue mechanism:

- Fatigue mechanism is generally governed by largest shrinkage porosity, but also positions of the defects are important. The well-known effect of the defect position was observed: the defects close to the specimen surface are more dangerous than inner ones.
- Combined compressive axial and torsional nonproportional cyclic loading gives rise to a fatigue zone which is smooth and featureless at the fracture surface.
- The detrimental effect of compressive strength on torsional fatigue limit was observed; by decreasing the compressive stress from 215 MPa (R=-4) to 200 MPa (R=-3), torsional stress increases from 107.5 MPa (R=-4) to 133.5 MPa (R=-3).

Multiaxial fatigue limit prediction models:

- Integral multiaxial fatigue limit prediction approaches give sufficient results for defective materials due to the consideration of all possible planes in an elementary volume.
- Papadopoulos criterion was chosen as multiaxial fatigue limit prediction model, the comparison with the experimental data results in a good agreement with both ratio cases with an error of 7.5% and 0.6%.
- In order to investigate effect of defect size on multiaxial fatigue limit, Nadot's methodology was applied. A detrimental effect was observed which decreases with the increase in defect size.
- For defective materials Dang Van criterion does not give proper results because its homogenization assumption fails in the presence of defects.

Metallurgical point of view:

- Shrinkage porosities are the main problem for high cycle multiaxial fatigue failures, all the specimens failed due to the presence of shrinkage porosities.

- Excess molybdenum content has two different effects: firstly gives rise to formation of intercellular carbides which can decrease the fatigue limits due to their brittle manner, and secondly cause the formation of shrinkage porosities during casting.

- Excess phosphorus (>0.02%) content lead to formation of steadites that can give rise to formation of shrinkage porosities.

References

[1] J. C. Balthazar and L. Malcher, "A review on the main approaches for determination of the multiaxial high cycle fatigue strength," in *Mechanics of Solids in Brazil*, Brazil, 2007.

[2] B. Li, L. Reis and M. de Freitas, "Comparative study of multiaxial fatigue damage models for ductile structural steels and brittle materials," *International Journal of Fatigue,* vol. 31, pp. 1895-1906, 2009.

[3] Y.-Y. Wang and W.-X. Yao, "Evaluation and comparison of several multiaxial fatigue criteria," *International Journal of Fatigue,* vol. 26, pp. 17-25, 2004.

[4] I. V. Papadopoulos, "A new criterion of fatigue strength for out-of-phase bending and torsion of hard metals," *Fatigue,* vol. 16, pp. 377-384, 1994.

[5] Y. Nadot and V. Denier, "Fatigue failure of suspension arm: experimental analysis and multiaxial criterion," *Engineering Failure Analysis,* vol. 11, pp. 485-499, 2004.

[6] Y. Murakami, Metal Fatigue: Effects of Small Defects and Nonmetallic Inclusions, Oxford: Elsevier, 2002.

[7] J. Schijve, Fatigue of Structures and Materials, Springer, 2008, pp. 13-56.

[8] D. F. Socie and G. B. Marquis, Multiaxial Fatigue, Warrendale: Society of Automotive Engineers, 2000.

[9] M. Meyers and K. Chawla, Mechanical Behavior of Materials, Cambridge: Cambridge, 2009.

[10] R. Stephens, A. Fatemi, R. Stephens and H. O. Fuchs, Metal Fatigue in Engineering, Wiley Interscience, 2001.

[11] G. E. Dieter, Mechanical Metallurgy, McGraw-Hill, 1988.

[12] V. Levkovitch, R. Sievert and B. Svendsen, "Simulation of fatigue crack propagation in ductile metals by blunting and re-sharpening," *International Journal of Fatigue,* vol. 136, pp. 207-220, 2005.

[13] N. Shamsaei, *Multiaxial Fatigue and Deformation Including Non-proportional Hardening,* The University of Toledo, 2010.

[14] D. C. Stouffer and L. T. Dame, Inelastic Deformation of Metals: models, mechanical properties, and metallurgy, New Jersey: Wiley-Interscience, 1996.

[15] J. Papuga, "A survey on evaluating the fatigue limit under multiaxial loading," *International Journal of Fatigue,* vol. 33, pp. 153-165, 2011.

[16] Y. Liu and S. Mahadevan, "Multiaxial high-cycle fatigue criterion and life prediction for metals," *International Journal of Fatigue,* vol. 27, pp. 790-800, 2005.

[17] L. Susmel, R. Tovo and P. Lazzarin, "The mean stress effect on the high-cycle fatigue strength from a multiaxial fatigue point of view," *International Journal of Fatigue,* vol. 27, pp. 928-943, 2005.

[18] G. Sines, "Behavior of metals under complex static and alternating stresses," in *Metal Fatigue*, G. Sines and J. L. Waisman, Eds., New York, McGraw-Hill, 1959, pp. 145-169.

[19] L. Susmel and N. Petrone, "Multiaxial Fatigue Life Estimations for 6082-T6 Cylindrical Specimens under In-Phase and Out-of-Phase Biaxial Loadings," in *Biaxial/Multiaxial Fatigue and Fracture*, vol. 31, A. Carpinteri, M. d. Freitas and A. Spagnoli, Eds., ESIS, 2003, pp. 83-104.

[20] I. V. Papadopoulos, P. Davoli, C. Gorla, M. Filippini and A. Bernasconi, "A comparative study of multiaxial high-cycle fatigue criteria for metals," *International Journal of Fatigue,* vol. 19, pp. 219-235, 1997.

[21] D. F. Socie, *Lecture Notes,* University of Illinois.

[22] B. Crossland, "Effect of large hydroscopic pressures on the torsional fatigue strength of an alloy steel.," in *Proceedings of international conference on fatigue of metals*, London, 1956.

[23] T. Matake, "An explanation on fatigue limit under combined stress," *Japan Society Mechanical Engineering,* vol. 20, no. 141, pp. 257-263, 1977.

[24] A. Carpinteri and A. Spagnoli, "Multiaxial high-cycle criterion for hard metals," *International Journal of Fatigue,* vol. 23, pp. 135-145, 2001.

[25] D. L. McDiarmid, "A general criterion for high cycle multiaxial fatigue failure," *Fatigue and Fracture of Engineering Materials and Structures,* vol. 14, no. 4, pp. 429-453, 1991.

[26] M. W. Brown and K. J. Miller, "A theory for fatigue failure under multiaxial stress-strain condition," *Proceedings of the Institution of Mechanical Engineers,* vol. 187, pp. 745-755, 1973.

[27] K. Dang Van, "Macro-micro approach in high-cycle multiaxial fatigue," in *Advances in Multiaxial Fatigue - STP 1191*, D. L. McDowell and R. Ellis, Eds., Philadelphia, ASTM, 1993, pp. 120-130.

[28] J. Liu, "Weakest link theory and multiaxial criteria," *European Structural Integrity Society,* vol. 25, pp. 55-68, 1999.

[29] A. Bernasconi, S. Foletti and I. V. Papadopoulos, "A study on combined torsion and axial load fatigue limit tests with stresses of different frequencies," *International Journal of Fatigue,* vol. 30, pp. 1430-1440, 2008.

[30] H. Zenner, A. Simbürger and J. Liu, "On the fatigue limit of ductile metals under complex multiaxial loading," *International Journal of Fatigue,* vol. 22, pp. 137-145, 2000.

[31] J. R. Davis, ASM Specialty Handbook: Cast Irons, Ohio: ASM International, 1996.

[32] *ISO 1352: Metallic materials - Torque controlled fatigue testing,* International Organization for Standardization, 2011.

[33] W. Weibull, Fatigue Testing and Analysis of Results, Pergamon, 1961.

[34] P. Pollak, A. Palazotto and T. Nicholas, "A simulation-based investigation of the staircase method for fatigue strength testing," *Mechanics of Materials,* vol. 38, pp. 1170-1181, 2006.

[35] K. A. Brownlee, J. L. Hodge and M. Rosenblatt, "The up- and down method with small samples," *Journal of the American Statistical Association,* vol. 48, pp. 262-277, 1953.

[36] *ISO 12107: Metallic materials - Fatigue testing - Statistical planning and analysis of data,* International Organisation for Standardization, 2003.

[37] E. C. Muratore, "Manganese another look at segregation," Sorelmetal Technical Services, 2006.

[38] *ASTM A247: Standard Test Method for Evaluating the Microstructure of Graphite in Iron*

Castings, Pennsylvania: American Society for Testing and Materials, 2010.

[39] J. M. Radzikowska, "Metallography and Microstructures of Cast Iron," in *ASM Handbook, Volume 9: Metallography and Microstructures*, G. F. Vander Voort, Ed., Ohio, ASM International, 2004, pp. 565-587.

[40] F. Hofmann, G. Bertolino, A. Constanttinescu and M. Ferjani, "Numerical exploration of the Dang Van high cycle fatigue criterion: Application to gradient effects," *Journal of Mechanics of Materials and Structures,* vol. 4, no. 2, pp. 293-308, 2009.

[41] N. E. Frost, "A relation between the critical alternating propagation stress and crack length for mild steel," *Proceedings of the Institution of Mechanical Engineers,* vol. 173, no. 35, pp. 811-827, 1959.

[42] H. Kobayashi and H. Nakazawa, "The effects of notch depth on the initiation propagation and non-propagation of fatigue cracks," *Transactions of the Japan Society of Mechanical Engineers,* vol. 35, no. 277, pp. 1856-1863, 1969.

[43] S. Foletti, S. Beretta and G. Bucca, "A numerical 3D model to study ratcheting damage of a tramcar line," *Wear,* vol. 268, pp. 737-746, 2010.